Grain refinement of Mg-Zn and Mg-Mn alloys by SiC inoculation

Doctoral Thesis

(Dissertation)

to be awarded the degree

Doctor of Engineering (Dr.-Ing.)

submitted by

Jian Gu

from Jiangsu / PR China

approved by the Faculty of Natural and Materials Science,

Clausthal University of Technology

Date of oral examination

07.08.2017

Dean

Prof. Dr.-Ing. Karl-Heinz Spitzer

Chairperson of the Board of Examiners

Prof. Dr. rer. nat. Albrecht Wolter

Supervising tutor:

apl. Prof. Dr.-Ing. (a.D.) Rainer Schmid-Fetzer

Reviewer:

Prof. Dr.-Ing. Karl Ulrich Kainer

Abstract

The addition of a grain refiner to molten metal prior to casting is one of the most important approaches to reduce the final grain size of both cast and wrought Mg alloys. Although it has been investigated for decades, the practical grain refinement methods of Mg alloys are still limited, and the grain refining mechanisms are still not fully understood. For Al-free Mg alloys, Zr is an extremely effective nucleant but an expensive one. Reducing the consumption of Zr and hence the cost of grain refinement is of great interest. Moreover, Zr will lose its grain refinement effect in Al-free Mg alloys if it encounters Mn, Si, or Fe due to the formation of stable intermetallic compounds. Thus, the development of a compatible and potent grain refiner to substitute Zr to be used in Al-free Mg alloys that contain some amount of Mn, Si, or Fe is necessary.

In the present work, SiC particles were validated as an effective grain refiner for both as-cast binary Mg-Zn and Mg-Mn alloys. The effects of grain-refining parameters on the grain sizes have been investigated. Comparative tests using high purity Mg ingots were carried out to clarify the grain refining mechanisms. The effects of micro-alloying element Al in Mg-Zn-SiC system were also investigated, and the poisoning grain refining mechanism was proposed.

The experimental results show that the added SiC particles cannot directly act as the nucleation sites of α-Mg grains. Mn_3Si or $(Mn,Fe)_3Si$ particles formed *in-situ* prior to the formation of α-Mg grains from the reaction between SiC particles and Mn (or Fe) are the actual nucleation sites, which depends on whether Fe atoms can substitute some of the Mn atoms during reaction. This work also found that the grain refining efficiency of SiC inoculation is not only dominated by the presence of *in-situ* formed heterogeneous nucleation sites, but also by the solute element of Mn or Zn. The co-existence of potent nucleants and solutes with high growth restriction factor (Q) values is necessary to obtain the highest grain refining efficiency. The grain coarsening effect with Al addition into Mg-Zn-SiC system is attributed to a decrease in nucleation potency where the lower potent $Al_8(Mn,Fe)_5$ intermetallic particles formed.

Abstract

Die Zugabe von Kornfeinern zu Magnesiumschmelzen ist das derzeit am meisten verwendete Verfahren, um die Größe der Kristallite in Guss- und Knetwerkstoffen zu reduzieren. Obwohl diese Praxis seit vielen Jahrzehnten untersucht wird, gibt es nur eine beschränkte Anzahl an Kornfeinern für Magnesiumlegierungen und ihre Wirkmechanismen sind noch nicht vollständig verstanden. Für Al-freie Magnesiumlegierungen ist Zr ein geeignetes, aber teures Additiv zur Kornfeinung. Daher ist es von großem Interesse, den Zr-Verbrauch zu reduzieren. Darüber hinaus verliert Zr in Al-freien Legierungen seine Wirkung, wenn Mn, Si oder Fe vorhanden sind, da intermetallische Phasen mit diesen Elementen gebildet werden. Die Entwicklung eines wirksamen Kornfeinungsmittels als Substitution für Zr für Al-freie Legierungen mit geringen Gehalten an Mn, Si und Fe ist daher von großer technischer und wirtschaftlicher Bedeutung.

In dieser Arbeit werden SiC-Partikel als Kornfeiner für gegossene Mg-Zn und Mg-Mn-Legierungen untersucht. Eine Parameterstudie wurde durchgeführt, bei der die Einflüsse auf die Korngröße untersucht wurden. Vergleichende Untersuchungen mit hochreinem Magnesium wurden durchgeführt, um den Mechanismus der Kornfeinung aufzuklären. Die Einflüsse des Mikrolegierungselementes Al im Mg-Zn-SiC System wurden ebenfalls untersucht und ein als „poisoning“ bekannter Mechanismus wurde angenommen.

Die experimentellen Ergebnisse zeigen, dass die SiC-Partikel nicht direkt als Kornfeiner des α-Mg dienen. Die Mn_3Si or $(Mn,Fe)_3Si$ Partikel, die sich *in-situ* vor der Bildung des α-Mg ausscheiden, sind die eigentlichen Nuclei. Ihre Zusammensetzung hängt von der Konzentration des Fe und Mn in der Schmelze ab. In dieser Arbeit konnte darüber hinaus gezeigt werden, dass die Effektivität des SiC als Kornfeiner nicht nur von der *in-situ* Bildung der Nuclei abhängt, sondern auch von der Konzentration des gelösten Mn und Zn. Das gleichzeitige Vorhandensein von Nuclei und gelöste Elemente mit hohen *Q*-Werten ist notwendig für das Erreichen einer optimalen Kornfeinung. Der Effekt des Kornwachstums durch Al-Zugabe im System Mg-Zn-SiC wird zurückgeführt auf eine geringere Nukleationsfähigkeit der $Al_8(Mn,Fe)_5$-Phase.

List of abbreviations

BSE	Backscattered scanning electron
CS	Constitutional supercooling
E2EM	Edge-to-edge matching
EDS	Energy dispersive spectroscopy
FIB	Focused ion beam
hcp	Hexagonal close-packed
HP	High purity
MM	Mischmetal
OM	Optical microscopy
OR	Orientation relationship
ppm	Parts per million
PS	Pseudomorphic solid
RE	Rare earths
RGS	Relative grain size
RP	Reduction percentage
SEM	Scanning electron microscope
S-L	Solid-liquid
TEM	Transmission electron microscope
XRD	X-ray diffraction
XRF	X-ray fluorescence

Nomenclature in alphabetical order

a	The intercept of the linear fit line related to the maximum number of particles that actually nucleate grains, see Eq. 2-8 (μm)
a_0	Lattice parameter for the nucleated phase, see Eq. 2-1 (nm)
Δa	Lattice parameter difference between the substrate and nucleated phase, see Eq. 2-1 (nm)
b	The slope of the linear fit line related to the potency of the nucleant particles, see Eq. 2-8 (μm•K)
C_0	Initial composition of the solute in a binary alloy, see Eq. 2-5 (wt%, note that all compositions are given in wt% in this thesis unless specified)
$C_{0,i}$	Initial composition of solute element i, see Eq. 2-6 (wt%)
C_l	Solute composition of the liquid in front of the S-L interface, see Eq. 2-20 (wt%)
C_L^*	Equilibrium solute composition of the liquid at the interface, see Eq. 2-12 (wt%)
C_s	Solute composition of the solid in front of the S-L interface, see Eq. 2-19 (wt%)
C_S^*	Equilibrium solute composition of the solid at the interface, see Eq. 2-12 (wt%)
d	Inoculant particle size, see Eq. 6-2 (μm)
d_A	The grain size of the alloy system after inoculation, see Eq. 6-1 (μm)
d_B	The grain size of the alloy system before inoculation, see Eq. 6-1 (μm)
d_{gs}	Grain size, see Eq. 2-9 (μm)
d_n	Diameter of nucleant particle, see Eq. 2-4 (μm)
D_s	Solute diffusion coefficient in the liquid, see Eq. 2-16 ($m^2 \cdot s^{-1}$)
f_d	Interplanar spacing mismatch (%)
f_r	Interatomic spacing misfit (%)
f_s	Solid fraction, see Eq. 2-21

g	Gravitational acceleration, see Eq. 6-2 ($m \bullet s^{-2}$)
ΔG_n^0	Free energy barrier for nucleation on a substrate, see Eq. 2-13 ($kJ \bullet mol^{-1}$)
(hkl)	Low index plane, see Eq. 2-3
h_c	Critical thickness (nm)
k	Distribution coefficient, see Eq. 2-5
k_i	Distribution coefficient of solute element i, see Eq. 2-6
K_i	A constant value of element i, see Eq. 6-3 ($g \bullet cm^{-3} \bullet {}^oC^{-1}$)
L(l)	Liquid phase, see Eq. 2-10
M	Atomic weight, see Eq. 6-6 ($kg \bullet mol^{-1}$)
m_l	Slope of the liquidus line, see Eq. 2-5 ($K \bullet wt\%^{-1}$)
$m_{l,i}$	Slope of the liquidus line of solute element i, see Eq. 2-6 ($K \bullet wt\%^{-1}$)
m_s	Slope of the solidus line, see Eq. 2-19 ($K \bullet wt\%^{-1}$)
N	Potent nucleating substrate
P	Supercooling parameter, see Eq. 2-7 (K)
Q	Growth restriction factor, see Eq. 2-8 (K)
r	Radius of a growing spherical crystal, see Eq. 2-16 (μm)
R	The gas constant, see Eq. 6-5 ($J \bullet mol^{-1} \bullet K^{-1}$)
r^*	Critical radius of a nucleus (μm)
S	Solid phase
S_d	Settling distance, see Eq. 6-2 (mm)
S_g	Growth parameter
ΔS_f	Entropy of fusion, see Eq. 2-13 ($J \bullet K^{-1}$)
ΔS_V	Entropy of fusion per unit volume, see Eq. 2-4 ($J \bullet K^{-1} \bullet m^{-3}$)

t	Time, see Eq. 2-16 (s)
T	The actual temperature of the molten alloy system, see Eq. 6-3 (K)
T_0	Melting point, see Eq. 2-18 (K)
T_A	Actual temperature of the melt, see Eq. 2-19 (K)
T_E	Equilibrium liquidus temperature, see Eq. 2-18 (K)
T_L	The liquidus temperature of the alloy system, see Eq. 6-3 (K)
ΔT	Solidification undercooling, see Eq. 2-11 (K)
ΔT_c	Curvature undercooling, see Eq. 2-11 (K)
ΔT_{cs}	Constitutional supercooling, see Eq. 2-11 (K)
ΔT_{fg}	Free growth undercooling, see Eq. 2-4 (K)
ΔT_k	Kinetic undercooling, see Eq. 2-11 (K)
ΔT_n	Critical undercooling required for nucleation, see Eq. 2-23 (K)
$\Delta T_{n\text{-}min}$	Nucleation undercooling of the most potent particle (K)
ΔT_t	Thermal undercooling, see Eq. 2-11 (K)
[uvw]	Low index direction on the (hkl), see Eq. 2-3
V	Growth rate of a spherical crystal, see Eq. 2-17 ($m \bullet s^{-1}$)
X_{cs}	Distance the previous grain must grow to generate sufficient CS, see Eq. 2-9 (μm)
X'_{dl}	Diffusion length from the S-L interface at X_{cs} of the previously nucleated grain, see Eq. 2-9 (μm)
X_{Sd}	Average distance to the activated particles, see Eq. 2-9 (μm)
Y_i	The atomic fraction of element i in the alloy, see Eq. 6-3

Greek symbols

$\alpha(s)$	Solid phase after peritectic reaction, see Eq. 2-10
$\beta(s)$	Solid phase before peritectic reaction, see Eq. 2-10
γ_{nl}	Interfacial energy between nucleus and liquid, see Eq. 2-15 ($J \bullet m^{-2}$)
γ_{sl}	Interfacial energy between substrate and liquid, see Eq. 2-15 ($J \bullet m^{-2}$)
γ_{sn}	Interfacial energy between substrate and nucleus, see Eq. 2-15 ($J \bullet m^{-2}$)
δ	Disregistry, see Eq. 2-1 (%)
η	The viscosity of molten alloy system, see Eq. 6-2 ($N \bullet s \bullet m^{-2}$)
θ	Wetting angle, see Eq. 2-13 (°)
λ_s	Interfacial parameter, see Eq. 2-16
ρ_P	The density of inoculant particle, see Eq. 6-2 ($g \bullet cm^{-3}$)
ρ_L	The density of molten alloy system, see Eq. 6-2 ($g \bullet cm^{-3}$)
$\rho_{L,i}$	The liquid density of element *i*, see Eq. 6-3 ($g \bullet cm^{-3}$)
$\rho_{m,i}$	The liquid density of element *i* at the melting point, see Eq. 6-3 ($g \bullet cm^{-3}$)
σ	Solid-liquid interfacial energy, see Eq. 2-4 ($J \bullet m^{-2}$)
φ	Angle between a pair of adjacent low index directions on the (*hkl*), see Eq. 2-3 (°)
Ω	Supersaturation, see Eq. 2-12

Table of contents

1 Introduction 1

2 Literature review 3

2.1 Grain refinement theories in magnesium alloys 3

2.1.1 Heterogeneous nucleation theory 3

2.1.2 Solute paradigm theory 9

2.1.3 Interdependence theory 12

2.1.4 Peritectic theory 14

2.2 Nucleation and growth 15

2.2.1 Nucleation 16

2.2.2 Grain growth and development of CS zone 18

2.3 Effect of elements on grain refinement 21

2.3.1 Fe 22

2.3.2 Mn 23

2.3.3 Si 25

2.3.4 Ca 25

2.3.5 Zr 26

2.4 Effects of carbon-containing particles on grain refinement 26

2.4.1 Carbon segregation 27

2.4.2 Al_4C_3 28

2.4.3 Al_2CO 28

2.4.4 Al_2MgC_2 29

2.5 Mg-Zn and Mg-Mn alloys 29

3 Motivations and objectives 31

4 Experimental procedures 32

4.1 Source materials 32

4.2 Casting 32

4.3 Microstructure 34

4.3.1 Optical microscopy 34

4.3.2 SEM analysis 35

4.3.3 FIB technology and TEM analysis 35

4.3.4 XRD analysis 36

4.4 Solidification simulation 36

5 Results 38

5.1 Grain refinement of Mg-Zn-SiC alloys 38

5.1.1 Grain refinement of Mg-*x*Zn alloys 38

5.1.2 Grain refinement of Mg-*x*Zn-0.3SiC alloys 42

5.1.3 Effects of grain-refining parameters on Mg-3Zn-SiC alloys 45

5.1.4 Characterization of nucleant particles in Mg-Zn-SiC alloy system 53

5.1.5 Effects of micro-alloying element Al 59

5.1.6 Comparison experiments 63

5.2 Grain refinement of Mg-Mn-SiC alloys 66

5.2.1 Grain refinement of Mg-*x*Mn alloys 66

5.2.2 Grain refinement of Mg-*x*Mn-0.3SiC alloys 69

5.2.3 Effects of grain-refining parameters on Mg-1Mn-SiC alloys 74

5.2.4 Characterization of nucleant particles in Mg-Mn-SiC alloy system 81

5.2.5 Solidification simulation of Mg-Mn-SiC system 88

6 Discussion 90

6.1 The role of solute element Zn and Mn in pure Mg 90

6.2 Grain refinement of Mg-Zn alloys by SiC inoculation 93

6.2.1 Effects of Zn contents 93

6.2.2 The role of SiC in Mg-Zn system 97

6.2.3 Poisoning mechanism of element Al in Mg-Zn-SiC system 102

6.2.4 Different grain refinement behavior between graphite (C) and SiC 103

6.2.5 Comparisons of Mg-3Zn-0.3SiC, Mg-3Al-0.3SiC and Mg-3Zn-0.3Zr 106

6.3 Grain refinement of Mg-Mn alloys by SiC inoculation 107

6.3.1 Effects of Mn contents 107

6.3.2 The role of SiC in Mg-Mn system 109

6.3.3 The formation of Mn_3Si nuclei 111

6.3.4 The influence of impurity element Fe 113

7 Summary 116

8 Acknowledgements 118

9 References 119

1 Introduction

Recent research indicates that grain refinement of Mg alloys can be attributed to two key factors: solute elements and nucleant particles [1, 2]. The contribution of solute is related to the formation of constitutional supercooling (CS) zone ahead of the solid-liquid (S-L) interface where heterogeneous nucleation could be activated in terms of the interdependency theory [3]. Thus, a fine-grain structure is obtained. The addition of nucleant particles named as inoculation treatment is a process by adding foreign particles into the melt prior to casting. This promotes the heterogeneous nucleation rate depending on their potency, size distribution and particle number density [2]. Although lots of researches have been focused on inoculation additions, the corresponding grain refining mechanisms are still not fully understood [4].

In view of grain refinement, Mg alloys can be generally classified into two broad groups: Al-free and Al-bearing. Most of the new developed grain refiners, such as Al_2Y [5, 6], AlN [7], Al_2Ca [8], CaO [9, 10] for Al-bearing Mg alloys are not as efficient as the commercially available ones, such as Zr in Al-free Mg alloys. However, there are still several limitations for Zr addition in Al-free Mg alloys, such as Zr master alloys are expensive and difficult to be added into the melt [11, 12]. In addition, Zr is only available for non-Al/Mn/Si/Fe-containing Mg alloys [4]. Recently, it was found that SiC, which shows potential in commercial applications in Al-bearing Mg alloys due to its environmental friendly, low cost and relatively good grain refining effect [13-15], can not only refine the as-cast Al-bearing Mg alloys but also the as-cast Al-free Mg alloys, such as Mg-Zn binary alloys [16, 17]. Unfortunately, no corresponding grain refinement mechanism was proposed. If the SiC particles can be successfully used as grain refiners for a wide range of Al-free Mg alloys to substitute the Zr, it would definitely have practical significance.

In addition, Mn has a great influence on the grain refinement of Mg alloys inoculated by carbon sources. Contrary results were always observed by different researchers [13, 18-20] due to the complex interactions among Mn, Al and carbon sources in the Mg melt. Also, Mn is commonly used to remove the detrimental impurity Fe in preparation of pure Mg ingots [21], so the interaction between carbon sources and Mn cannot be ignored. Therefore, Mg-Zn and

Mg-Mn binary alloys were selected to be inoculated with SiC particles. Special attention will be paid to the discussion of the grain refinement mechanism during solidification process, which may give new insights into the grain refinement mechanism of carbon inoculation in Al-free Mg alloys.

To date, the investigations on grain refinement of Mg-Zn and Mg-Mn binary alloys by SiC particles are limited. The influences of inoculation parameters of SiC particles such as the addition amount, particle size, addition temperature and holding time on grain refinement of Mg-Zn and Mg-Mn alloys are still unclear. Therefore, it is necessary to carry out a systematic investigation on the grain refinement efficiency of Mg-Zn and Mg-Mn alloys with SiC inoculation.

2 Literature review

2.1 Grain refinement theories in magnesium alloys

Grain refinement mechanisms were extensively investigated over the past six decades. Many theories and models were developed in light metals and their alloys. It is well known that both solute elements and nucleant particles play significant roles in controlling grain size. Current grain refinement theories of cast Mg alloys can be roughly divided into four categories: the heterogeneous nucleation theory, the solute paradigm theory, the interdependence theory and the peritectic theory.

2.1.1 Heterogeneous nucleation theory

Heterogeneous nucleation fundamentally emphasizes the role of potent nucleant particles in promoting nucleation of grains. Three main factors of the nucleant particles, i.e. their potency, size distribution and particle number density, determine the efficiency of grain refinement [2]. Considering the potency of a nucleant, which is closely related to the crystallographic matching between the nuclei and the matrix, several models were proposed to evaluate this effect including the Turnbull and Vonnegut model [22], the Bramfitt model [23], the edge-to-edge matching (E2EM) model [24] and the epitaxial growth model [25]. Another important aspect to evaluate grain refinement efficiency that focuses on particle size effects is the free growth model [26].

In 1952, Turnbull and Vonnegut [22] emphasized the importance of crystallographic disregistry on heterogeneous nucleation behavior. The disregistry δ can be defined as:

$$\delta = \Delta a / a_0 \qquad 2\text{-}1$$

where Δa is the difference between the lattice parameter of the substrate and the nucleated solid for a low-index plane, and a_0 is the lattice parameter for the nucleated solid [22]. In this model, it places a strict limitation on the selection of a crystallographic relationship because only planes of similar atomic arrangement are considered.

In 1970, Bramfitt [23] proposed a modified equation in terms of angular difference between

the crystallographic directions within the planes. The main progress made by Bramfitt is redefinition of δ from linear disregistry to planar disregistry [27]. The modified equation can be expressed in two forms, and the first equation is generally defined as follows:

$$\delta = [(\delta_1 + \delta_2 + \delta_3) / 3] \times 100 \quad 2\text{-}2$$

where δ_1, δ_2 and δ_3 are the disregistries calculated along the three lowest-index directions within a 90 degree quadrant of the planes of the nucleated solid and the substrate [23]. The calculated result is multiplied by 100 in order to change it into percentage value.

The second, or more specific, form of the modified equation is expressed as:

$$\delta_{(hkl)_n}^{(hkl)_s} = \sum_{i=1}^{3} \frac{\frac{|d_{[uvw]_s^i} \cos\varphi - d_{[uvw]_n^i}|}{d_{[uvw]_n^i}}}{3} \times 100 \quad 2\text{-}3$$

where *s* and *n* represent the substrate and the nucleated solid, respectively; (*hkl*) is a low index plane, [*uvw*] is a low index direction on the (*hkl*), φ is the angle between a pair of adjacent low index directions on the (*hkl*) [23, 27]. As pointed out by Bramfitt, the nucleant substrate is potent when the planar disregistry is less than 12%; otherwise the potency is poor when the disregistry is above 12% [23]. The grain refining efficiencies of Al_4C_3 [28], TiB_2 [29, 30] and MgO [31] in Mg-Al alloys were successfully applied with this model. The calculated planar disregistry values between those particles and α-Mg is much less than 12%.

The E2EM model, proposed by Zhang and Kelly [32, 33], was originally developed to predict the orientation relationships (ORs) and the corresponding interfaces between two phases. The basis of the E2EM model for understanding the crystallography of partially coherent precipitates is the minimization of the interfacial energy between the two phases. It points out that the edges of the planes that meet at the interface should be close-packed or relatively close-packed rows of atoms [34]. The essential criterion to form such interface is that both the interatomic spacing misfit (f_r) < 10% and the interplanar spacing mismatch (f_d) < 10% [35]. Compared with other crystallographic model, the E2EM model is more rigorous because it evaluates both the f_r and f_d, which can be applied in a wide range of more complicated systems. E2EM model provides a number of insights into the mechanisms behind some issues such as superheating [32, 33, 36], grain poisoning effect [35] and which particles are likely to be

better grain refiners [7, 37-41]. The E2EM model condition is schematically shown in Fig. 2-1 [42].

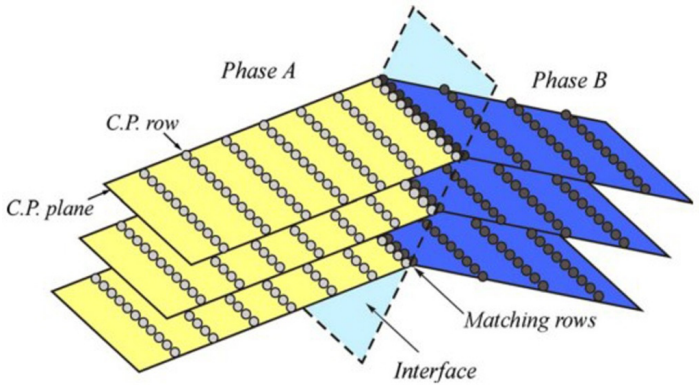

Fig. 2-1 Schematic diagram of an interface meeting the E2EM model conditions. C.P. row and C.P. Plane represent the close-packed row and close-packed plane, respectively [42]

More recently, an epitaxial growth model to explain the early stages of nucleation for heterogeneous nucleation on potent substrates was proposed [25]. The epitaxial growth model is schematically shown in Fig. 2-2 [25]. At the atomic level, the process of heterogeneous nucleation on a potent substrate can be considered to be atom-by-atom building of the initial solid phase on a template. It is proposed that epitaxial growth of a pseudomorphic solid (PS) layer on the substrate surface initiates heterogeneous nucleation at a critical undercooling. Misfit dislocations are created to release the elastic strain energy in the PS layer at a critical thickness h_c. This converts the strained PS layer to a strainless solid (S) [25].

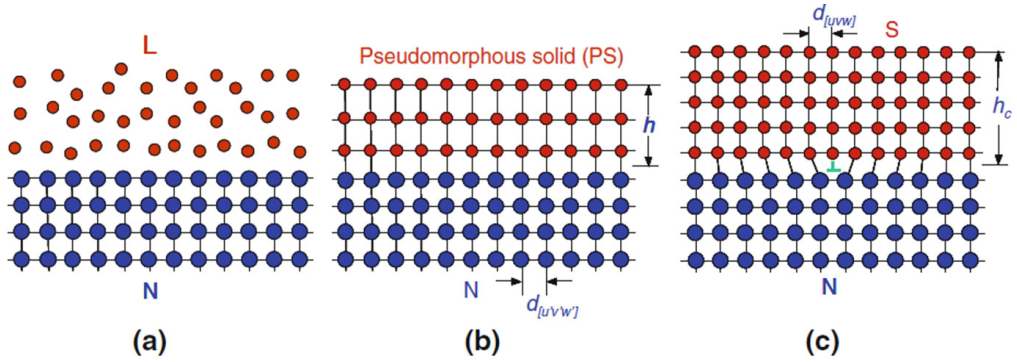

Fig. 2-2 Schematic illustration of the epitaxial model for heterogeneous nucleation of a solid phase (S) on a potent nucleating substrate (N) from a liquid phase (L): (a) sketch showing the L/N interface before the growth of the PS layer; (b) the initial formation of the PS with a coherent PS/N interface; and (c) completion of the epitaxial nucleation at a critical thickness (h_c) [25]

Combining the fundamentals of absorption theory [43] and hypernucleation theory [44, 45], and considering the effects of the solute segregating at the nucleation interface [46], this model could be used to explain the grain refining mechanism involving Al–Ti–B-based grain refiners in Al alloys [47-50]. Furthermore, molecular dynamic simulations indicate that TiB_2 particles may be more active if the close-packed layer exposed to the Al melt contains Ti atoms rather than B atoms [46, 51, 52]. It is worth mentioning that the assumed Al_3Ti layers on TiB_2 particles were experimentally verified using high resolution transmission electron microscope (TEM) by Fan's work [53]. This investigation has confirmed the existence of a Ti-rich monolayer on the (0001) TiB_2 surface, which is most likely to be a (112) Al_3Ti two-dimensional compound [53]. In addition, this model can also be applied to explain the grain refining effect of Zr on Al-free Mg alloys and the poisoning effect of Al on Zr in Mg-Al alloys [25].

Apart from the above theories based on crystallography, a theory based on particle size effects is called the free growth model [26]. This model based on the earlier Maxwell-Hellawell's model [54] assumes that free growth of a crystal starts on a given particle at an undercooling inversely proportional to the diameter of the particle [26]. The equation deduced by Greer is given as follows:

$$\Delta T_{\mathrm{fg}} = 4\sigma/(\Delta S_V d_n) \qquad 2\text{-}4$$

where ΔT_{fg} is the free growth undercooling that constitutes a barrier for the effective initiation of a new grain, σ is the solid-liquid interfacial energy, ΔS_V is the entropy of fusion per unit volume and d_{n} is the diameter of nucleant particle [26]. The critical condition for free growth of a crystal through the minimum-radius hemispherical shape is when $d = 2r^*$, where r^* is the critical radius of a nucleus, a schematic illustration of the classical flat particle model is shown in Fig. 2-3 [26]. If $d < 2r^*$, there is a barrier for free growth due to the inherent requirement of reducing the radius of curvature of the interface when it grows [55]. In this case, the free growth of the crystal starting from the nucleant particle becomes possible only at greater undercooling by reducing the r^* [26, 55]. It should be noted that except for the classical flat particle model, heterogeneous nucleation on other shape substrate is also possible. In 1958, Fletcher [56] proposed the spherical substrate model, which provides new

insights and extends perspectives on heterogeneous nucleation and its control. More recently, Qian et al. [57] presents a rigorous thermodynamic formulation of the nucleation phenomena on a convex spherical substrate based on Fletcher's previous model. However, following paragraphs will still use the classical flat particle model in illustration for easy understanding.

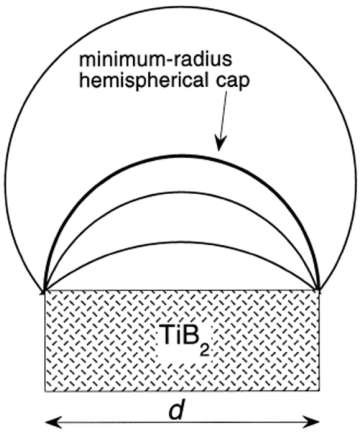

Fig. 2-3 Schematic illustration of the hemisphere created by grain initiation on one boride particle followed by free growth [26]

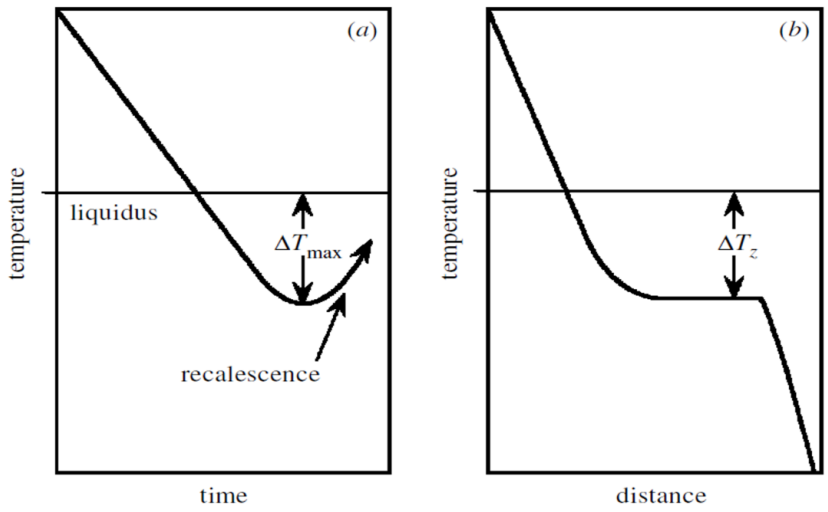

Fig. 2-4 Schematics of the thermal conditions during solidification. In case (a), a small, spatially isothermal melt shows recalescence. In case (b), a directionally solidified melt shows a quasi-isothermal zone [55]

As emphasized by Greer, the number of grains is limited by recalescence of the melt based on the free growth model, which in turn determines the final grain size [26]. The recalescence refers to the phenomenon that each growing crystal releases latent heat that is distributed

uniformly through the melt, slowing the rate of cooling, and eventually causing the temperature to rise. After the temperature has started to rise, there is no further initiation of free growth. Two simplified models have been proposed for the analysis of grain refinement during solidification: one is based on an isothermal melt [54] and the other one is based on directional solidification [58]. Fig. 2-4 shows the corresponding schematics of the two thermal conditions during solidification [55]. In each case the undercooling limiting the grain initiation is indicated.

According to Eq. 2-4, ΔT_{fg} is inversely proportional to d, which indicates larger particles have higher potency. As the melt is cooled below the liquidus temperature, free growth of crystals occurs first on the largest nucleant particles, and then on more, smaller particles. Greer et al. [26, 55] predicted that nucleant particles with an average diameter about 2 μm are most effective to act as heterogeneous nucleation sites (Fig. 2-5) [26]. Recently, researchers found that the optimized particle size of inoculation is controlled at 1 ~ 5 μm in most systems, such as Zr in Al-free Mg alloys [59] and SiC in AZ31 alloys [60]. Qiu's work [61] suggested that Al_2Y with diameter of 6 ~ 6.5 μm are effective nucleant particles in Mg-10 wt% Y (all compositions are given in wt% unless specified) cast alloy. However, this point is actually controversial because some nanoscale particles have been reported to act as heterogeneous nucleation sites [53, 62].

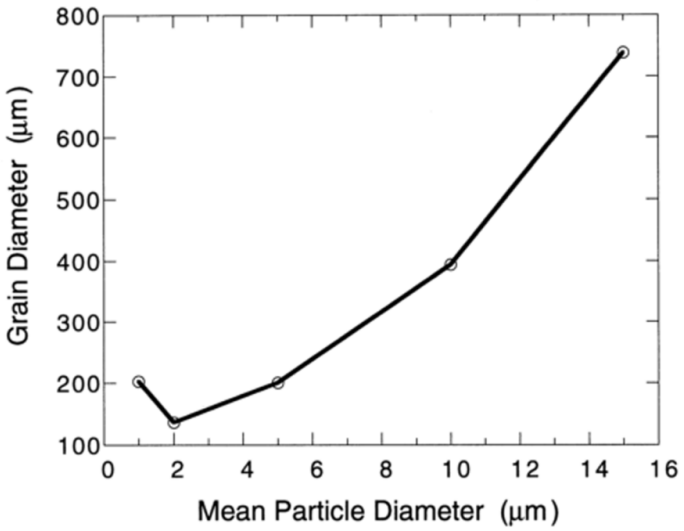

Fig. 2-5 The predicted grain size as a function of average inoculant particle diameter for grain refinement in Al alloy with Al-5Ti-1B refiner [26]

2.1.2 Solute paradigm theory

In general, solute segregation unavoidably exists during casting due to non-equilibrium solidification. The contribution of solute is related to the role of solute segregation in front of the solid-liquid (S-L) interface in restricting growth of grains and developing constitutional supercooling (CS, denoted as ΔT_{cs}). This provides a driving-force to activate further nucleation in the CS zone, and those newly formed grains can in turn restrict the growth of the previously-formed grains [63-68].

The growth restriction factor, Q, was used as a quantitative characterization parameter of the effect of solute on grain refinement. In a binary system, the value of Q can be simply calculated as follows [66]:

$$Q = m_l \ C_0 \ (k \ - 1) \qquad 2\text{-}5$$

where m_l is the slope of the liquidus line, k is the distribution coefficient, and C_0 is the composition of the solute in a binary alloy. It should be pointed out that Q is closely related to the rate of development of CS zone at the earliest stage of grain growth [69]. Higher value of Q means the CS-zone can be formed more rapidly, consequently, a better grain refinement effect could be obtained. The Q values of various alloying elements used in Mg alloys were provided by previous researches [4, 27], which were summarized in Table 2-1 (reordered with atomic number, some values in the table were changed/recalculated by retaining two decimal places).

For dilute systems and considering the absence of solute interactions, the overall Q values for a multicomponent alloy can be estimated by summing the Q values for each element (assumed to be i solute elements in total):

$$Q = \sum_i m_{l,i} \, C_{0,i}(k_i - 1) \qquad 2\text{-}6$$

where $m_{l,i}$ is the slope of the liquidus line, k_i is the distribution coefficient, and $C_{0,i}$ is the initial composition of solute element i [65]. However, for non-dilute alloys or in systems that element interacts with each other, this calculation needs to be revisited [69, 70] in detail.

Table 2-1 Slope of the liquidus line, m, distribution coefficient, k, and growth restriction factor, Q at C_0 = 1.0 %, of various alloying elements in Mg alloys, adapted from Ref. [4, 27]

Element	m	k	$Q = m\,(k-1)$	Element	m	k	$Q = m\,(k-1)$
Li	– 7.52	0.73	2.03	Nd	– 3.56	≈0.00	3.56
Na	– 6.88	≈0.00	6.88	Sm	– 3.40	0.14	2.92
Al	– 6.87	0.37	4.32	Eu	– 2.49	≈0.00	2.49
Si	– 9.25	≈0.00	9.25	Gd	– 2.60	0.61	1.01
Ca	– 12.67	0.06	11.94	Tb	– 2.99	0.31	2.06
Sc	4.02	1.65	2.61	Dy	– 2.35	0.65	0.82
Mn	1.49	1.10	0.15	Ho	– 2.20	0.61	0.86
Fe	– 55.56	0.054	52.56	Er	– 2.16	0.76	0.52
Co	– 3.18	≈0.00	3.18	Tm	– 1.58	0.65	0.55
Ni	– 6.31	≈0.00	6.31	Yb	– 3.07	0.17	2.53
Cu	– 5.37	0.02	5.28	Lu	– 0.68	0.82	0.12
Zn	– 6.04	0.12	5.31	Ir	– 1.65	≈0.00	1.65
Ge	– 4.41	≈0.00	4.41	Au	– 1.98	≈0.00	1.98
Sr	– 3.53	0.006	3.51	Hg	– 3.15	0.17	2.61
Y	– 3.40	0.50	1.70	Tl	– 3.32	0.82	0.59
Zr	6.90	6.55	38.29	Pb	– 2.75	0.62	1.03
Pd	– 4.07	≈0.00	4.07	Bi	– 1.81	0.15	1.54
Ag	– 4.22	0.37	2.66				
Cd	– 2.64	≈0.00	2.64				
In	– 2.68	0.86	0.38				
Sn	– 2.41	0.39	1.47				
Sb	– 0.53	≈0.00	0.53				
Ba	– 1.17	≈0.00	1.17				
La	– 2.90	≈0.00	2.90				
Ce	– 2.86	0.04	2.74				
Pr	– 2.91	≈0.00	2.91				

Another closely related parameter used to quantify the effect of solute on the grain size of a casting is termed as supercooling parameter, P, which is designated as:

$$P = \frac{m\ C_0\ (k\ -1)}{k} = \frac{Q}{k} \qquad 2\text{-}7$$

where m, k and C_0 are already defined in Eq. 2-5. P characterizes the largest growth restriction which could be achieved for a given composition, and corresponds to the maximum solutal undercooling, relevant for steady state growth of a planar front. In contrast, Q characterizes the degree of growth restriction for a small undercooling set independently [26], which is related to the initial rate of CS zone development. The difference between Q and P was illustrated previously in the Al-Ti system by Easton et al. [66, 67] and presented in Fig. 2-6.

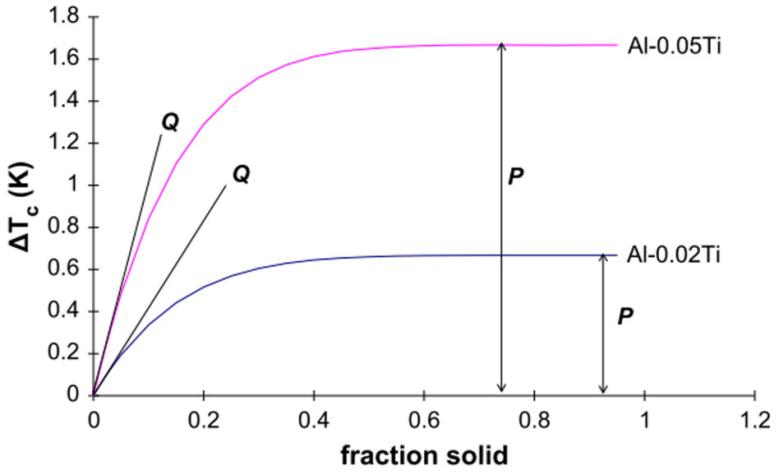

Fig. 2-6 Illustration of the value of Q as the initial rate of CS development and P as the maximum value in the Al-Ti system [67]

Most of the previous studies found that the measured grain sizes in castings comply with a better correlation based on Q [1, 4, 13, 26, 71-73], which indicates that a small initial undercooling determines the effectiveness of inoculation controlling by the growth restriction, rather than the maximum possible undercooling. In addition, comparing the Q values of Ti solute in Al alloy system with that of P, the Q values can be used to better explain the powerful grain refinement effect of Ti additions [64, 66].

Recent work by StJohn et al. [4, 74] proposed that the grain size, d_{gs}, for a wide range of alloys [74, 75] and solidification conditions with different cooling rates [76, 77], can be

related to Q by the following relationship:

$$d_{gs} = a + b/Q \quad (2\text{-}8)$$

where the intercept, a, corresponds to the number of particles that actually nucleate grains at infinite values of Q (generally lower value of a represents higher amount of activated nucleant particles), and the slope, b, is related to the potency of the nucleant particles where a steeper slope corresponds to a lower potency. Fig. 2-7 represents a typical grain size (d_{gs}) plotted against $1/Q$ showing the relationship [4]. As this relationship is a useful tool to evaluate the combining effects of both Q of the solutes in a melt and the potency of nucleant particles on the evolution of a grain structure, it is widely applied to assess the grain refinement efficiency.

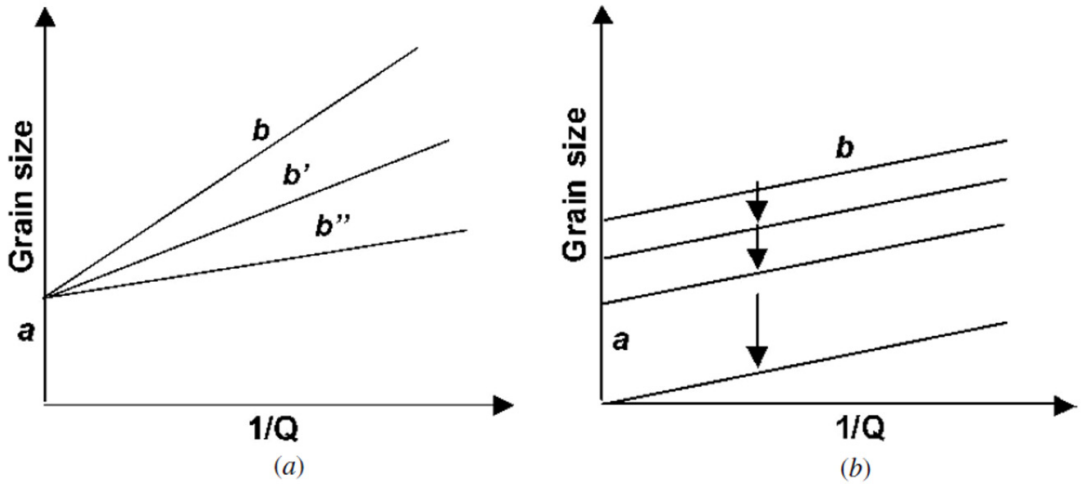

Fig. 2-7 (a) Effect of changing the nucleant particle potency on the slope b while keeping the number of particles constant. Particles that produce a slope b" are the most potent particles. (b) Effect of adding more particles on the value of a, while keeping the potency constant [4]

2.1.3 Interdependence theory

Considering the effects of both solutes and nucleant particles on grain refinement, StJohn et al. [3] proposed an interdependence theory to powerfully describe the relationship between grain formation and nucleant selection. This theory is based on assuming that grain formation is the result of the interdependence between nucleation and growth, which are closely related to surrounding alloy chemistry environment. The final grain size is determined by three major terms, as shown in Fig. 2-8 [3].

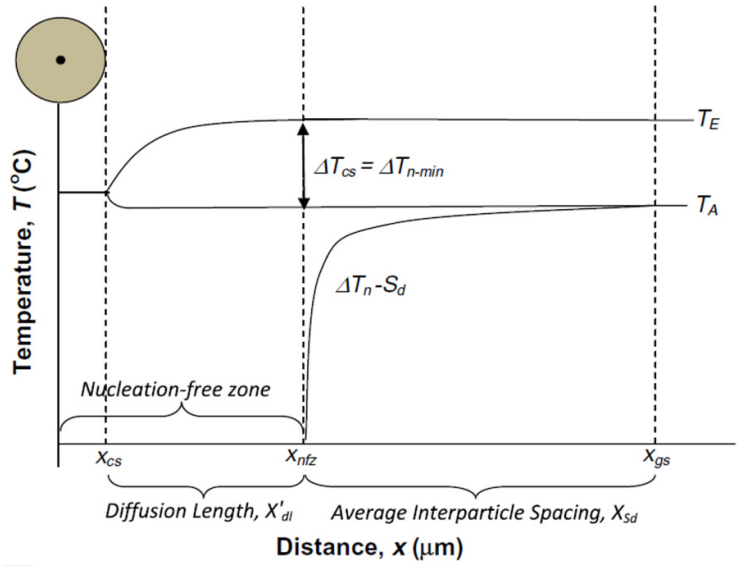

Fig. 2-8 Schematic representation showing the three regions that together establish the grain size of the microstructure: X_{cs}, X'_{dl} and X_{Sd}. The first two regions X_{cs} and X'_{dl} together represent a nucleation-free zone, where nucleation is not possible for the particle distribution described by $\Delta T_n - S_d$ [3]

The grain size (d_{gs}) of the microstructure can be simply expressed as:

$$d_{gs} = X_{cs} + X'_{dl} + X_{Sd} \qquad 2\text{-}9$$

The first term, X_{cs}, is the distance the previous grain must grow to generate sufficient CS (ΔT_{cs}) that can trigger nucleation on a particle with potency $\Delta T_{n\text{-}min}$ (i.e., requiring $\Delta T_{cs} \geq \Delta T_{n\text{-}min}$, where $\Delta T_{n\text{-}min}$ is the required nucleation undercooling of the most potent particle). The second term, X'_{dl}, is the diffusion length from the S-L interface at X_{cs} of the previously nucleated grain, to where ΔT_{cs} reaches its maximum value. The third term, X_{Sd}, is the distance from the end of the diffusion field to the next most potent nucleating site where a new nucleation event can take place (i.e., the average distance to the activated particles) [3]. The nucleation-free zone is denoted by the sum of X_{cs} and X'_{dl}, where ΔT_{cs} is always less than $\Delta T_{n\text{-}min}$ for the most potent particles within the distribution. This means that no new nucleation will occur as the amount of CS is not at the maximum value within this zone and therefore insufficient for triggering the new nucleation event on potent particles, which is illustrated in Fig. 2-9 [67]. Thus, the formation of a nucleation-free zone is a main reason to cause low particle efficacy in terms of a broad distribution of particle sizes. The previous research results illustrate this very well that

only a small proportion (1 ~ 2%) of the added inoculant particles contribute to the grain refinement [13, 55, 61, 74]. Therefore, in order to promote nucleation and grain refinement effect, it is critical to minimize the nucleation-free zone by control of alloy chemistry and/or growth rate [3, 67].

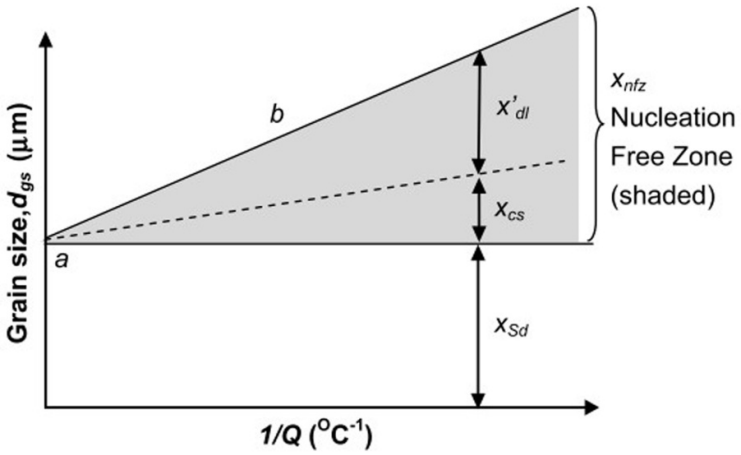

Fig. 2-9 A simple representation illustrating that for each value of Q, the grain size is the result of three components: X_{Sd} is the average distance to the activated particles and b is equal to the gradient of X_{cs} plus X'_{dl} over a unit of 1/Q (Eq. (2)). X_{Sd} is a constant when the particle number density is constant [67]

The interdependence theory improves the ability to predict as-cast grain size, to reveal the mechanisms of grain refinement, and to clearly explain why only a small proportion of added inoculant particles are operative. However, this theory also has limitations due to the lack of accurate thermodynamic and diffusion data used in the calculation, and some other variations such as crystallography and particle property are not considered. Future work should focus on the development of new and more effective grain refinement evaluation systems for cast metals by integrating the interdependence theory and other theories/models mentioned above.

2.1.4 Peritectic theory

The peritectic reaction theory was initially proposed by Asato and co-workers [78] based on the studies of silver, copper, and antimony alloys. Later this theory is applied in the case of grain refinement of $TiAl_3$ in Al alloys [79]. The peritectic reaction is defined as:

$$L(l) + \beta(s) = \alpha(s) \qquad 2\text{-}10$$

where L(l) is the liquid phase, β(s) and α(s) represent the solid phase before and after the peritectic reaction, respectively. Based on the peritectic theory, one solid phase β(s) that is suitable as nucleant particle reacts with the liquid phase L(l) to form a new solid phase, which is namely the primary α(s) phase.

For the application in Mg alloys, the peritectic theory is suitable to explain the grain refinement mechanism of Mg alloys by Zr. The powerful grain refining effect of Zr in Mg alloys was firstly discovered by Sauerwald [80] in 1947. The Zr particles separating from the liquid react with it at the peritectic temperature, thereby acquiring a layer of Zr-enriched solid solution [81]. More recently, it is widely accepted that peritectic-forming solutes do not only introduce potent nuclei into the melt and promote significant grain refinement via heterogeneous nucleation, but cause grain refinement by their segregation power [4, 82]. Considering the situation for grain refinement of Mg alloys with Zr, the undissolved Zr particles act as potent sites for heterogeneous nucleation, and the dissolved Zr with high growth restriction factor (Q) value allows to rapidly build up an effective CS zone ahead of the growing crystals [4, 27, 83-85], leading to the potent grain refinement.

2.2 Nucleation and growth

Effective refinement requires both heterogeneous nucleation and growth restriction, which are the two fundamental factors in grain refinement [2, 3]. For grain refinement, the inoculant particles added to the melt must be potent substrates for heterogeneous nucleation. However, the nucleation can occur only if the melt is sufficiently undercooled, i.e. the final grain size is determined by the balance of nucleation and growth that is controlled by the undercooling degree [26, 86]. Quested et al. [69] pointed out that the total solidification undercooling, ΔT is composed of four terms, including the kinetic undercooling, ΔT_k, the curvature undercooling, ΔT_c, the thermal undercooling, ΔT_t, and the constitutional supercooling (or undercooling) ΔT_{cs}, which is expressed as:

$$\Delta T = \Delta T_k + \Delta T_c + \Delta T_t + \Delta T_{cs} \quad 2\text{-}11$$

Only the CS (ΔT_{cs}) is available to drive diffusion of solute ahead of the solidification front. The thermodynamic driving force for solidification is the supersaturation, Ω, which is related

to Q and ΔT_{cs} [69]:

$$\Omega = \frac{C_0 - C_L^*}{C_S^* - C_L^*} \approx \frac{\Delta T_{cs}}{Q} \quad 2\text{-}12$$

where C_0 is defined in Eq. 2-5, C_S^* and C_L^* are the equilibrium solute compositions of the solid and liquid at the interface, respectively (Fig. 2-10). The rate of development of the CS zone at the earliest stage of grain growth plays a key role in determining the final grain size in castings. Hence, the basic aspects of development of the CS zone will be discussed in this section. In addition, heterogeneous nucleation is the main part resulting in grain refinement, which is derived from the classic nucleation theory, named as homogeneous nucleation, will also be reviewed in this section.

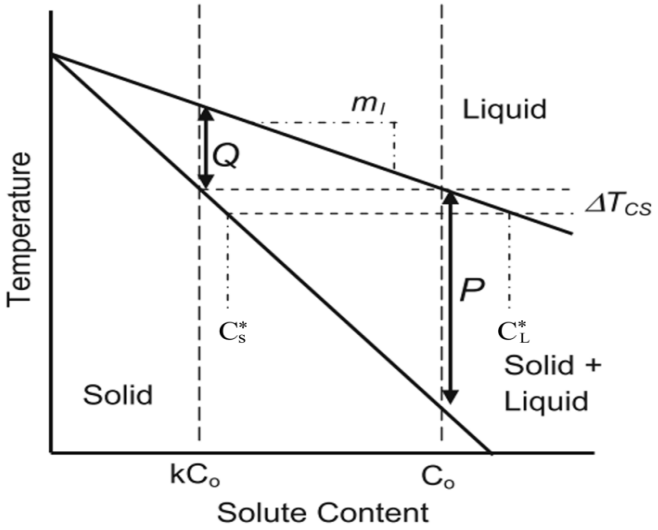

Fig. 2-10 Solvent-rich portion in a binary eutectic system, adapted from Ref. [67, 69]

2.2.1 Nucleation

It is well known that the formation of a stable nucleus requires sufficient driving force which derives from the competition between the energy required for the formation of a new interface and the volume free energy resulting from the phase change, i.e., from liquid to solid. For homogeneous nucleation, a nucleus forms within a melt without the aid of an external substrate or site, indicating a very large driving force is required to overcome the created energy of the new surface. For heterogeneous nucleation, the free energy barrier for nucleation on a substrate, ΔG_n^0, is given as follows [87]:

$$\Delta G_{\mathrm{n}}^{0} = \left(\frac{16\pi}{3}\right)\left(\frac{\sigma^{3}}{\Delta S_{f}\Delta T^{2}}\right) f(\theta) \qquad 2\text{-}13$$

where σ is the energy of the new interface, ΔS_f is the entropy of fusion, ΔT is the undercooling below the liquidus temperature and $f(\theta)$ can be calculated by:

$$f(\theta) = \frac{2-3\cos\theta+\cos^{3}\theta}{4} \qquad 2\text{-}14$$

where θ is the wetting angle between the liquid phase and the heterogeneous nucleation substrate (see in Fig. 2-11).

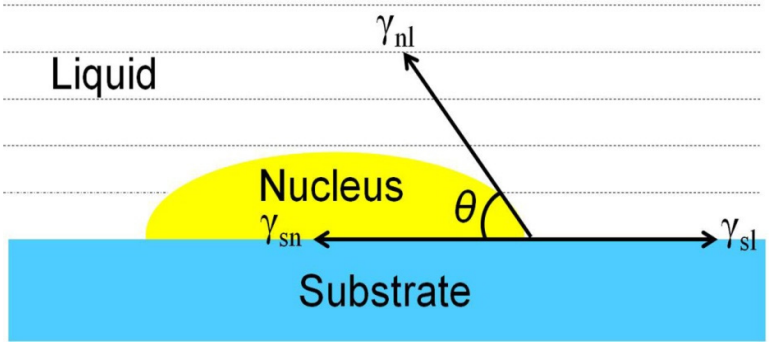

Fig. 2-11 Schematic representation of the contacting configuration between liquid, nucleus and substrate, reproduced according to Ref. [43, 88]

The θ is related to physical chemistry (wettability), statistical physics, long-range forces and fluid dynamics significantly affecting the nucleation progress [88]. The corresponding γ_{sn}, γ_{sl} and γ_{nl} in Fig. 2-11 are the interfacial energy between substrate and nucleus, the interfacial energy between substrate and liquid, and the interfacial energy between nucleus and liquid, respectively. In a steady state, the balance of the forces should follow the relationship by [88]:

$$\gamma_{sl} = \gamma_{sn} + \gamma_{nl}\cos\theta \qquad 2\text{-}15$$

According to Eq. 2-13, the $\Delta G_{\mathrm{n}}^{0}$ can be decreased by increasing the undercooling (ΔT) or by decreasing the wetting angle (θ). Small wetting angle between the liquid phase and the substrate indicates a small thermodynamic barrier to nucleation even at relatively low ΔT, which means a higher probability of a nucleation event occurring at this condition. However, too small wetting angle (< 10°) will lead to the failure of this model, because the spherical cap is below a mono-layer thick [43]. For encountering a very small wetting angle, Kim et al. [43]

proposed that nucleation occurs by the absorption of a mono-layer of solid on the nucleating substrate, which is known as the absorption theory. However, this process still needs a thermodynamic driving force for nucleation although its value is probably significantly lower than that calculated with the spherical cap analysis [66].

2.2.2 Grain growth and development of CS zone

More recently, Fan [25] pointed out that a successful nucleation event will result in a nucleus, but may not necessarily lead to a successful grain initiation depending on whether the free growth criterion is satisfied. Fig. 2-12 schematically illustrates the relationship between nucleation and grain initiation and then followed by free growth [25]. A small undercooling is required to allow the strained layer growth (epitaxial nucleation) for the creation of the initial solid layer of thickness h_c against the increasing elastic strain energy. Further undercooling is still needed to overcome the free growth barrier (curvature effect) for the hemisphere formation on the substrate if $\Delta T > \Delta T_{fg}$. Further growth beyond the hemisphere will be free (i.e., free growth), resulting in the formation of a new grain [25].

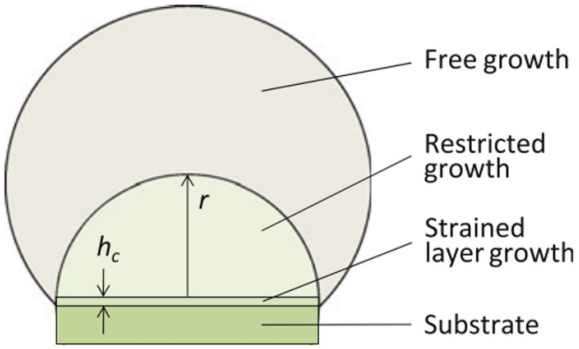

Fig. 2-12 Schematic illustration of epitaxial nucleation (strained layer growth) in relationship to the hemisphere created by restricted growth (grain initiation) followed by free growth [25]

The crystal growth rate can be calculated based on Maxwell and Hellawell's method, which is assumed that (a) the growth in the early stage can be regarded as spherical, not dendritic; (b) a near-isothermal melt was supposed in the condition of slow growth, so only the curvature and constitutional supercooling are significant, therefore the Eq. 2-11 can be rewritten by $\Delta T = \Delta T_c + \Delta T_{cs}$. Under these conditions, the radius of a growing spherical crystal, r, is given by [89]:

$$r = \lambda_s (D_s t)^{1/2} \quad 2\text{-}16$$

where D_s is the solute diffusion coefficient in the liquid, t is the time, and λ_s is an interfacial parameter, determined by $\lambda_s = f(S_g)$. The S_g is known as the growth parameter, which has been discussed in detail elsewhere [66, 90]. Differentiating Eq. 2-16 with respect to time, the growth rate of a spherical crystal, V, can be obtained as:

$$V = \frac{dr}{dt} = \frac{\lambda_s^2 D_s}{2r} \quad 2\text{-}17$$

As emphasized earlier, the rate of development of the CS zone at the earliest stage of grain growth plays a key role in determining the final grain size in castings. Easton and StJohn [66] proposed that the effects of the development of a CS zone on nucleation can be calculated by following assumptions: (a) comparing with the amount of CS, the negative thermal undercooling (ΔT_t) at the S-L interface due to unconstrained growth is negligible (see in Fig. 2-13, i.e., the dashed line was applied during the calculation to represent the actual temperature in the melt, assuming that the thermal gradient is zero); (b) sufficient substrates are presented and nucleation occurs as soon as the critical undercooling required for nucleation (ΔT_n) is achieved.

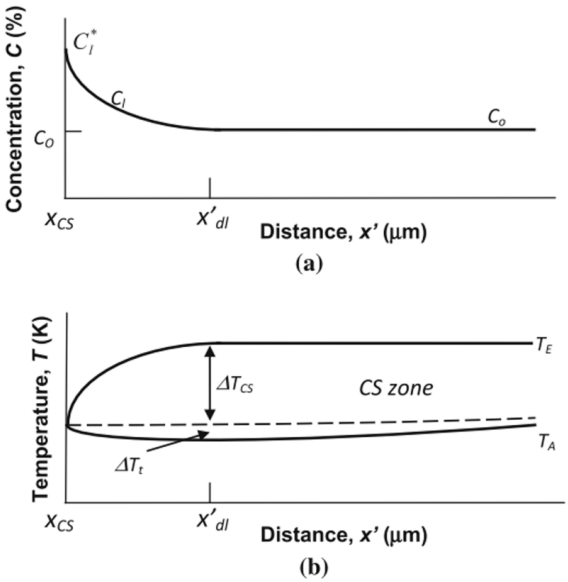

Fig. 2-13 Illustration of the development of the CS zone in front of a growing equiaxed grain: (a) the composition profile of the solute rejected in front of the growing S-L interface. (b) the corresponding temperature profile accompanied by the development of CS zone [66, 67]

Fig. 2-13 shows the CS zone produced during the growth of a grain. T_E and T_A are the equilibrium liquidus temperature and the actual temperature, respectively, which can be calculated by:

$$T_E = T_0 + m_l C_0 \quad 2\text{-}18$$

$$T_A = T_0 + m_s C_s \quad 2\text{-}19$$

where m_l and C_0 are already defined in Eq. 2-5. T_0 is the melting point. m_s is the slope of the solidus line. Therefore, the value of ΔT_{cs} can be calculated as:

$$\Delta T_{cs} = T_E - T_A = T_0 + m_l C_0 - (T_0 + m_s C_s) = m_l C_0 - m_l C_s/k = m_l (C_0 - C_l) \quad 2\text{-}20$$

where C_l and C_s represent the solute composition of the liquid and solid in front of the S-L interface, respectively. Other parameters are already defined previously elsewhere. Considering the slow diffusion nature in a solid phase, the Scheil equation is used to predict the solute redistribution that occurs during solidification, by assuming no diffusion of solute in the solid phase, while instantaneous diffusion of solute in the liquid phase, as given by:

$$C_l = \frac{C_0}{(1-f_s)^p} \quad 2\text{-}21$$

where f_s is the dimensionless term solid fraction, and $p = 1 - k$.

Substituting Eq. 2-20 into Eq. 2-21 to obtain the calculation expression of the development of CS (ΔT_{cs}) with solid fraction f_s:

$$\Delta T_{cs} = m_l C_0 \left(1 - \frac{1}{(1-f_s)^p}\right) \quad 2\text{-}22$$

Eq. 2-22 can be used to predict how effectively each element in the melt develops the CS that required for nucleation process by using the corresponding data in Table 2-1. In general, an increase in the rate of development of the CS zone decreases the time and amount of growth required for nucleation events to occur ahead of the interface, and thus smaller final grain sizes are obtained.

In addition, by assuming that the CS generated by a growing grain reaches the undercooling for nucleation of another grain (i.e., $\Delta T_{cs} = \Delta T_n$) on an adjacent nucleant substrate, the distance between those nucleation events determines the final grain size of the microstructure. The

relative grain size (RGS) that predicting the trend of grain size change for any binary alloy system can be given as [66]:

$$\mathrm{RGS} = 1 - \left(\frac{m_l C_0}{m_l C_0 - \Delta T_n}\right)^{1/p} \quad 2\text{-}23$$

This model accurately predicts the RGS and the trend of grain size change in Al and Al-Si alloys with grain refiner addition [3]. However, it should be pointed out that the latent heat and thermal gradients are not considered in this calculation.

2.3 Effect of elements on grain refinement

For the cast Mg alloys, the effects of different elements on grain refinement have been extensively studied in the last decade. Considering the Mg production processes, currently, Pidgeon process dominates the production of Mg in the world, especially in China [91]. The main four steps of a typical Pidgeon Process in China are shown in central blocks vertically in Fig. 2-14.

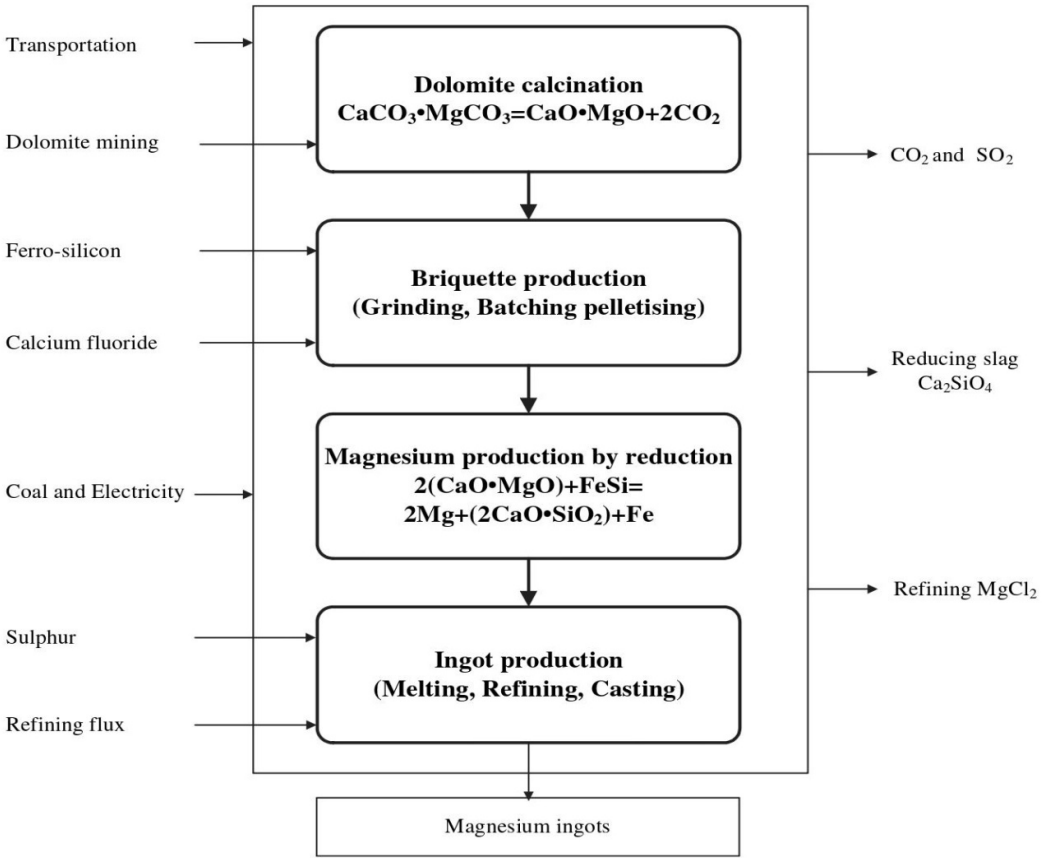

Fig. 2-14 Flow chart of Mg production by a typical Pidgeon process [91]

The materials on the left side of Fig. 2-14 are inputs and the ones on the right side are outputs. Therefore, it is reasonable to deduce that some minor/impurity elements, such as Fe, Si, Ca, Ni and Cr (the existence of Cr and Ni originates from the retorts used in the process, which are made of Ni-Cr-steel alloy), inevitably exist during the preparation of pure Mg ingots [21]. Mn and Zr elements are also included in this section because they are closely related to the present work. It should be noted that Cr and Ni are not discussed here due to the lack of data of grain refinement effects. Therefore, the effects of Fe, Mn, Si, Ca and Zr on the grain refinement of Mg alloys will be reviewed in this section, in order to give a much better understanding of the function of those elements.

2.3.1 Fe

Fe is notoriously detrimental to the corrosion resistance of Mg alloys. The upper limit of 50 ppm is specified for good corrosion resistance [21]. Liquid Mg melt dissolves approximately 180 ppm Fe at 650 °C, while increasing to approximately 400 ppm at 750 °C [92]. However, Fe has a very high Q value of 52.56, as shown in Table 2-1, indicating that the growth restriction effect of Fe is very impressive although its solubility is limited. Most of the researches support that Fe addition served as a grain refiner in both Al-free and Al-bearing alloys [1, 4, 81, 93-95]. However, grain coarsening with Fe addition was also reported [96, 97]. It has been noticed that the effect of Fe on grain refinement of Al-bearing Mg alloys has close relationship with three different grain refining methods, i.e. the Elfinal process, superheating, and native grain refinement. The Elfinal process [95] involves the addition of anhydrous $FeCl_3$ into Mg-Al melts at about 750 °C, where the most possible mechanism related to Fe-particles or Fe-containing intermetallics served as nuclei is proposed. However, this mechanism has not been established conclusively.

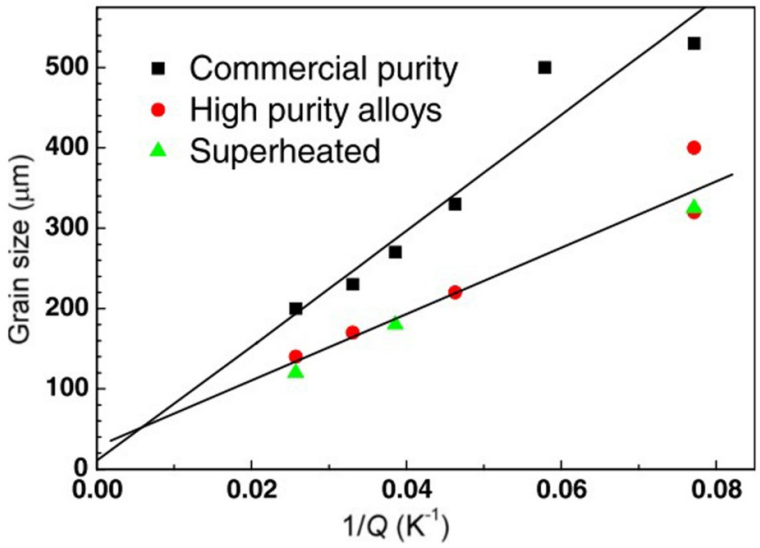

Fig. 2-15 Plot of grain size versus 1/Q for the experimental results obtained for a range of Mg–Al alloys. It is clear that high purity data and superheating data lie on the same straight line [98]

For superheating or native grain refinement in Mg-Al alloys, it is proved that their grain refinement effects are equivalent (Fig. 2-15) [98], indicating that the same mechanism is operating. More recently, StJohn et al. [1, 75] concluded that the actual mechanism for both superheating and native grain refinement is the thermal reinvigoration of the native grain refining particles as a result of the dissolution of the poisoning phases formed by Fe and Mn combining with Al. Unfortunately, the specific kinds of those native grain refining particles are still elusive. Although Cao et al. [98, 99] proposed that the native Al_4C_3 particles are most likely to be the potential nucleant particles responsible for grain refinement, the formation of Al_4C_3 is still questionable because no one shows its existence by credible characterization methods. In addition, it is doubtable where the carbon comes from as aluminium titanite (Al_2TiO_5) crucible was used in their experiments. Therefore, more detailed analyses are needed to focus on those native grain refining particles, which is the key process to understand the grain refinement effect in Mg alloys with Fe impurities.

2.3.2 Mn

As Fe inevitably exists in commercial purity Mg alloys, Mn is commonly used to remove the detrimental impurity Fe and improve the corrosion resistance [1]. In Mg-Al alloys, Mn easily combines with Fe to form Fe-Mn-Al intermetallics (in particular $Al_8(Mn,Fe)_5$) above the

liquidus temperature [100]. The solubility of Mn in pure Mg melt is about 2% at the melting point, but is reduced with increasing Al content in the melt [21]. Various Mn addition techniques are investigated because the melting point of Mn is relatively high. Recently, Cao et al. [101] investigated the effects of three different Mn additives, i.e. Al-60% Mn master alloy splatters, electrolytic Mn flakes and ALTAB^{TM} Mn75 tablets, on the grain refinement of high purity Mg-3Al, Mg-6Al and Mg-9Al alloy systems and commercial AZ31 alloys. Compared to electrolytic Mn flakes and ALTAB^{TM} Mn75 tablets, Al-60%Mn splatter leads to significant grain refinement in all the examined alloys, because it contains hexagonal close-packed (hcp) ε-AlMn phases, which are crystallographically favourable nuclei for Mg grains. Long time holding of the melt at 730 °C leads to an increase in grain size due to the transformation from the ε-AlMn phase to the more stable Al_8Mn_5 phase, which is less effective for the nucleation of Mg grains. However, based on the E2EM model calculation, Qiu et al. [36] proposed that the metastable τ-AlMn phase originated from the transformation of the high temperature ε-AlMn phase through rapid cooling is the preferred nucleant for α-Mg grains rather than the ε-AlMn, Al_8Mn_5 and β-Mn phase. Du et al. [18] found that Al-Mn intermetallic particles with molar ratio of 1:1, possibly identified as τ-AlMn phase, are considered as potent nucleants during solidification.

In addition, whether $Al_8(Mn,Fe)_5$ can be served as potent nucleation sites for α-Mg grains during solidification is still under debate. Zhang et al. [38] supported that $Al_8(Mn,Fe)_5$ is a potential nucleant based on the E2EM model calculation, but is much less efficient than either Al_4C_3 or Al_2CO. Laser et al. [102] pointed out that both Al_8Mn_5 and β-Mn(Al) formed prior to α-Mg can serve as potential heterogeneous nuclei during the solidification of Mn-modified AZ31 alloys. Kim et al. [103] found that the average grain size of Mg-9Al alloy was reduced from 480 μm to 61 μm by addition of 0.6% $MnCO_3$, which might attribute to the formation of potent nucleants such as Al_8Mn_5, MgO, and Al_4C_3 before solidification of α-Mg. However, Wang et al. [104] opposed this idea by their extensive TEM work on the Al_8Mn_5/α-Mg interfaces, revealing no crystallographic OR existed between the Al_8Mn_5 and α-Mg grains.

Another contradictive phenomenon is about the influence of Mn on the grain refinement of Mg-Al alloys inoculated by carbon sources. Easton et al. [13] concluded that the addition of

Mn poisoned the grain refining effect of Mg-Al alloys by SiC inoculation, probably due to the formation of less potent Al-Mn-carbides, such as $AlCMn_3$. However, Zhang et al. [19] proposed that the formed Al-C-Mn particles by the reaction between Al_4C_3 and Mn in AZ31 alloy inoculated by Al-5C master alloy could act as nucleating substrates for α-Mg grains. Liu et al. [20] reported that the grain size of AZ91D alloy inoculated by 0.6% Al_4C_3 can be further refined by small amount of Mn addition (< 0.27%). Nevertheless, Jun et al. [18] found that the addition of Mn had no obvious effect on the grain size of Mg-3Al alloy inoculated by 0.2% carbon. Therefore, the controversies of Mn addition on the grain refinement of Mg-Al alloys have not been resolved. One reasonable explanation is attributed to the complicated interaction between Mn and Al elements, as a result in which the formation of different types of Mn-Al phases depending on temperature and compositions will lead to totally different grain refinement effects. In order to understand the role of Mn in Mg alloys with or without carbon inoculation, the investigation with Al-free Mg alloys is possibly a key solution to understand the mechanisms.

2.3.3 Si

Si is also an alloying element which is commonly used in Mg alloys. Si can be added into molten Mg as elemental metallic Si, however, dissolving the Si is very difficulty due to its high melting temperature [65]. Therefore, Al-Si master alloy is an alternative approach to introduce the Si. Mg_2Si intermetallic phase can be commonly observed with the addition of Si [13, 14, 105, 106], which reduces the ductility and strength of the alloy both at room and high temperatures. Si has a relatively high Q value of 9.25, as shown in Table 2-1, Lee et al. [65] verified that a small addition of 0.15% Si fully converted the columnar grain structure of pure Mg into equiaxed grains. The grain size remained constant with further addition of Si. In addition, the combination of Si and other alloying element such as Ca [107, 108] can improve the grain refinement efficiency. More detailed work focused on the corresponding grain refinement mechanisms should be continued.

2.3.4 Ca

To date, most of the experimental results show that Ca can serve as an effective grain refiner for both Al-free and Al-bearing Mg alloys [8, 65, 109-111]. When Ca is added into Al-free Mg

alloys, the eutectic of α-Mg and Mg_2Ca phases are mainly formed [109, 112]. Different views [65, 109, 111] have been proposed for the explanation of the corresponding grain refinement mechanisms. Harandi et al. [111] pointed out that the significant grain refining effect with Ca addition is attributed to the strong growth restriction effect of solute Ca. However, Lee et al. [65] pointed out that besides the solute effect of Ca, some *in-situ* formed intermetallic compounds by the interaction between solutes and impurities might also contribute to nucleation process. In addition, Zuo et al. [109] indicated that the precipitated Mg_2Ca phase could also contribute to the grain refinement by restricting the growth of the grains.

For Al-bearing Mg alloys with Ca addition, Suzuki et al. [113] systematically investigated the solidification process of Mg-Al-Ca ternary alloys. They found that the intermetallic compounds in the eutectic structures formed during solidification are Mg_2Ca, $(Mg,Al)_2Ca$ and β-$Mg_{17}Al_{12}$ phases. In addition, the phase transformation from $(Mg,Al)_2Ca$ to Al_2Ca by a shear-assisted mechanism was verified during annealing at 573 K in Mg-5Al-3Ca alloy [113]. Although the grain refinement mechanism of Mg-Al alloys with Ca addition is still not fully understood, Jiang et al. [8] believed that the grain refinement of Ca addition in a twin-roll-cast Mg-3Al-1Zn alloy is attributed to the heterogeneous nucleation of α-Mg grains on *in-situ* formed Al_2Ca particles.

2.3.5 Zr

Zr is an extremely effective grain refiner for Mg alloys that contain no Al, Mn, Si, and Fe, because Zr forms stable intermetallic compounds with these elements. The grain refinement mechanism by Zr addition is already summarized in section 2.1.4, and various experimental results have been reviewed in detail elsewhere [1, 4, 27]. As Zr addition is an expensive approach, the main challenge is to reduce the consumption of Zr or find an alternative to substitute Zr in Al-free Mg alloys.

2.4 Effects of carbon-containing particles on grain refinement

Apart from the category of solutes effect on grain refinement of Mg alloys, another category by means of particle inoculations also plays an important role in grain refinement. Carbon-containing inoculant was known to be one of the most popular grain refining

treatments for Mg-Al alloys [1, 4, 114]. The grain refinement mechanisms in this area include carbon segregation, Al_4C_3, Al_2CO and Al_2MgC_2, which are still under debate. The major challenge is hard to identify the possible nucleant particles by using convincing characterization methods. Furthermore, the detection limit of carbon to date is equivalent to or even greater than the solubility of carbon in Mg [115-117], which makes it very difficult to evaluate the content of carbon. In this section, those grain refinement mechanisms are reviewed accordingly to give a better understanding of the role of carbon inoculation in Mg alloys, where carbon inoculation is defined as a grain refining method by using carbon-containing sources [4, 81]. The crystal structure, lattice parameters and calculated disregistries of Mg and various carbides are summarized in Table 2-2.

Table 2-2 Crystal structure, lattice parameters and calculated disregistries of Mg and carbides

	Crystal structure	Lattice parameter (nm)		Disregistry (%)	Reference
		a	*c*		
Mg	Hexagonal	0.3209	0.5210	0.00%	[118]
Al_4C_3	Rhombohedral	0.3388	2.4996	4.05%	[28]
Al_2CO	Hexagonal	0.3170	0.5078	1.23%	[38]
Al_2MgC_2	Hexagonal	0.3380	0.5822	5.32%	[14]
SiC	Cubic	0.4358	0.4358	4.00%	[118]

2.4.1 Carbon segregation

In 2003, Jin et al. [119] reported that the segregation of carbon could greatly affect the constitutional supercooling and restrict the grain growth in AZ31 alloys treated with carbon hexachloride (C_2Cl_6). However, Ma and Cao [115] did not agree with this hypothesis. Firstly, they concluded that grain refinement of Mg alloys by carbon inoculation must originate from the interaction between carbon-containing sources and Al, because Nucleant 5000 (supplied by Foseco GmbH, Germany, one carbon-containing source they tested) cannot refine the grains of Mg alloys that do not contain Al [115]. Secondly, the carbon segregation effect should be negligible because the solubility of carbon in a molten Mg alloy is very low (~ 20 ppm), and also most of the excessively added carbon would form carbon-containing compounds with other elements during solidification [115]. Therefore, the existence of potent

nucleant particles that promote heterogeneous nucleation is commonly accepted as a reasonable grain refinement mechanism in this system.

2.4.2 Al_4C_3

Early in 1966, Emley [81] concluded that Al_4C_3 nuclei play a major role in the grain refinement of Mg-Al type alloys by carbon inoculation. Furthermore, Lu et al. [28, 120] theoretically and experimentally examined the role of Al_4C_3 as a potent nucleus for Mg grain. They found that the addition of 1% Al_4C_3 particles to high purity Mg-3Al alloy results in significant grain refinement. In addition, they crystallographically calculated that the planar disregistry between Al_4C_3 and Mg is about 4.05% (see in Table 2-2), which falls in the potent range for heterogeneous nucleation as stated in section 2.1.1. More recently, the theory of Al_4C_3 formation by the reaction between carbon inoculation and Al element is supported by other researchers [121, 122]. Unfortunately, no direct or powerful evidence of the existence of Al_4C_3 particle is given in any of the results.

2.4.3 Al_2CO

Al-C-O type particles in Mg grains can be commonly observed by energy dispersive spectroscopy (EDS) analyses in Mg-Al alloys with carbon inoculation [110, 123]. Yano et al. [124] further proposed that these Al-C-O compounds are Al_2CO particles. Al_2CO is more potent than Al_4C_3 by considering the disregistry value in Table 2-2. Zhang et al. [38] also predicted that Al_2CO is the most effective nucleant for Mg grains compared to Al_4C_3 and $Al_8(Mn,Fe)_5$ by using E2EM model calculation. However, as the free oxygen content in the Mg melt is extremely low [125], the direct formation of Al-C-O compounds in the melt during solidification is thermodynamically impossible. Lu et al. [28] proposed that Al_4C_3 is the actual nucleating particle and the formation of Al-C-O compound is the result of the reaction between Al_4C_3 and water by the following reaction:

$$Al_4C_3\,(s) + 12\,H_2O\,(l) = 4\,Al(OH)_3\,(s) + 3\,CH_4\,(g) \qquad 2\text{-}24$$

Furthermore, Lu et al. [28] found that many open pores were observed in the sample of Mg-3Al alloy with carbon inoculation by aqueous metallographic preparation technique, which supports the reaction 2-24.

2.4.4 Al_2MgC_2

More recently, the ternary phase Al_2MgC_2 was observed in Mg-Al alloys inoculated by SiC particle [14, 15, 126, 127]. Compared to Al_4C_3 phase, the lattice parameter *c* of Al_2MgC_2 with a value of 0.5822 nm (see in Table 2-2) is very close to that of Mg supporting that Al_2MgC_2 is a potent nucleant particle. In addition, Mg_2Si phase can be verified by both X-ray diffraction (XRD) and scanning electron microscope (SEM) analyses [14, 15], indicating the following reaction happened:

$$2\ SiC\ (s) + 2\ Al\ (l) + 5\ Mg\ (l) = 2\ Mg_2Si\ (s) + Al_2MgC_2\ (s) \qquad 2\text{-}25$$

Furthermore, Huang et al. [14] confirmed the diffraction pattern of Al_2MgC_2 phase by using focused ion beam (FIB) and TEM analyses. But, Al_2MgC_2 would disappear at the later stage of observation and the reaction product $MgAl_2O_4$ formed [14].

Carbon inoculation works effectively for grain refinement of Mg-Al alloys, but a more powerful approach suitable for commercial production has long been desired. In addition, more detailed work to clarify the actual species of the nuclei is necessary.

2.5 Mg-Zn and Mg-Mn alloys

The alloying element Zn plays an important role on tailoring the properties of Mg alloys. Zn can effectively improve the strength of Mg especially if its content is higher than 3% [21]. In addition, the corrosion rate of Mg could be reduced by increasing the content of Zn [128]. Moreover, Mg-Zn alloys are known to be the most marked age hardening system in Mg base alloys [129, 130]. Nayeb-Hashemi et al. [92] pointed out that the control of the decomposition of supersaturated Zn in Mg by adjusting the temperature can produce a significant age-hardening effect. Furthermore, Zn is one of the most abundant nutritionally essential elements in the human body [131], indicating that Zn is suitable for biomedical applications. Zhang et al. [132] proved that a novel Mg-Zn binary alloy has good biocompatibility both in vitro and in vivo. Also, Zn is a good candidate to combine with other elements such as Al, Zr and RE to develop new alloy systems, which can be correspondingly divided into AZ-series alloys, ZK-series alloys and ZE-series alloys, respectively [21]. Microstructure, mechanical property, formability and corrosion behavior of those series alloys can be adjusted by the

control of the content of alloying element Zn.

The addition of alloying element Mn in Mg alloys can improve the formability, corrosion resistance and strength [21]. Similar to that of Zr with Mg, Mg-Mn binary alloy belongs to the peritectic system. However, compared to the role of Zr in the extruded Mg-10Gd alloy, Fang et al. [133] found that Mn is better to refine the grains of extruded alloy sample because α-Mn particles restrict recrystallization grain growth during extrusion. More recently, Wang et al. [134] reported that Mg-Mn alloys exhibit much higher strain-dependent damping values than that of pure Mg in the high strain region. Zhong et al. [135] concluded that the thermal conductivity of the as-extruded Mg-Mn alloys (Mn content > 0.5 at%) is higher than that of as-extruded binary Mg-Al and Mg-Zn alloys. Moreover, a series of newly developed Mg-Mn-Zn systems for future biodegradable applications have been attracted considerable attentions [136-139].

3 Motivations and objectives

Carbon inoculation using various systems, such as graphite, paraffin wax, lampblack, organic compounds, carbides and bubbling the melt with carbonaceous gases, is a feasible and economic grain refining treatment for Al-bearing Mg alloys. Moreover, a common view that carbon inoculation is only effective to Mg alloys that contain more than 2% Al is well accepted [4]. But recently Cao et al. [16, 17] found that the grain size of Mg-Zn alloy was reduced considerably by the addition of SiC nanoparticles. However, the corresponding grain refinement mechanisms are still not fully understood.

Considering that both the physical and chemical properties of SiC are totally different from other carbon-containing sources, the view of carbon inoculation only effective to Al-bearing Mg alloys may be debatable. Al-free Mg-Zn and Mg-Mn alloys with SiC inoculation were selected to investigate the grain refinement mechanisms.

The objectives of this study are given as follows:

- Optimize the experimental parameters of grain refinement by SiC inoculation for Mg-Zn and Mg-Mn alloys, including the addition amount, particle size, addition temperature and holding time.
- Reveal the effects of Mn and/or Fe on grain refinement of Mg-Zn and Mg-Mn alloys with SiC inoculation.
- Clarify the role of micro-alloying element Al on grain refinement of Mg-Zn alloys by SiC inoculation.
- Elucidate the interaction between heterogeneous nucleation and solute effects on grain refinement.
- Simulate the phase forming sequence of nucleation sites and α-Mg grains by Pandat software.
- Propose grain refinement mechanisms of Mg-Zn and Mg-Mn alloys by SiC inoculation.

4 Experimental procedures

4.1 Source materials

In this study, two different categories of Mg ingots based on their purity levels, i.e. commercial purity and high purity (HP) Mg, were applied for preparation of all the casting alloys. HP Zn ingots and commercial purity Al ingots were used as Zn and Al source materials, respectively. Commercial Mg-2Mn and Mg-33Zr master alloys were also used. The chemical composition of each source material was checked. Note that the chemical compositions of commercial purity Mg, HP Mg, and Mg-2Mn master alloy were analyzed using spark optical emission spectroscopy (Spectrolab M9, Kleve, Germany), and using X-ray fluorescence (XRF) analyzer (Bruker AXS S4 Explorer, Germany) for HP Zn, commercial purity Al and Mg-33Zr master alloy.

Based on the prediction that nucleant particles with diameter of about 2 μm are most potent to act as heterogeneous nucleation sites (section 2.1.1, Fig. 2-5), SiC particles with the average size of 2 μm (Alfa Aesar GmbH & Co KG, Germany) were selected as grain refiners. In order to investigate the effects of particle size on the grain refinement of Mg-Zn and Mg-Mn alloys by SiC inoculation, SiC particles with diameter of 0.1~1 μm (Goodfellow Cambridge Limited, England) and SiC particles with diameter of 10 μm (Lohmann Laborservice GmbH, Germany) were also used in this study. In addition, graphite powders with diameter of < 20 μm (Sigma-Aldrich Chemie GmbH, Germany) were used as another carbon source to test and compare their grain refining efficiency in Mg-Zn alloys. The morphology and size distribution of those particle sources were checked by SEM in detail.

4.2 Casting

Ingots and master alloys based on the designed chemical compositions were molten at 700 °C in an electrical resistance furnace using a mild steel crucible under a protective gas mixture of high pure Ar + 0.2% SF_6. The melt was manually stirred for 2 min and then the melt surface was skimmed. SiC or graphite particles preheated to 500 °C under Ar atmosphere were added into the melt directly. After that the melt was stirred vigorously at 100 rpm for 5 min to ensure

good dispersion of the particles and then held at 700 °C for 15 min before casting. Each sample was cast by pouring the melt into a mild steel mold preheated to 200 °C with a diameter of 70 mm at the bottom and 80 mm at the top and a height of 250 mm, followed by air cooling to room temperature. The wall thickness of the mold is 6 mm. Detailed nominal compositions of cast alloys based on above casting procedures are listed in Table 4-1.

Table 4-1 Nominal compositions of cast alloys

Experimental list	Nominal chemical compositions (wt%)
1	Mg-*x*Zn (*x* = 1, 1.5, 2, 3, 6)
2	Mg-*x*Zn-0.3SiC (*x* = 1, 1.5, 2, 3, 6)
3	Mg-3Zn-0.3SiC-*x*Al (*x* = 0.05, 0.1, 0.2, 0.3, 0.5, 1.0)
4	Mg-3Zn-*x*C (*x* = 0.3, 1.0, 10.0)
5	HP Mg-3Zn-*x*SiC (*x* = 0, 0.3, 0.5)
6	HP Mg-3Zn-0.3SiC-0.1Al
7	Mg-3Zn-0.3Zr
8	Mg-3Al-*x*SiC (*x* = 0, 0.3)
9	Mg-*x*Mn (*x* = 0.1, 0.2, 0.3, 0.5, 1.0)
10	Mg-*x*Mn-0.3SiC (*x* = 0.1, 0.2, 0.3, 0.5, 1.0)

Table 4-2 Detailed refining parameters used in Mg-3Zn and Mg-1Mn alloys. The two alloys were selected based on experimental list of 2 and 9 in Table 4-1, respectively

Refining parameter category	SiC size (μm)	Addition amount (wt%)	Addition temperature (°C)	Holding time (min)
I	0.1~1, 2, 10	0.3①, 0.5②	700	15
II	2	0.1, 0.2, 0.3, 0.5, 1.0, 5.0②, 10.0①	700	15
III	2	0.3①, 0.5②	700, 720, 740, 760	15
IV	2	0.3①, 0.5②	700	0, 15, 30, 60

Note that parameters of addition amount marked as ① were tested only in Mg-3Zn alloy, and ② were tested only in Mg-1Mn alloy. All of them are given in nominal chemical compositions

In order to study the effects of different refining parameters on the grain refinement of Mg-Zn

and Mg-Mn alloys by SiC additions, Mg-3Zn and Mg-1Mn based alloys were selected. Also, four base refining parameters were fixed, i.e., SiC particle size of 2 µm, SiC addition amounts of 0.3 and 0.5 wt%, addition temperature of 700 °C, and holding time of 15 min. These base parameters were varied in the four processing categories compiled in Table 4-2. They were tested correspondingly one by one.

4.3 Microstructure

4.3.1 Optical microscopy

Metallographic samples were transversally sectioned from the position of 20 mm away from the bottom of each ingot, which is shown in Fig. 4-1. Specimens for optical microscopy (OM) were cold mounted, ground with silicon carbide abrasive paper (grits size from 120, 500, 800, 1200, to 2500), polished with water-free colloidal silica and 1 µm diamond suspension. Then they were chemically etched in a solution of 8 g picric acid, 5 ml acetic acid, 10 ml distilled water, and 100 ml ethanol. After that they were quickly washed using ethanol and dried with blowing warm air. OM was performed with a Leica DMI5000 microscope. The average grain size was measured by the linear intercept method [140] from the micrographs taken using polarized light. Image analysis software named AnalySIS Pro was used to distinguish between neighbouring grains during grain size measurement.

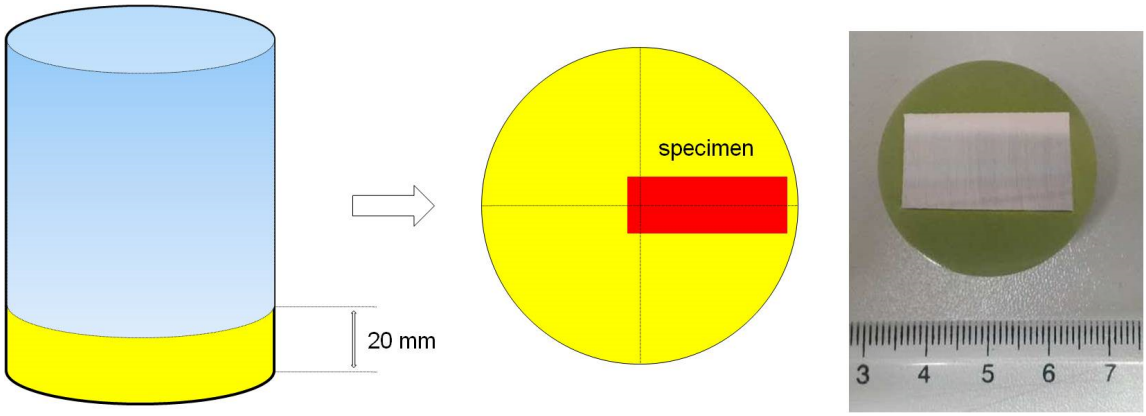

Fig. 4-1 Schematic illustration of a metallographic sample transversally sectioned from the position of 20 mm away from the bottom of an ingot and a correspondingly cold mounted specimen

In order to reflect the uniformity degree of the grain size for each ingot, grain size distribution diagrams were investigated as following: at least 50 counts of grain sizes were measured for each field and at least 5 fields were randomly selected from optical micrographs of each ingot to gather quantitative grain size data. The full grain size range on the horizontal axis was divided accordingly, e.g. each size range was set as 100 μm in Mg-Zn system. After that, the number of the grain size data located within each size range was counted respectively. Then, the counted number in one size range was divided by the total number of the measured grain size data, and its value reflects the frequency on the vertical axis for this size range. Note that no single value of grain size was extracted and used from these grain size distribution diagrams. Furthermore, all the grain size values appeared in this thesis were given in "average grain size". This follows the ASTM-definition of "average grain size" as the mean of data from the linear intercept method.

4.3.2 SEM analysis

Samples for SEM analysis were ground and polished with the same method described in optical microscopy. A Zeiss Ultra 55 SEM (Carl Zeiss GmbH, Oberkochen, Germany) equipped with EDS was used to observe the microstructures. Both EDS line-scan analyses and EDS mapping analyses were applied to analyze the chemical composition distributions of the selected areas.

4.3.3 FIB technology and TEM analysis

FIB technology using in a Nova-200 dual-beam SEM (Fig. 4-2) was applied to prepare site-specific TEM thin foils from a Mg-1Mn-0.3SiC alloy, in which the selected milling area contained the possible nucleant particle inside a grain. The thickness of the FIB-milled sample was measured in the SEM prior to examination in the TEM. The thin foils prepared by this method are of high quality. The TEM samples were examined in a Philips CM200 microscope operating at 200 kV.

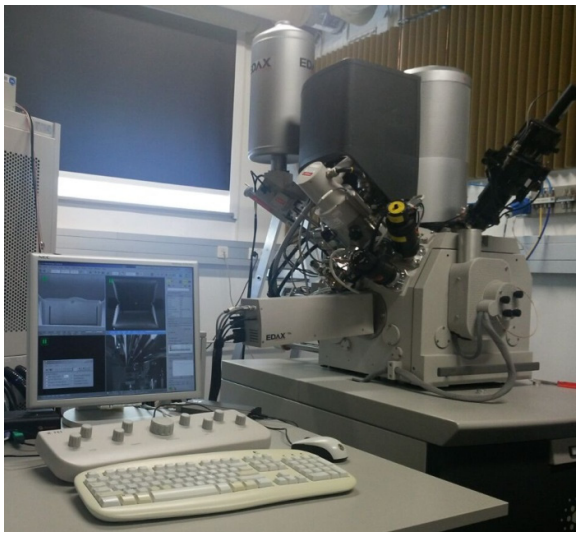

Fig. 4-2 A Nova-200 dual-beam SEM device equipped with FIB and EDS components

4.3.4 XRD analysis

For phase analysis, XRD was carried out with a diffractometer (Siemens D5000, Germany) equipped with Cu *K*α radiation. The XRD measurements were performed at 40 kV and a tube current of 40 mA over the 2θ ranging from 20^{o} to 90^{o}, using a step size of 0.02° with a dwell time of 3 s at each step. PANalytical X'pert HighSocre software with the International Center for Diffraction Data (ICDD) PDF2-2004 database was used to analyze the diffraction peaks of identified phases based on crystal structures.

4.4 Solidification simulation

Thermodynamic calculations to simulate the evolution of the second phases during solidification process in the present study were performed using Pandat software with the 2016 version of the PanMg database. In order to take into account the non-equilibrium solidification path, the Scheil model [141] was applied in the thermodynamic calculations. The Scheil model assumes that solidification occurs rapidly such that there is no chance for solute elements to diffuse in solid precipitates, while the liquid phase remains homogeneous even after the redistribution of the elements, and *local equilibrium* is assumed between the liquids and the solids [141]. During *normal Scheil simulation*, all phases are allowed to form without consideration of the nucleation barrier of different phases. The solid phase will immediately precipitate from the liquid when its thermodynamic stability conditions are met.

However, along the non-equilibrium solidification path, supercooling below the local S-L equilibrium may be sufficiently large to precipitate the "next stable phase" in *local metastable equilibrium* from the melt [142]. This could be modeled with *constrained Scheil simulation,* first proposed in Al–Si–P alloy solidification [143]. Both *normal Scheil simulation* and *constrained Scheil simulation* were used in the present study to check the type of the actual nuclei, which were validated by the FIB and TEM analyses in the Mg-Mn-SiC alloy system.

5 Results

5.1 Grain refinement of Mg-Zn-SiC alloys

5.1.1 Grain refinement of Mg-*x*Zn alloys

As mentioned previously, the additions of solute elements and nucleant particles are two key factors to determine the grain refinement effects of Mg alloys [1, 27]. Previous researches proved that the addition of solute element definitely affects the function of nucleant particles [13, 144]. Therefore, the independent role of solute element Zn in pure Mg is necessary to be checked first, which will contribute to the understanding of the role of SiC in binary Mg-Zn alloys. Furthermore, this is helpful to select a suitable Mg-Zn base alloy for the following inoculation process with SiC. In addition, the grain refinement efficiency of Mg-Zn alloys with SiC inoculation can be determined only when the grain sizes of corresponding binary Mg-Zn alloys were obtained.

Fig. 5-1 shows the microstructures and variations in average grain size of as-cast pure Mg alloy with different contents of Zn, i.e. Mg-*x*Zn (x = 1, 1.5, 2, 3, 6) alloys. As-cast pure Mg typically displays a coarse columnar structure [65]. The addition of 1% Zn into pure Mg leads to a transition from columnar to fully equiaxed grain morphologies. The grain size in Mg-Zn binary alloys with the content of Zn ≤ 2% is not uniform. With the addition of 3% Zn into pure Mg, small and homogeneous equiaxed grain morphologies were obtained. A gradual reduction in average grain size was observed in Fig. 5-1(f) with the increase of Zn content. From 1% Zn to 6% Zn in pure Mg, a significant reduction in average grain size from 624 ± 29 to 242 ± 9 μm was obtained.

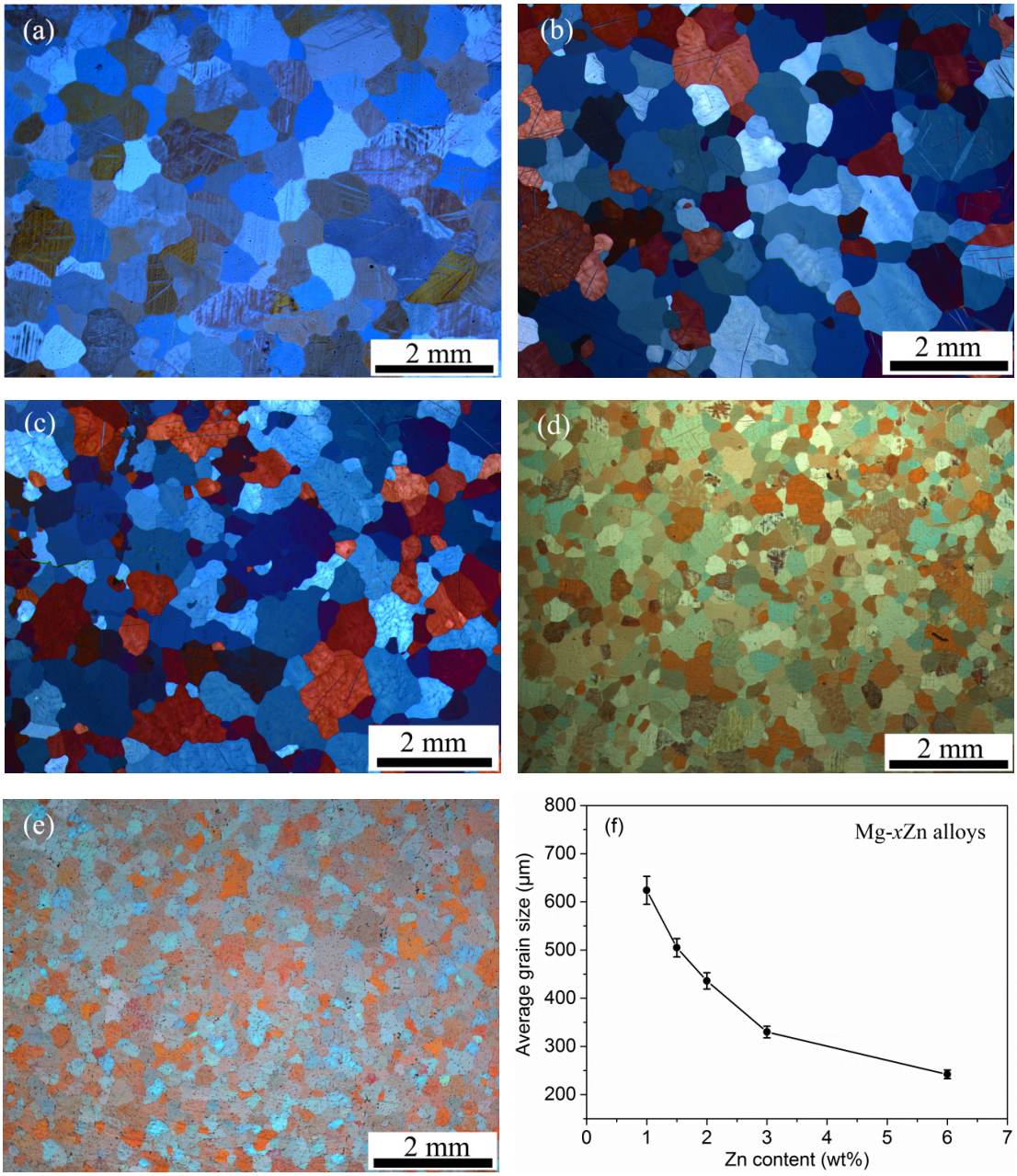

Fig. 5-1 Optical micrographs of as-cast alloys: (a) Mg-1Zn; (b) Mg-1.5Zn; (c) Mg-2Zn; (d) Mg-3Zn; (e) Mg-6Zn; (f) Changes in average grain size of pure Mg with different contents of Zn

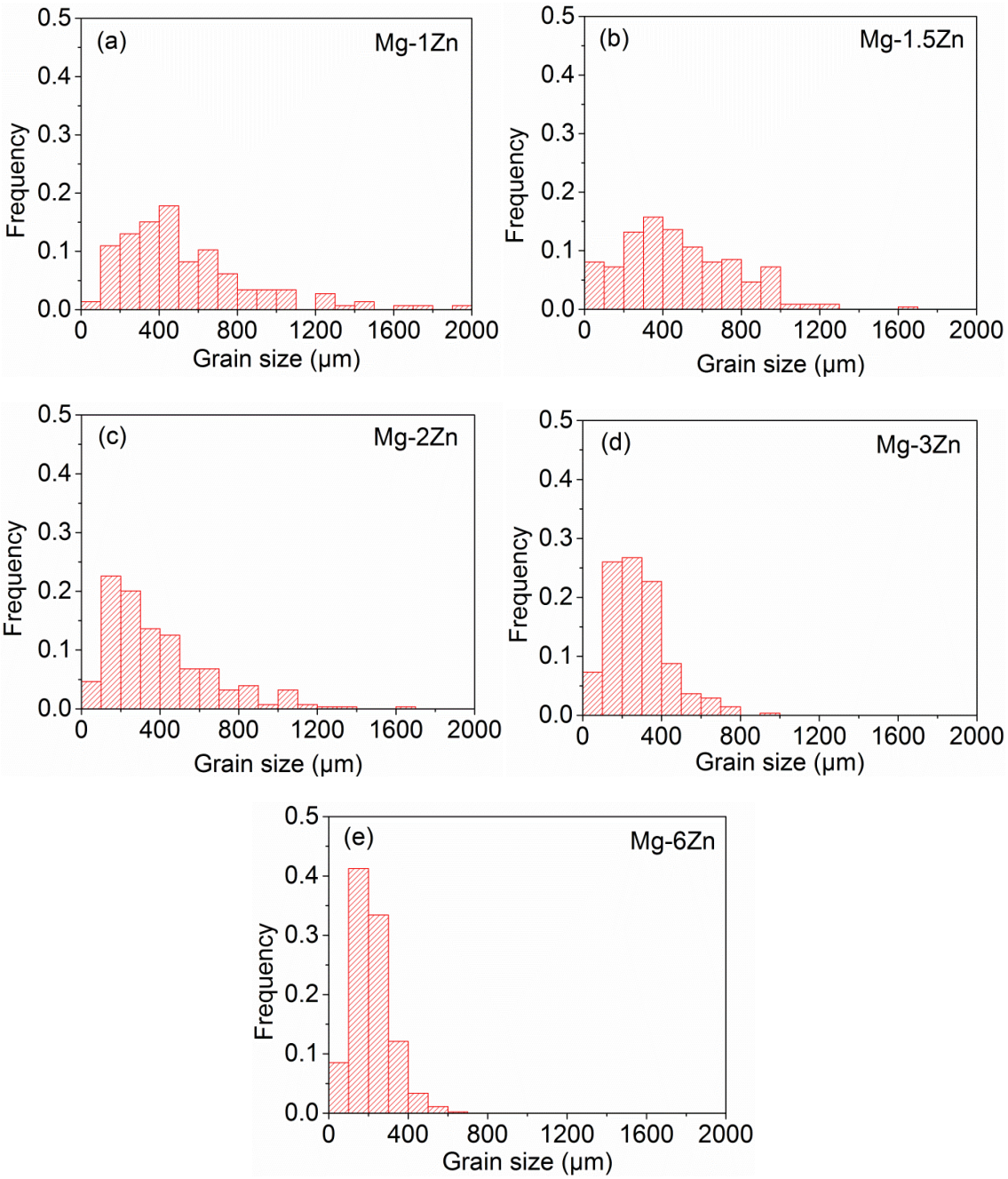

Fig. 5-2 Grain size distribution of as-cast Mg-xZn (x = 1, 1.5, 2, 3, 6) alloys

Fig. 5-2 shows the grain size distribution for Mg-*x*Zn (*x* = 1, 1.5, 2, 3, 6) alloys. The frequency of grain size distribution of Mg-1Zn was scattered in the size range from 0 to 2000 μm. Its maximum frequency is lower than 0.2 (note that the sum of the frequency is 1). These indicate that very inhomogeneous microstructure is formed in Mg-1Zn alloy. Similar grain size distributions were obtained in Mg-1.5Zn and Mg-2Zn alloys. The frequency of Mg-3Zn alloy was scattered in the size range from 0 to 1000 μm. The cumulative frequency value in

the range from 100 to 400 μm reaches to about 0.75 for Mg-3Zn alloy. Very narrow dispersion of grain size in Mg-6Zn alloy was obtained in Fig. 5-2(e). The maximum frequency in the range from 100 to 200 μm is higher than 0.4 for Mg-6Zn alloy. Its cumulative frequency value in the range from 100 to 400 μm reaches to about 0.87.

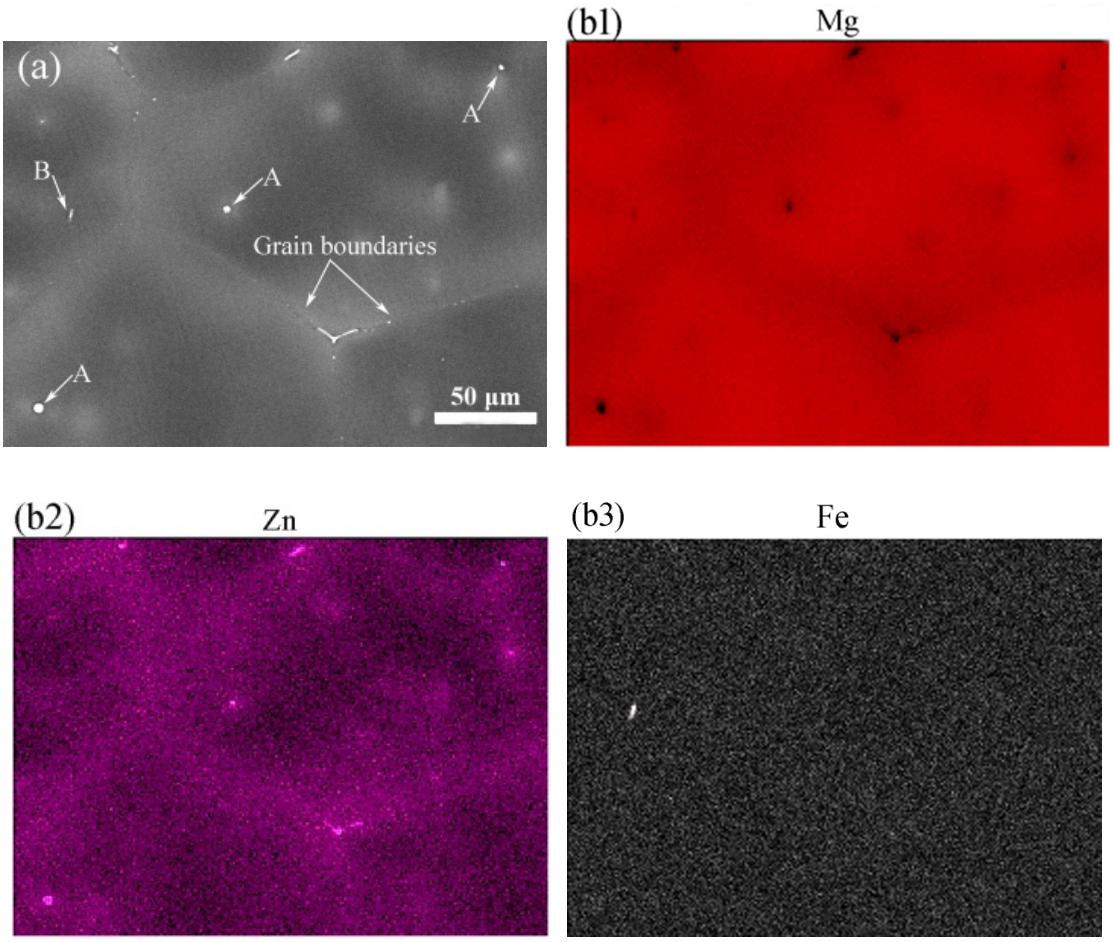

Fig. 5-3 (a) BSE image of the as-cast Mg-3Zn alloy; (b1–b3) EDS mappings of element distribution for Mg, Zn and Fe, respectively

Fig. 5-3(a) is a typical backscattered scanning electron (BSE) image for the as-cast Mg-3Zn alloy. Round-shaped particles (marked as A) with bright white contrast can be seen inside Mg grains. Further EDS analysis indicates the Mg/Zn ratio in these areas is approximate 2.2 to 2.8, which is close to that in Mg_7Zn_3 phase. EDS mappings of element distribution for Mg, Zn and Fe are shown from Fig. 5-3(b1) to (b3). It clearly shows that alloying element Zn severely segregates at the grain boundaries. It can be speculated that when a nucleated crystal formed during solidification, the alloying element Zn was rejected at the S-L interface. The rejected

Zn greatly affected the constitutional undercooling at the S-L interface and then restricted grain growth. The liquid around the crystal was therefore further undercooled, which allowed other crystals to nucleate more easily in this region. This process continued until at the end of solidification.

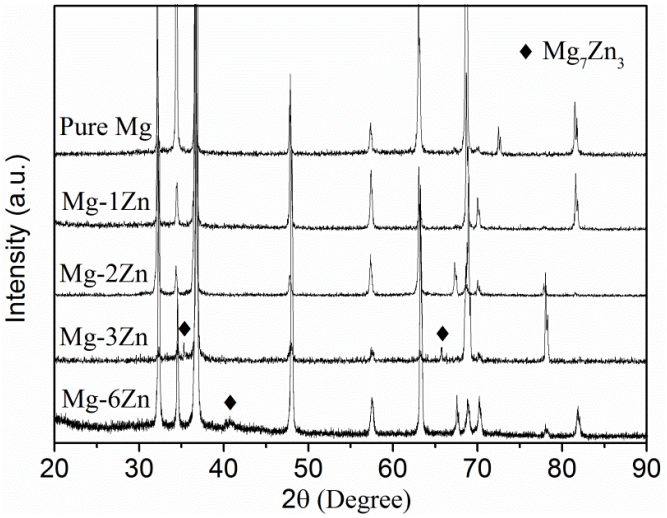

Fig. 5-4 XRD patterns of as-cast pure Mg and Mg-xZn (x = 1, 2, 3, 6) alloys. The peaks corresponding to Mg are not labeled

Fig. 5-4 shows the XRD patterns of as-cast pure Mg and Mg-*x*Zn alloys in order to identify the phases. It clearly shows that the intensities of Mg peaks changed with the addition of Zn content into pure Mg. In particular, no new phases were detected when the Zn content is less than 2%. However, peaks of Mg_7Zn_3 phases were identified in both Mg-3Zn and Mg-6Zn alloys by comparing them with pure Mg curve, which also support the EDS results of Mg-3Zn. This verified that Zn might consume some Mg to form Mg_7Zn_3 and then alter the solidification process of Mg. De Cicco et al. [145] also detected the Mg_7Zn_3 phase by XRD analysis for Mg-Zn binary alloy.

5.1.2 Grain refinement of Mg-*x*Zn-0.3SiC alloys

Fig. 5-5 shows the microstructures and variations in average grain size of as-cast Mg-*x*Zn (*x* = 1, 1.5, 2, 3, 6) alloys with the same addition of 0.3% SiC.

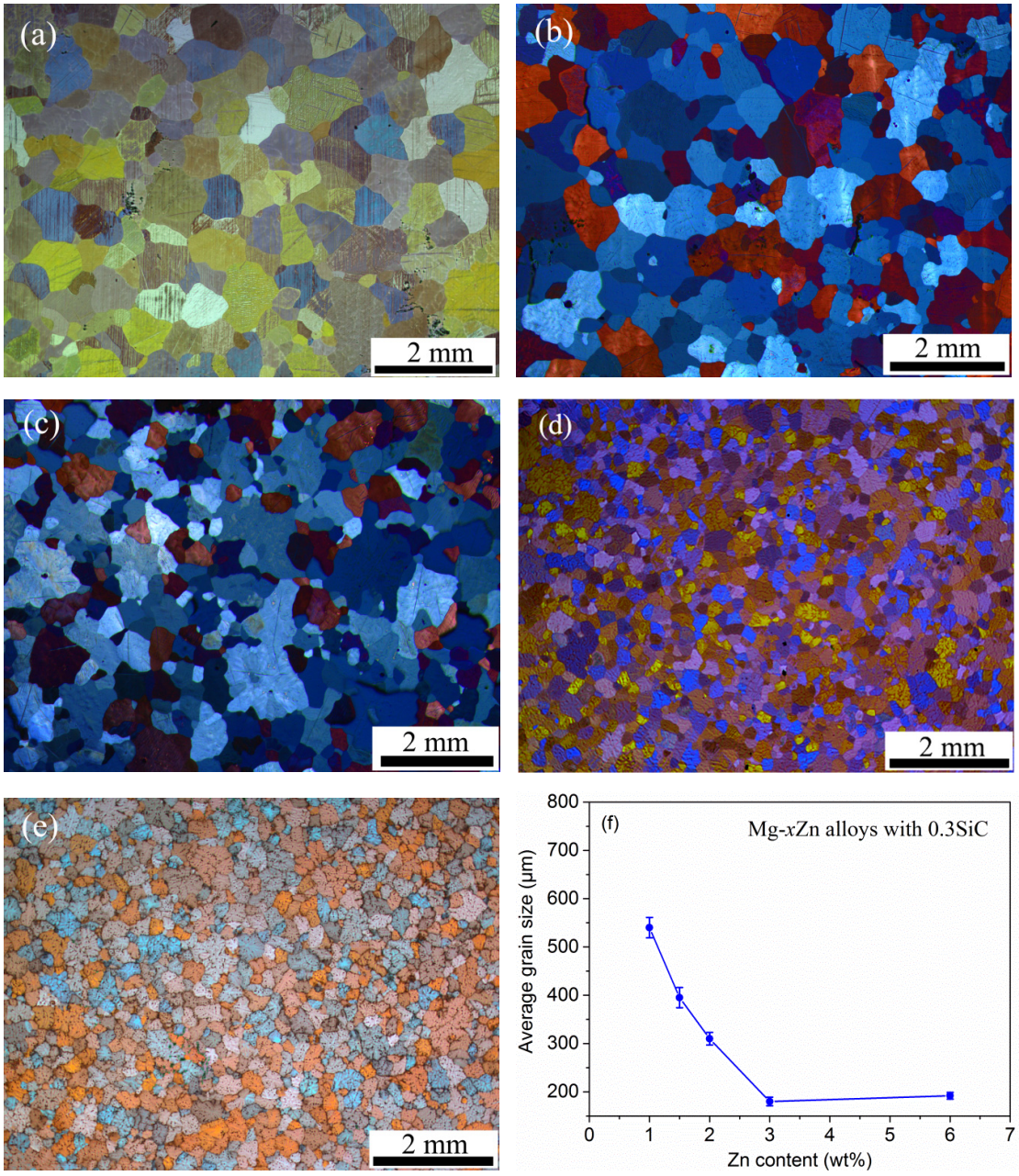

Fig. 5-5 Optical micrographs of as-cast alloys: (a) Mg-1Zn-0.3SiC; (b) Mg-1.5Zn-0.3SiC; (c) Mg-2Zn-0.3SiC; (d) Mg-3Zn-0.3SiC; (e) Mg-6Zn-0.3SiC; (f) Changes in average grain size of binary Mg-xZn alloys with 0.3% SiC

The average grain size of the Mg-*x*Zn-0.3SiC alloys decreased with the increase of Zn content, up to 3% Zn. It decreased significantly from 540 ± 21 μm for Mg-1Zn-0.3SiC alloy to 180 ± 9 μm for Mg-3Zn-0.3SiC alloy as shown in Fig. 5-5(f). Notably, small and homogeneous equiaxed grain morphologies were obtained with the addition of 0.3% SiC into Mg-3Zn and Mg-6Zn alloys. However, the grain size of Mg-6Zn-0.3SiC alloy is slightly larger than that of

Mg-3Zn-0.3SiC alloy, which means that higher content of Zn, i.e. 6% Zn, does not help to further refine the grains when the content of Zn already reaches to 3%.

Fig. 5-6 shows the average grain size comparison diagram of as-cast Mg-*x*Zn (*x* = 1, 1.5, 2, 3, 6) alloys prior to and after the addition of 0.3% SiC. It clearly shows that the average grain size of Mg-*x*Zn alloys decreased with the addition of 0.3% SiC in all the range of Zn content. This means that SiC is a good grain refiner in binary Mg-Zn system. Compared to the average grain size of 330 ± 12 μm for Mg-3Zn alloy, the average grain size for Mg-3Zn-0.3SiC alloy significantly decreased to 180 ± 9 μm. The alloys with lower (1%) or higher (6%) Zn content, however, has poor grain refinement effect with 0.3% SiC addition. The average grain size decreased from 624 ± 29 μm for Mg-1Zn alloy to 540 ± 21 μm for Mg-1Zn-0.3SiC alloy and from 242 ± 9 μm for Mg-6Zn alloy to 192 ± 7 μm for Mg-6Zn-0.3SiC alloy, respectively.

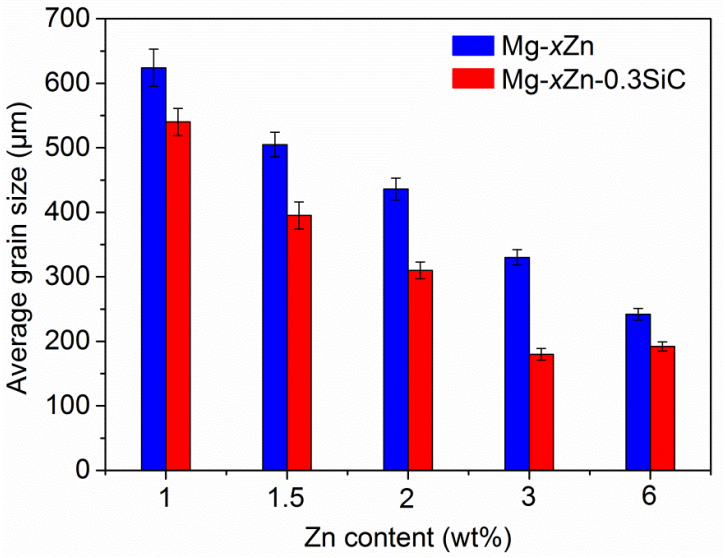

Fig. 5-6 Average grain size comparison of binary Mg-xZn alloys with and without 0.3SiC addition

Based on above results, the combination of 3% Zn and 0.3% SiC leads to the highest grain refining efficiency at the moment. Therefore, Mg-3Zn was selected as the base alloy for the following investigations. Whether the proper addition amount of SiC is 0.3% in Mg-3Zn alloys will be checked in section 5.1.3.1.

5.1.3 Effects of grain-refining parameters on Mg-3Zn-SiC alloys

5.1.3.1 Addition amount

Fig. 5-7 shows the changes in average grain size of as-cast Mg-3Zn alloy inoculated by different contents of SiC. It clearly shows a slight decrease of average grain size from 330 ± 12 to 285 ± 10 μm with the increase of SiC content from 0 to 0.2%. Then, a sharp decrease of average grain size from 285 ± 10 to 180 ± 9 μm was obtained with increasing of SiC content from 0.2% to 0.3%. After that, the average grain size remains relatively stable with the increase of SiC content, even up to 10% SiC.

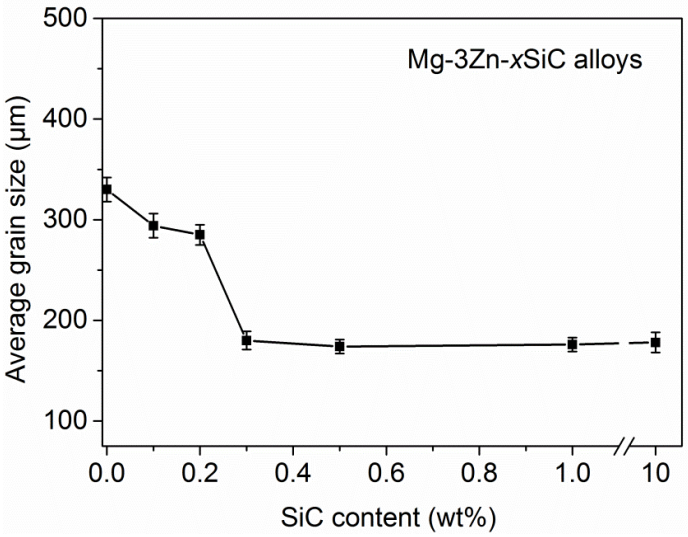

Fig. 5-7 Changes in average grain size of Mg-3Zn alloy inoculated by different contents of SiC

Fig. 5-8 shows the optical micrographs of as-cast Mg-3Zn-0.2SiC, Mg-3Zn-0.5SiC and Mg-3Zn-10SiC alloy. Homogeneous equiaxed grain morphologies were obtained in both Mg-3Zn-0.5SiC and Mg-3Zn-10SiC alloys. Compared with Mg-3Zn-0.2SiC (Fig. 5-8(a)) and Mg-3Zn-0.5SiC (Fig. 5-8(b)) alloy, SiC clusters that marked by black arrows in Fig. 5-8(c) were observed in Mg-3Zn-10SiC alloy, indicating that SiC is not well inoculated in Mg-Zn alloy with high content of SiC. Conversely, SiC can be added into the melt well and distributed uniformly within the matrix when the content of SiC was less than 0.5%.

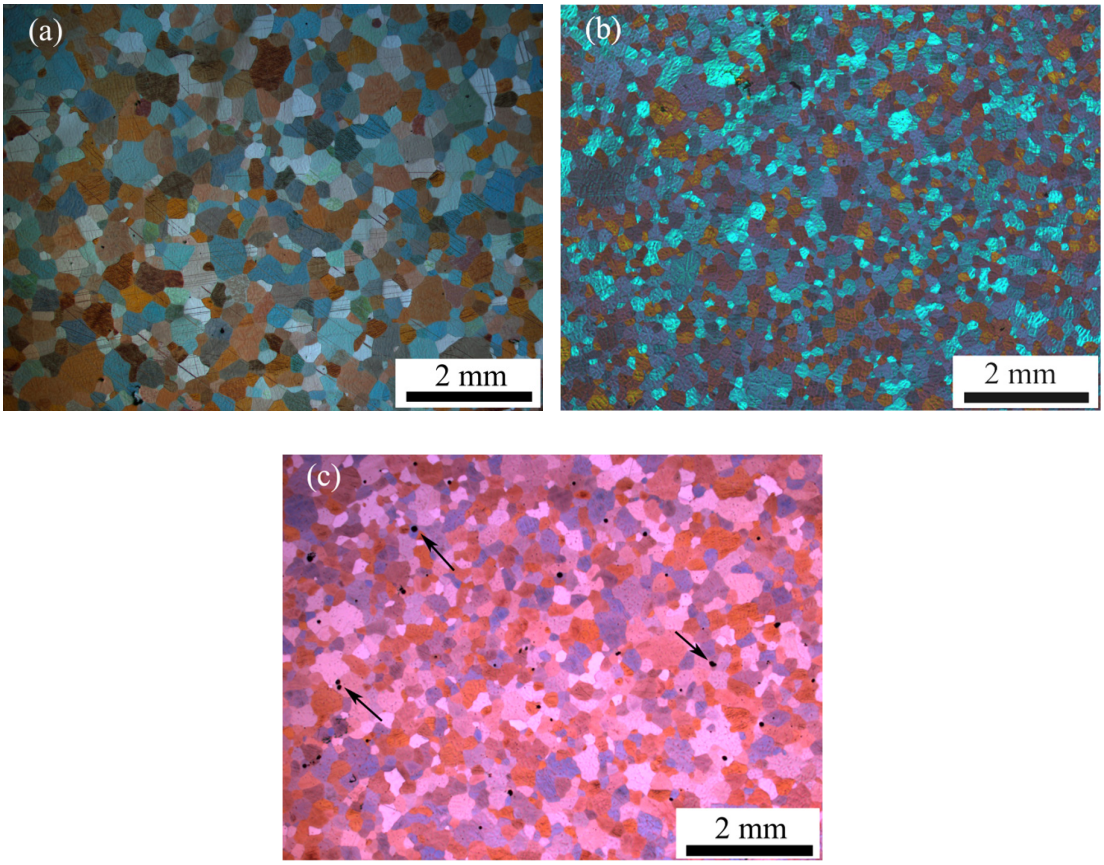

Fig. 5-8 Optical micrographs of as-cast alloys: (a) Mg-3Zn-0.2SiC; (b) Mg-3Zn-0.5SiC; (c) Mg-3Zn-10SiC

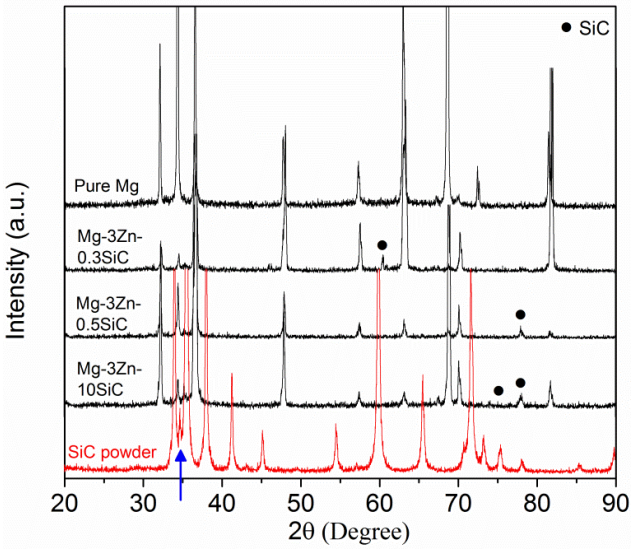

Fig. 5-9 XRD patterns of Mg-3Zn alloys inoculated with different contents of SiC. Patterns of pure Mg and SiC powder were used in comparison. The peaks corresponding to Mg are not labeled

Fig. 5-9 shows the XRD patterns of as-cast Mg-3Zn alloys inoculated with different contents

of SiC. A peak at 2θ = 60.4° appears in Mg-3Zn-0.3SiC alloy, which is closely matching the SiC phase at 2θ = 60.0° (PDF pattern No. 01-073-1664) that appears in SiC powder pattern. Peaks at 2θ = 78.1° in both Mg-3Zn-0.5SiC and Mg-3Zn-10SiC alloys are matching the SiC phase compared with SiC powder pattern. However, it should be noted that the peak around 2θ = 77.8° (PDF pattern No. 00-004-0770) could also belong to Mg phase peak, which clearly appears in XRD pattern of Mg-3Zn in Fig. 5-4. In addition, the peak of SiC phase at 2θ = 34.8° indicated by a blue arrow is closely overlapped with the peak of Mg phase at 2θ = 34.4°. These two factors make it even harder to characterize the SiC in those alloys with XRD analysis.

Fig. 5-10 is a typical BSE image of as-cast Mg-3Zn-10SiC alloy and its corresponding EDS mapping analysis. Alloying element Zn segregates at the grain boundaries, which is similar to that of Mg-3Zn alloy as shown in Fig. 5-3. Mg_7Zn_3 round-shaped particles were also detected inside Mg grains. It clearly shows that SiC clusters aggregated at the grain boundaries were identified by EDS mapping. This result agrees with the optical micrograph in Fig. 5-8(c) and XRD result in Fig. 5-9. The presence of element oxygen (O) could be due to the preparation of metallographic specimen, or it directly comes from the casting process.

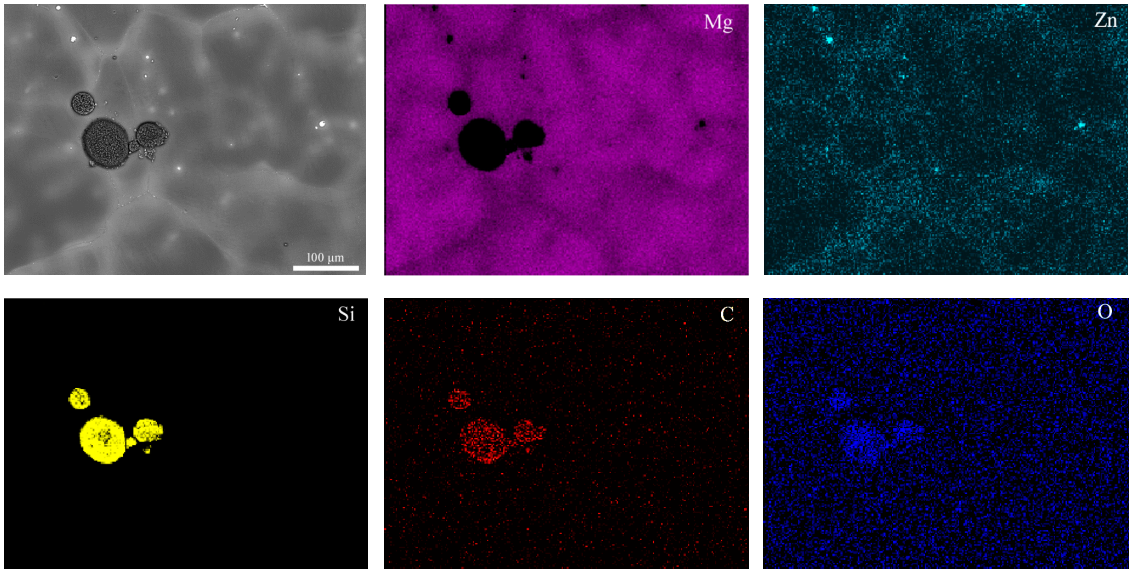

Fig. 5-10 BSE image of as-cast Mg-3Zn-10SiC alloy and corresponding EDS mappings of element distribution for Mg, Zn and Si, C and O respectively

Based on above results, SiC contents varied from 0.3% to 0.5% are the optimized addition

amount in Mg-3Zn alloys. As the grain refining efficiency of 0.3% SiC in Mg-3Zn is comparable to that of 0.5% SiC, and also in order to save the costs and narrow down the scope of investigations, 0.3% SiC addition was selected for Mg-3Zn alloy to test the influence of other parameters on grain refinement effect.

5.1.3.2 Effect of SiC particle size

SEM images of SiC particles with different sizes are shown in Fig. 5-11.

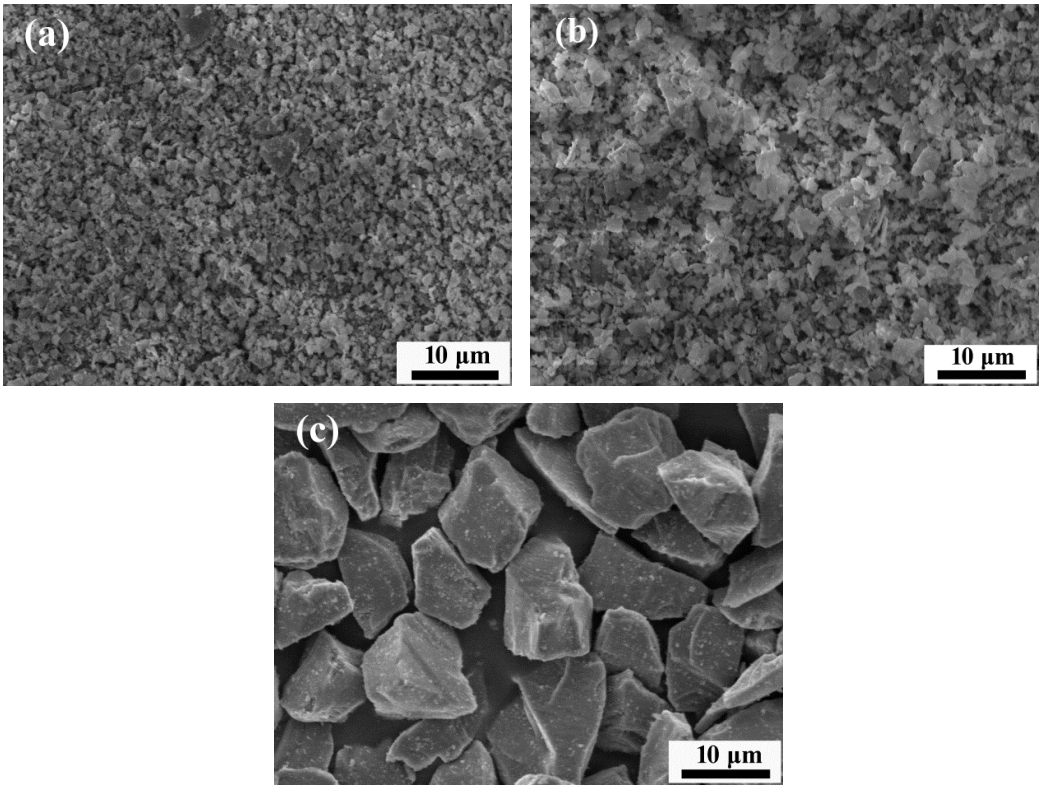

Fig. 5-11 SEM images of SiC particles with different sizes: (a) 0.1~1 µm; (b) 2 µm; (c) 10 µm

Fig. 5-12 shows the average grain size of Mg-3Zn alloy by adding 0.3% SiC with different particle sizes. Compared with the alloy inoculated by SiC particles in the form of 10 µm, the alloy inoculated by 0.1~1 µm SiC has relatively smaller average grain size. When SiC particles were added in the form of 2 µm, the refining effect is further improved. The average grain size of Mg-3Zn-0.3SiC (2 µm) reaches to 180 ± 9 µm.

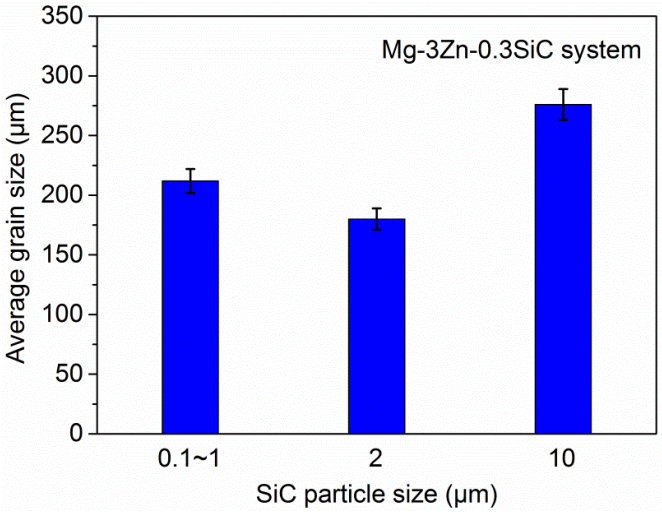

Fig. 5-12 Variations in average grain size of Mg-3Zn alloy by adding 0.3% SiC with different particle sizes

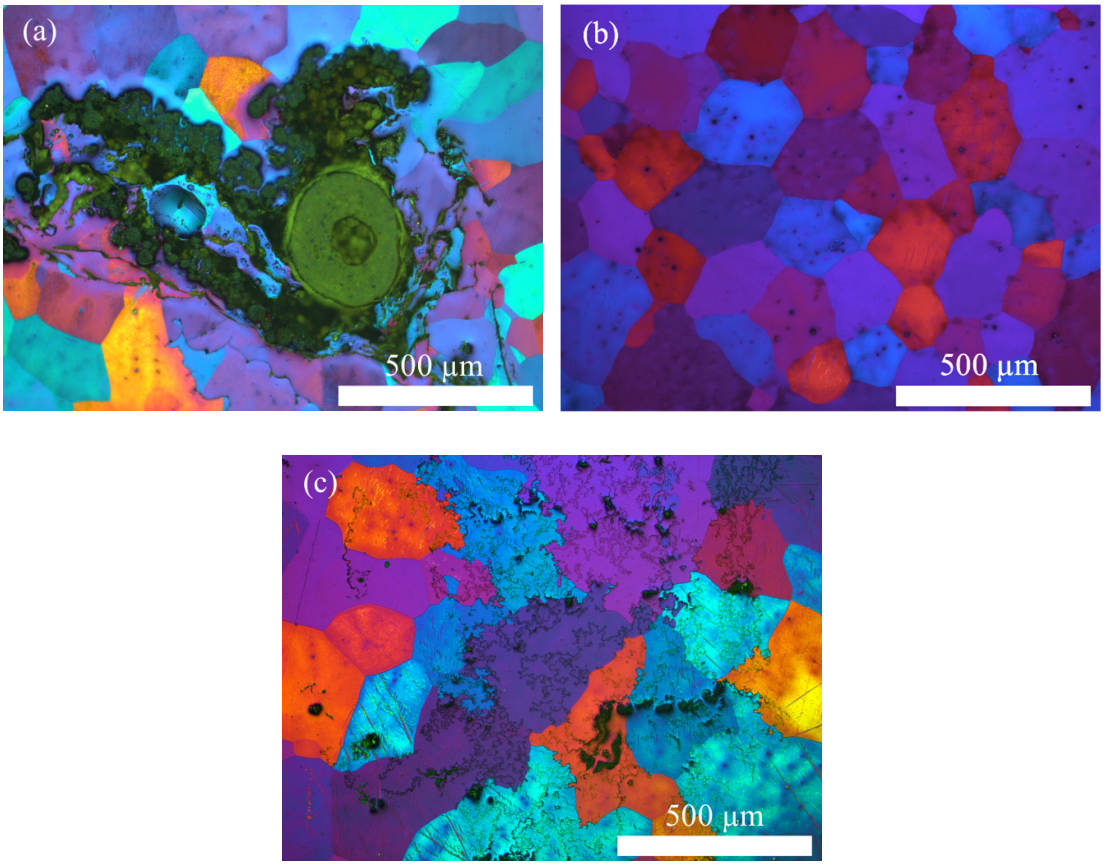

Fig. 5-13 Optical micrographs of Mg-3Zn alloy by adding 0.3% SiC with different particle sizes: (a) 0.1~1 μm; (b) 2 μm; (c) 10 μm

The corresponding optical micrographs of Mg-3Zn alloy by adding 0.3% SiC with different particle sizes are shown in Fig. 5-13. Very big SiC clusters were observed in Mg-3Zn-0.3SiC

(0.1~1 μm) alloys (Fig. 5-13(a)), verifying that sub-micrometer SiC agglomerated in the melt. Both SiC clusters and discontinuous SiC particles were found in Mg-3Zn-0.3SiC (10 μm) alloys (Fig. 5-13(c)), which means that the added SiC that has dissolved in the melt is little. Therefore, the refining effect is limited as shown in Fig. 5-12. Very few SiC particles can be detected in Mg-3Zn-0.3SiC (2 μm) alloys, which agrees with its optical micrograph with low magnification in Fig. 5-5(d).

Hereafter, Mg-3Zn-0.3SiC (2 μm) alloy system was selected to test the influence of following parameters, such as addition temperature and holding time on grain refinement effect, due to its highest grain refining efficiency.

5.1.3.3 Addition temperature

Fig. 5-14 shows the variation of average grain size with addition temperature for Mg-3Zn-0.3SiC alloy system. It shows that the average grain size gradually increases from 180 ± 9 to 272 ± 12 μm with the increase of addition temperature from 700 °C to 740 °C. After that, a sharp increase was observed when the addition temperature changes from 740 °C to 760 °C, which reflects that the grain refining effect is totally lost at such high addition temperature. The average grain size of the alloy with the addition temperature of 760 °C reaches to 446 ± 14 μm.

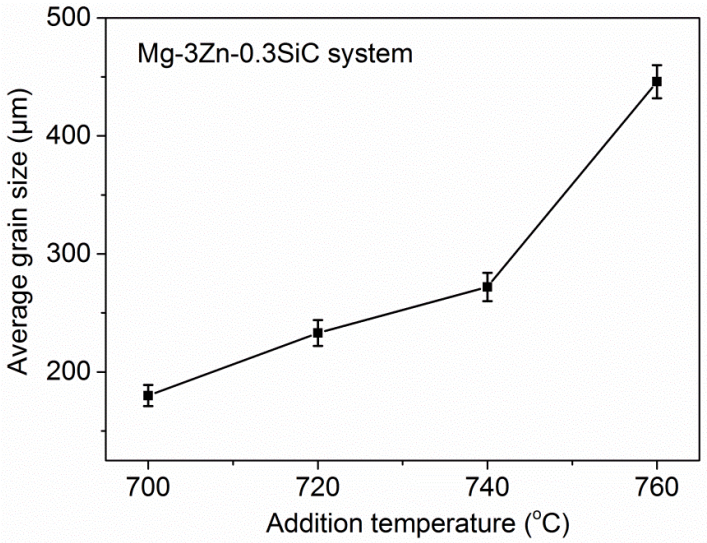

Fig. 5-14 Variation of average grain size with addition temperature for Mg-3Zn-0.3SiC alloy system

Fig. 5-15 shows the corresponding optical micrographs of as-cast Mg-3Zn alloy by adding 0.3% SiC particles under different addition temperature. Small and equiaxed grain morphologies basically maintained as the temperature rises from 700 °C to 740 °C, although the grain sizes became bigger with increasing the addition temperature. When the addition temperature is 760 °C, large amount of equiaxed grains were developed into columnar grains or irregularly round-shaped grains.

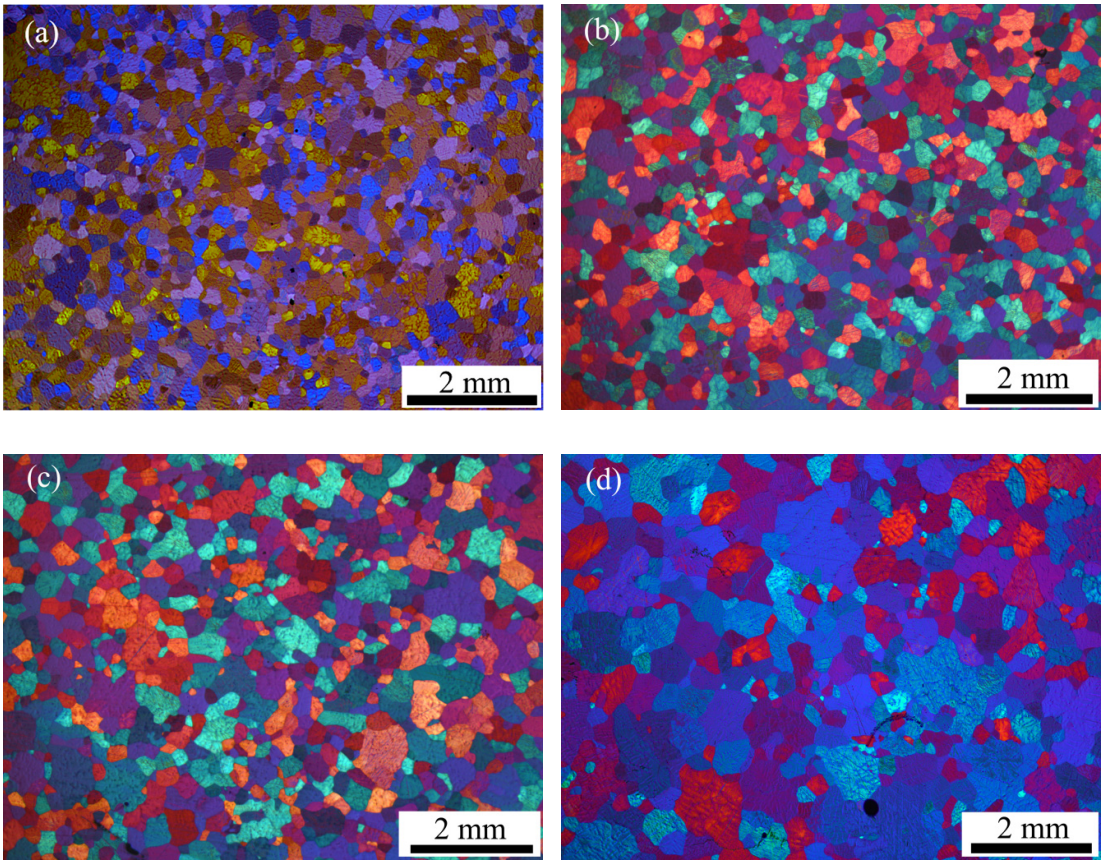

Fig. 5-15 Optical micrographs of as-cast Mg-3Zn alloy by adding 0.3% SiC particles under different addition temperature: (a) 700 °C; (b) 720 °C; (c) 740 °C; (d) 760 °C

5.1.3.4 Holding time

Fig. 5-16 shows the variation of average grain size with holding time for Mg-3Zn-0.3SiC alloy system. Firstly, the average grain size slightly decreases from 209 ± 13 to 180 ± 9 μm with the increase of holding time from 0 to 15 min. After that, the average grain size sharply increases from 180 ± 9 to 301 ± 19 μm with the increase of holding time from 15 to 60 min.

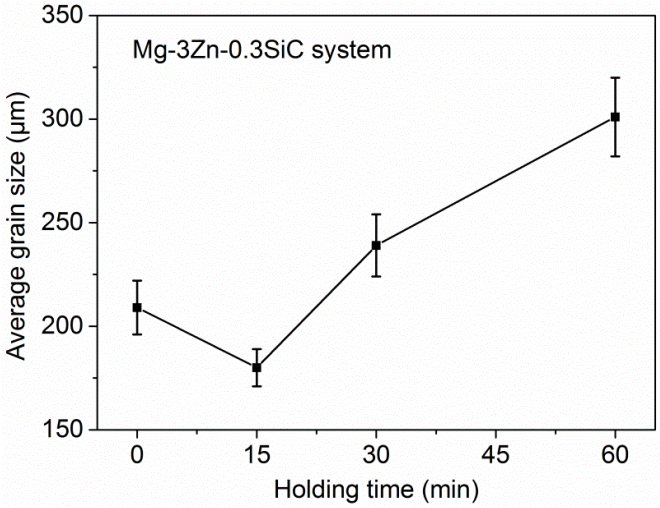

Fig. 5-16 Variation of average grain size with holding time for Mg-3Zn-0.3SiC alloy system

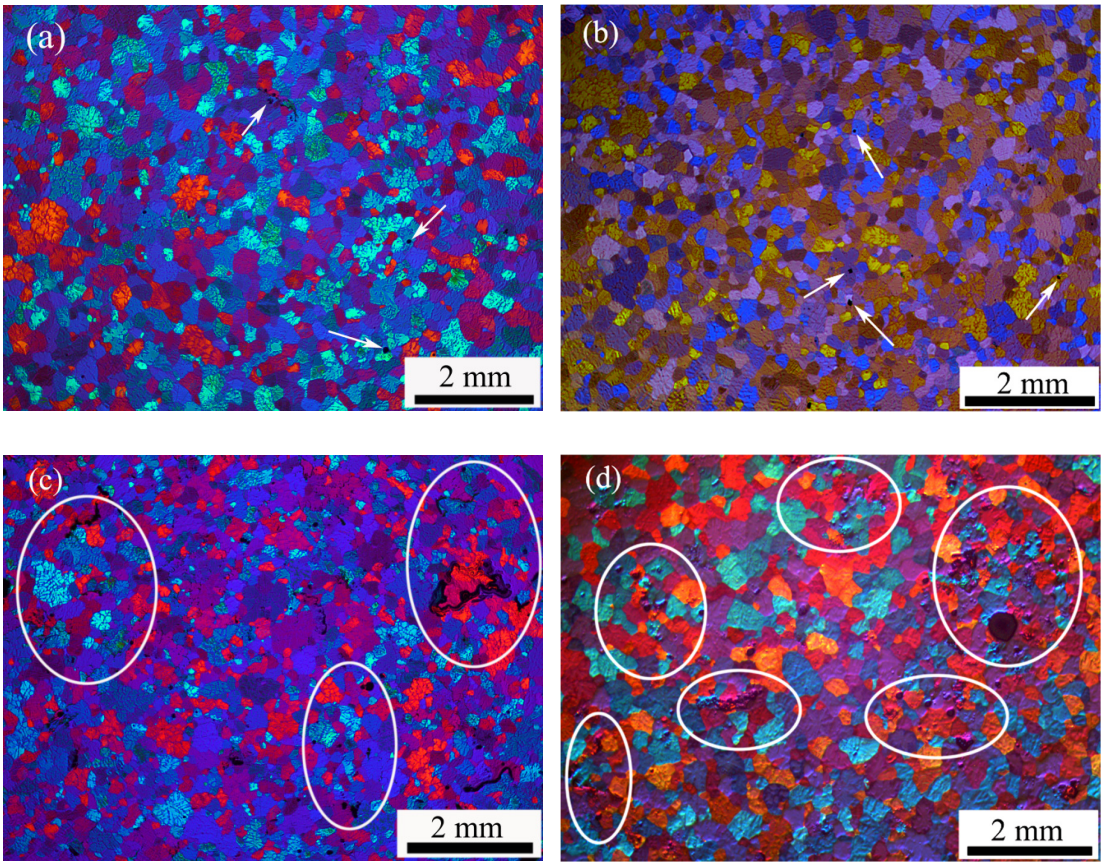

Fig. 5-17 Optical micrographs of as-cast Mg-3Zn-0.3SiC alloys under different holding time condition: (a) 0 min; (b) 15 min; (c) 30 min; (d) 60 min. Both white arrows and circles indicate the SiC aggregation areas

The corresponding optical micrographs of as-cast Mg-3Zn-0.3SiC alloys under different holding time condition are shown in Fig. 5-17. The grain morphologies did not change too

much between the holding time of 0 and 15 min. Some relatively big and irregularly shaped grains were observed when the holding time increasing to 30 and 60 min. Although the same amount of 0.3% SiC was added into those alloys, the aggregation of SiC became more severe with the increase of holding time. Especially, large amount of SiC clusters (marked as white circles in Fig. 5-17(c) and Fig. 5-17(d)) were found in alloys with the holding time of 30 and 60 min.

5.1.4 Characterization of nucleant particles in Mg-Zn-SiC alloy system

Fig. 5-18(a) shows a feature of a nucleation site obtained in Mg-3Zn-0.3SiC alloy that detected by EDS line-scan analysis in Fig. 5-18(b). In backscattered electron image, the black part enriched with Si and C between both the inside white and outside white part can be confirmed as a SiC particle. Firstly, this particle has even darker contrast than that of Mg matrix suggesting that its average atomic number is less than that of Mg matrix. In addition, the length of the black part particle is about 2.1 μm, which is very close to the original size 2 μm of the SiC particle. The inside white part was enriched with Fe and Mn, indicating that SiC is likely to associate/react with Fe and Mn to serve as nuclei for α-Mg grains. Moreover, the SiC was wrapped by the outside white part, which is confirmed as the Zn enriched area.

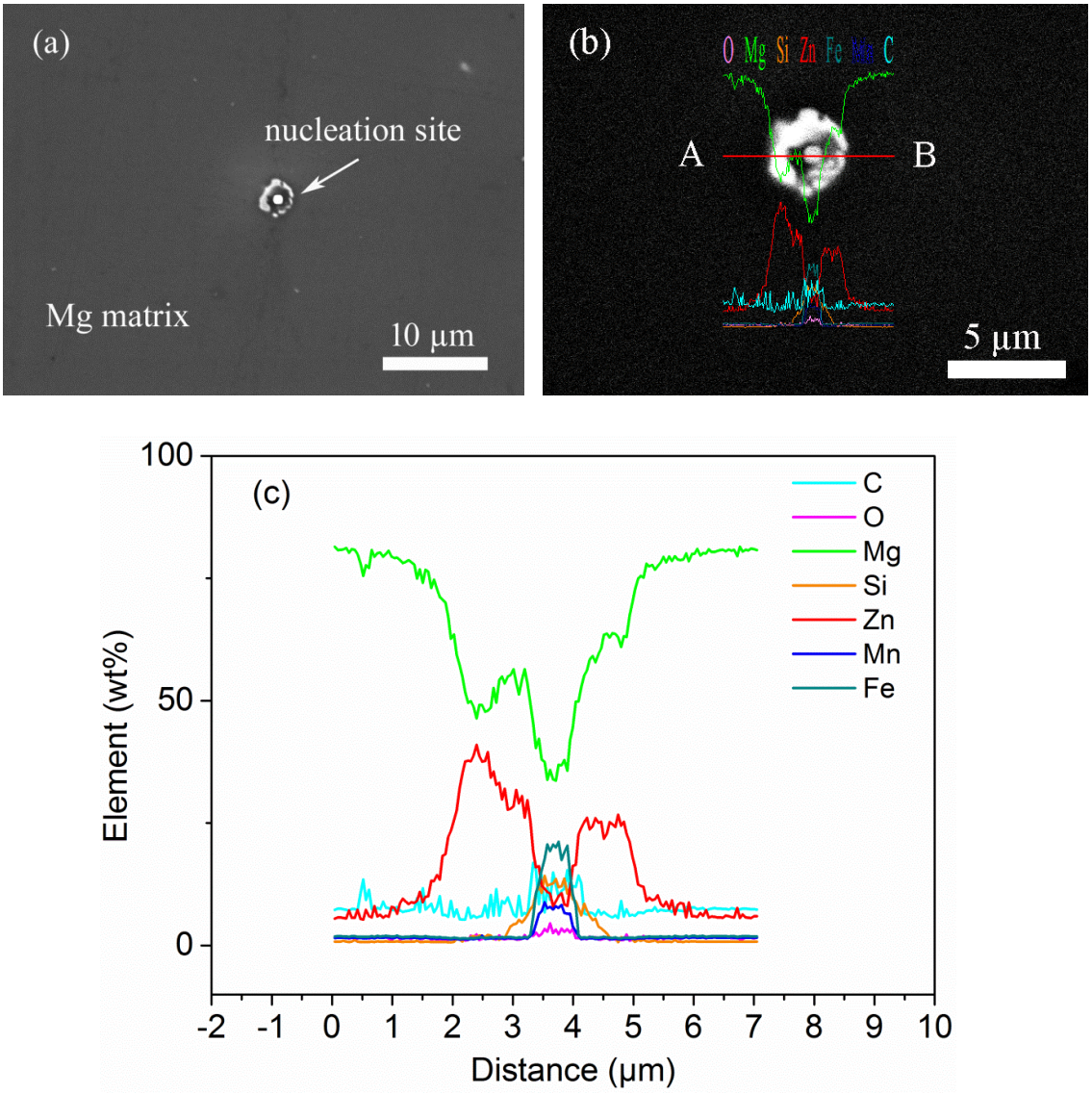

Fig. 5-18(a) BSE image of a nucleation site in Mg-3Zn-0.3SiC alloy; (b) EDS line-scan analysis of the nucleation site; (c) corresponding line-scan analysis curves along line A-B in Fig. 5-18(b) for clarity

Fig. 5-19(a) shows a feature of a nucleation site obtained in Mg-3Zn-0.5SiC alloy that detected by EDS line-scan analysis in Fig. 5-19(b). The grain boundaries were indicated clearly by the white arrows in Fig. 5-19(a). A few dotted Zn rich areas were observed along the grain boundaries. The nucleation site embedded in the Mg matrix locates inside the center of the Mg grain. The EDS line-scan results show that the combinations of elements in this region are similar to that of the nucleation site obtained in Mg-3Zn-0.3SiC alloy. The black part particle can be confirmed as a SiC particle, which is partly reacted with Mn and Fe impurities. In addition, Zn enriched area was also detected by EDS line-scan analysis at the

bottom of the right corner, which is closely attached to the SiC particle.

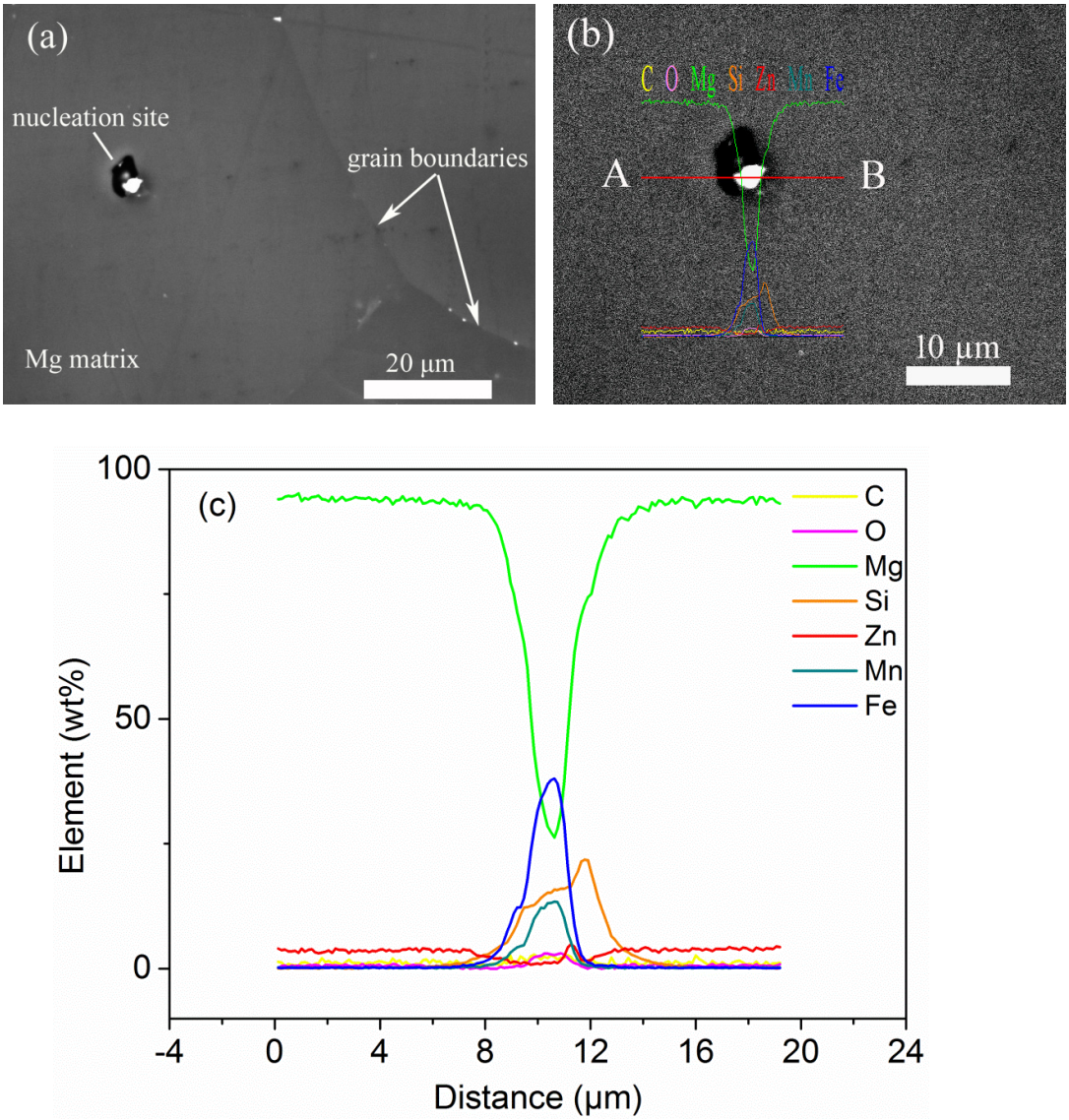

Fig. 5-19(a) BSE image of a nucleation site in Mg-3Zn-0.5SiC alloy; (b) EDS line-scan analysis of the nucleation site; (c) corresponding line-scan analysis curves along line A-B in Fig. 5-19(b) for clarity

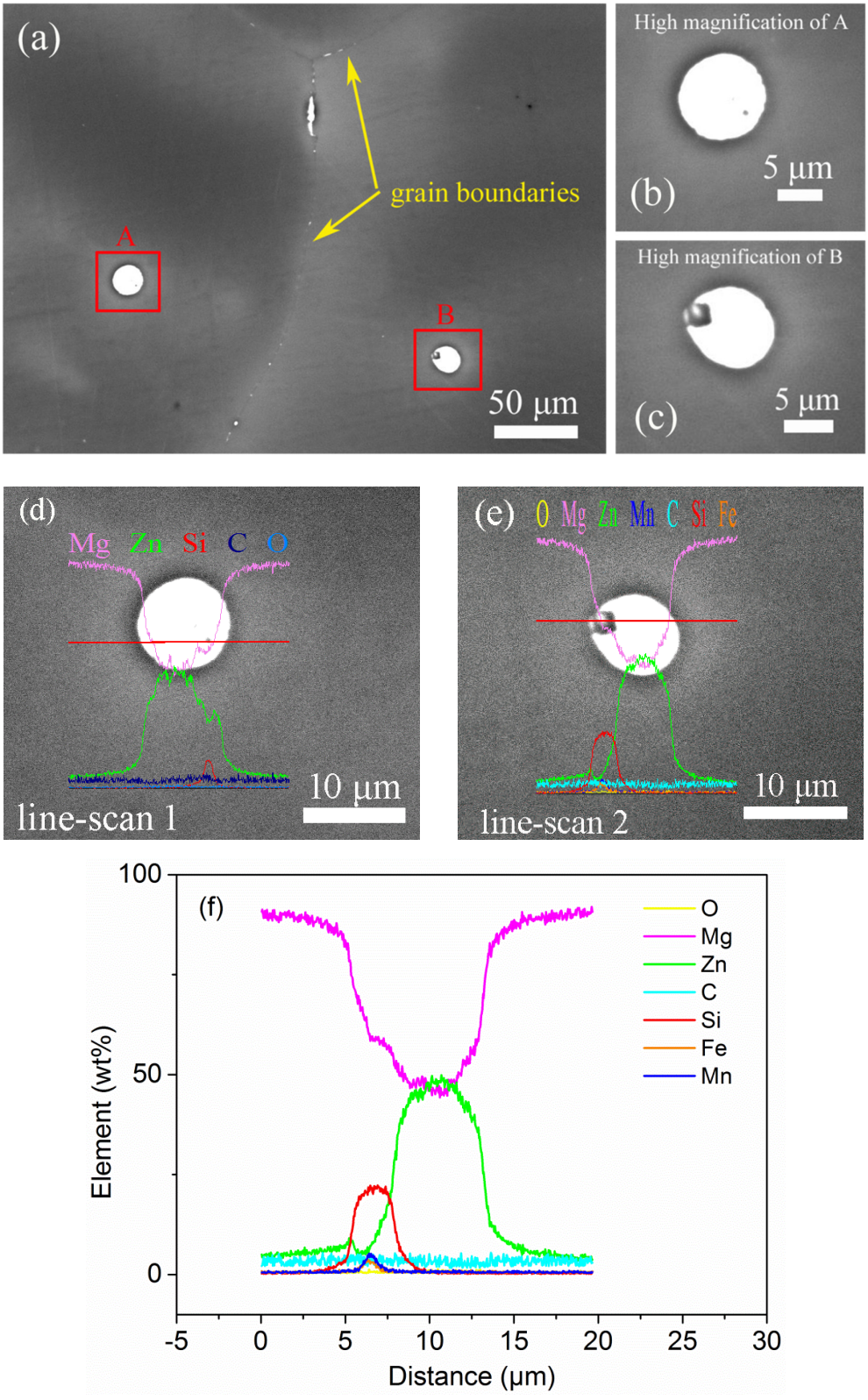

Fig. 5-20(a) BSE image of Mg-3Zn-10SiC alloy; (b) and (c) are high magnification images for point A and B marked with red rectangle in Fig. 5-20(a); (d) and (e) are corresponding EDS line-scan analyses; (f) line-scan analysis curve of line-scan 2 for clarity

Very similar results can be also detected in Mg-3Zn-10SiC alloy, and the detailed characterizations are shown in Fig. 5-20. Fig. 5-20(c), (e) and (f) clearly show that carbon containing SiC particle partly reacted with Mn and Fe to form Fe-Mn-Si rich intermetallic phase, which served as a nucleation site locates inside the center of the Mg grain. Another interesting result is that one small black region wrapped by the outside Zn enriched area was observed in Fig. 5-20(b). Corresponding EDS line-scan analysis in Fig. 5-20(d) shows that this region is enriched with Si and C, which can be confirmed as an unreacted SiC particle.

In order to verify the role of SiC with Mn and/or Fe in Mg-Zn system, comparative ingots prepared with high purity Mg were carried out under the same casting procedures. It should be noted that the content of Mn in commercial purity Mg is about 0.03%, which is 30 times of that in high purity Mg (0.001%), see in Table 5-1.

Table 5-1 Measured chemical composition of source materials (wt%)

Alloys	Zn	Al	Zr	Mn	Fe	Cu	Ca	Ni	Mg
Mg	0.003	0.006	<0.001	0.030	0.007	<0.001	0.0001	<0.0002	Bal.
HP Mg	0.003	0.004	<0.001	0.001	0.005	<0.001	<0.0001	<0.0002	Bal.
HP Zn	99.999	–	–	–	–	–	–	–	Bal.
Al	–	99.930	–	–	–	–	–	–	Bal.
Mg-2Mn	0.002	0.010	0.005	2.03	0.017	0.001	0.0006	0.002	Bal.
Mg-33Zr	–	–	31.083	–	–	–	–	–	Bal.

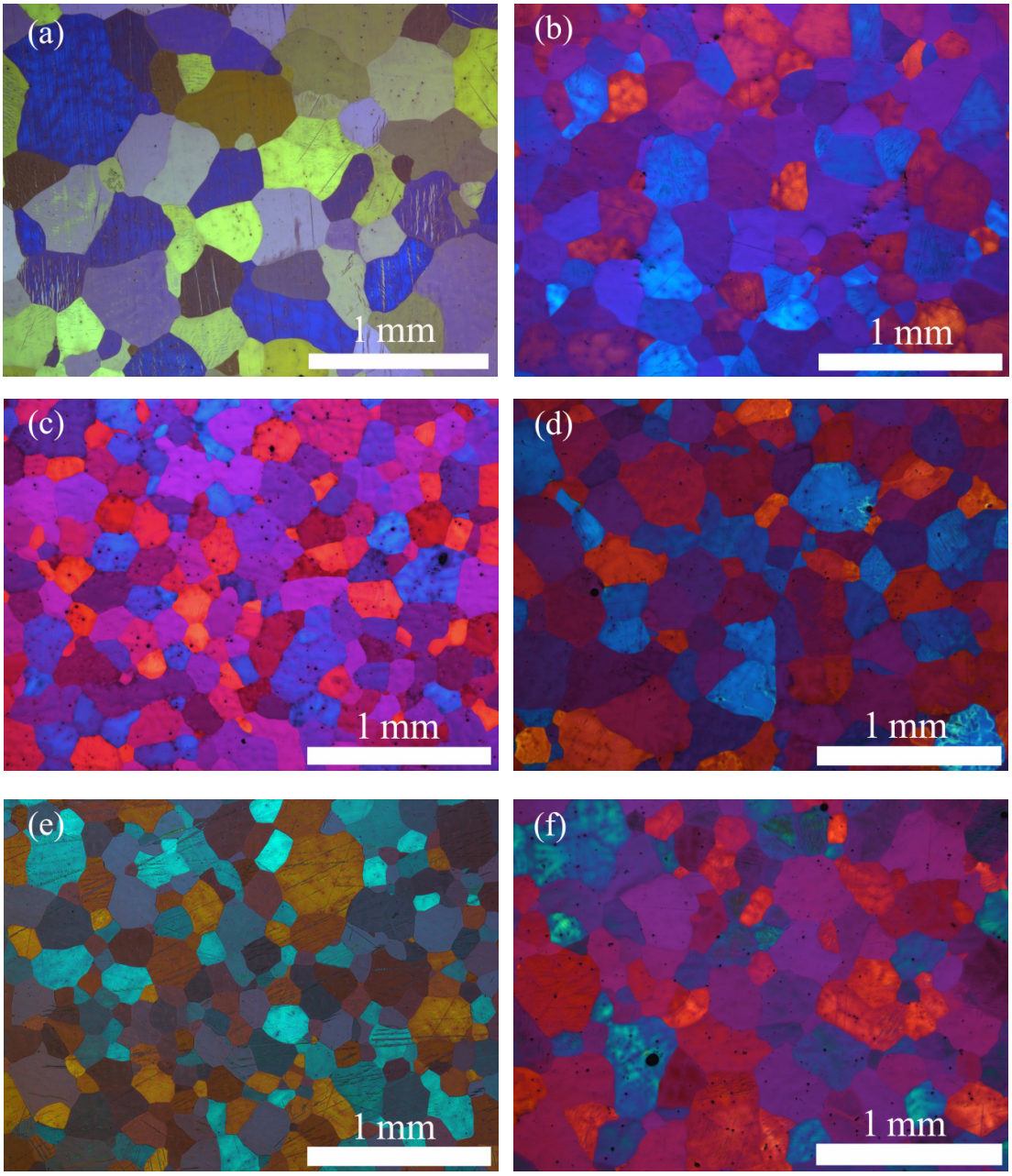

Fig. 5-21 Optical micrographs of as-cast alloys: (a) Mg-3Zn; (b) HP Mg-3Zn (c) Mg-3Zn-0.3SiC; (d) HP Mg-3Zn-0.3SiC; (e) Mg-3Zn-0.5SiC; (f) HP Mg-3Zn-0.5SiC

Fig. 5-21 shows the correspondingly optical micrographs of the comparison experiments. Compared with the remarkable grain refining effect of 0.3% SiC in commercial purity Mg-3Zn alloy, its grain refining effect in HP Mg-3Zn alloys can be neglected. The grain sizes of commercial purity Mg-3Zn alloy (Fig. 5-21(a)), HP Mg-3Zn alloy (Fig. 5-21(b)) and HP Mg-3Zn-0.3SiC alloy (Fig. 5-21(d)) keep in the same level. In addition, no such nucleation

sites can be observed in HP Mg-3Zn-0.3SiC alloy system by SEM characterization. Also, similar results occurred for 0.5% SiC inoculated in commercial purity Mg-3Zn or HP Mg-3Zn alloys, see in Fig. 5-21(e) and (f). Therefore, it is reasonable to conclude that Mn appeared in the commercial purity alloy is very important for the grain refining process with SiC inoculant in Mg-Zn alloy.

5.1.5 Effects of micro-alloying element Al

Fig. 5-22 shows the changes in average grain size of Mg-3Zn-0.3SiC alloys with different contents of Al addition. Interestingly, a sharp increase of average grain size from 253 ± 15 to 348 ± 30 μm was observed when the addition of Al is less than 0.1%. Then the average grain size decreases from 348 ± 30 to 250 ± 12 μm when the addition of Al increases from 0.1% to 0.3%. After that, the average grain size slightly decreases by adding more Al up to 1.0%. The average grain size of Mg-3Zn-0.3SiC-1.0Al alloys reaches to 238 ± 13 μm.

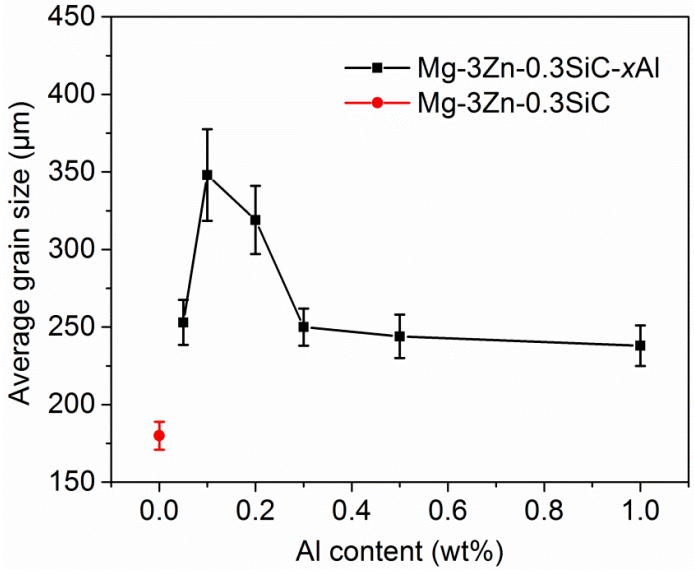

Fig. 5-22 Changes in average grain size of Mg-3Zn-0.3SiC alloys with different contents of Al addition. The average grain size of Mg-3Zn-0.3SiC alloy is given for comparison

Fig. 5-23 shows the corresponding optical micrographs of as-cast Mg-3Zn-0.3SiC-*x*Al alloys (x = 0.05, 0.1, 0.2, 0.3, 0.5, 1.0). Very big grains were observed in alloys with 0.1% and 0.2% Al addition (Fig. 5-23(b) and Fig. 5-23(c)). Relatively small and homogeneous grain morphologies were obtained with the addition of Al ≥ 0.3% in this alloy (Fig. 5-23(d) to (f)).

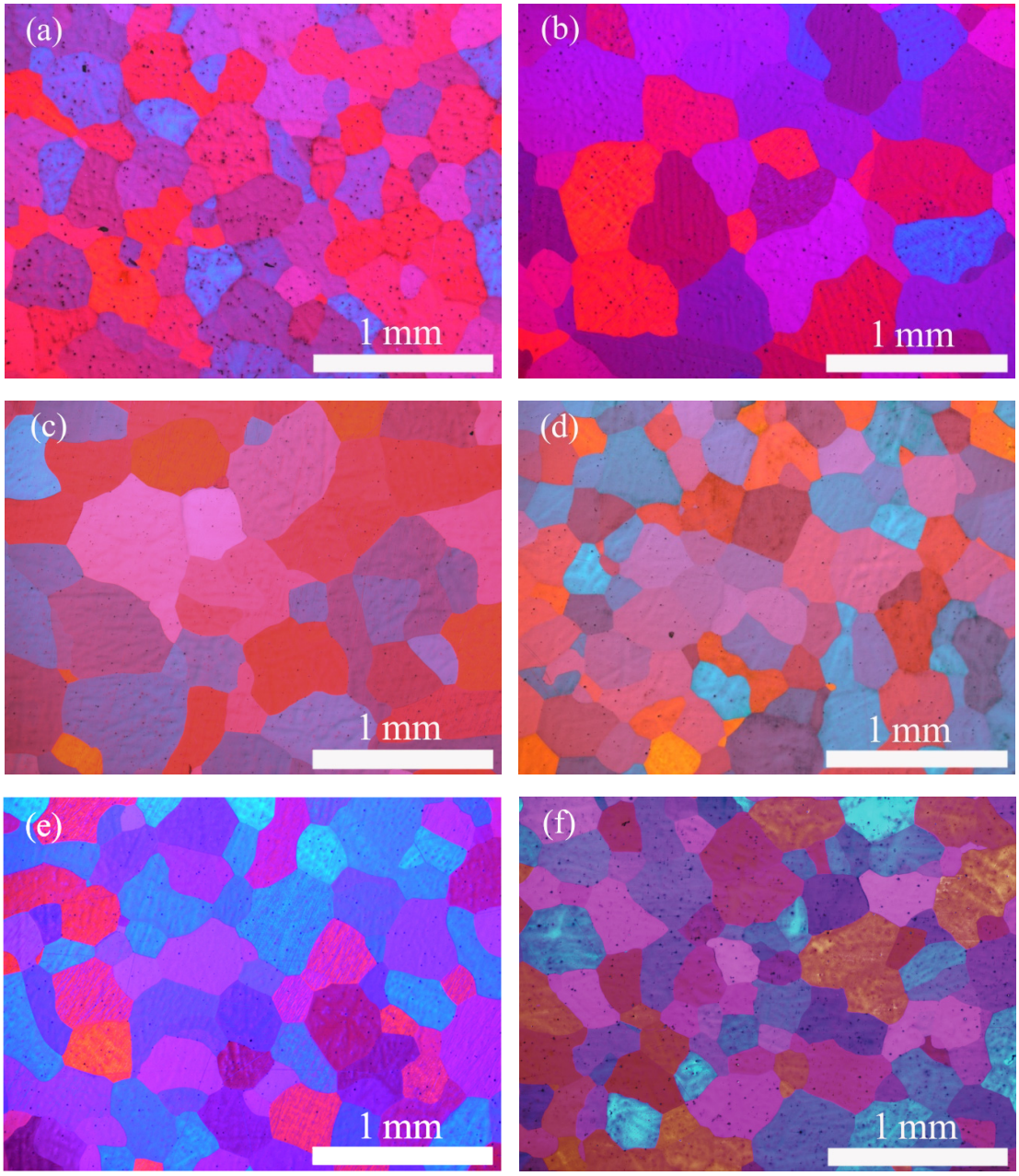

Fig. 5-23 Optical micrographs of as-cast Mg-3Zn-0.3SiC-xAl alloys: (a) x = 0.05%; (b) x = 0.1%; (c) x = 0.2%; (d) x = 0.3%; (e) x = 0.5%; (f) x = 1.0%

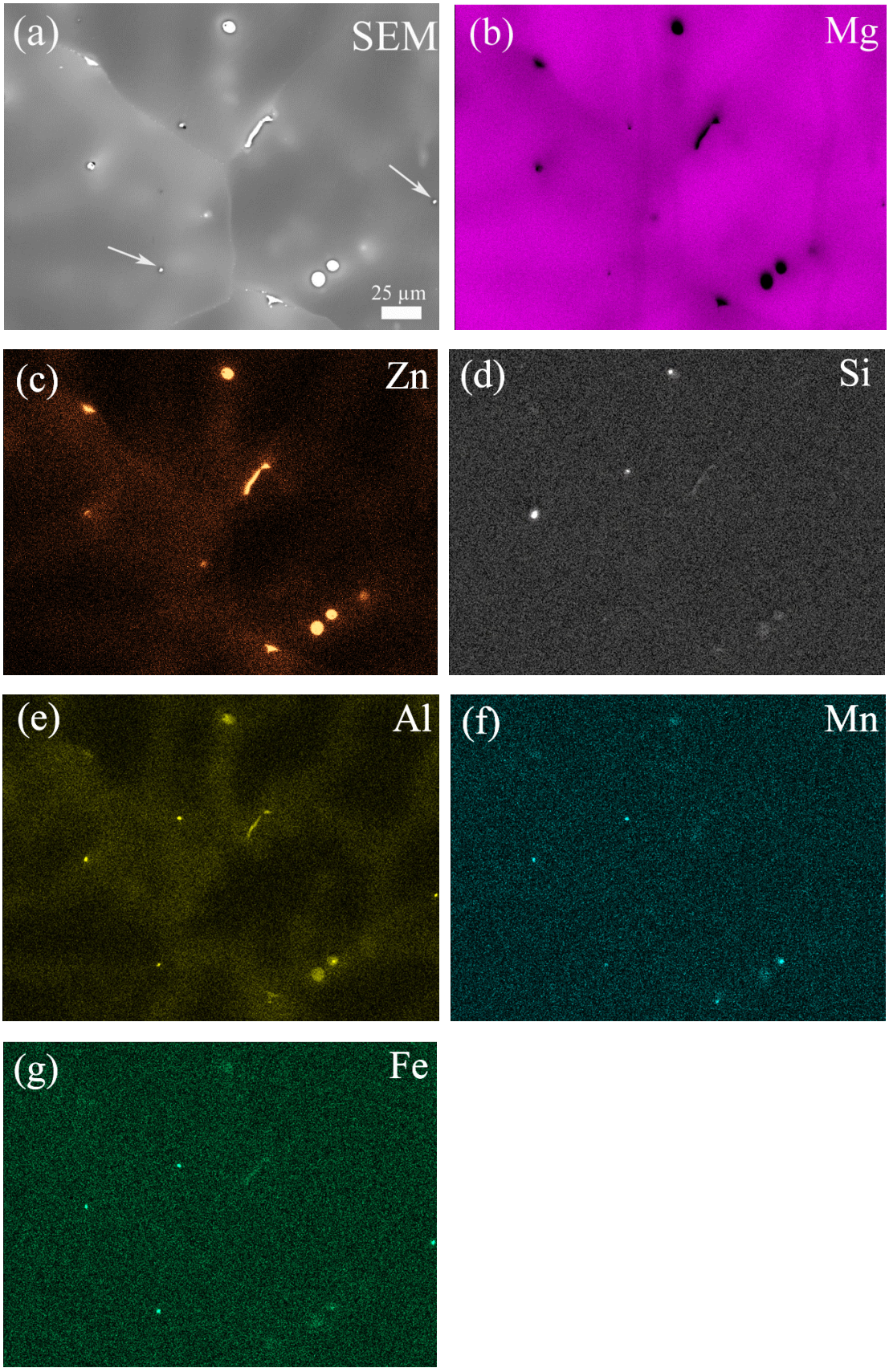

Fig. 5-24 BSE image and corresponding EDS mappings of Mg-3Zn-0.3SiC-1.0Al alloy

Fig. 5-24 shows a BSE image for as-cast Mg-3Zn-0.3SiC-1.0Al alloy and its corresponding EDS mapping analysis. Zn enriched areas were segregated along the grain boundaries. Especially, the Al element has the same distribution as that of element Zn, suggesting that the Al could affect the contact between SiC and Zn when some Al was added into the Mg-3Zn-0.3SiC system. In addition, wherever the distribution of Mn and/or Fe can be detected, the corresponding distribution of Al can be found. Two tiny particles with bright white contrast (marked by white arrows in Fig. 5-24(a)) were enriched with Al, Mn and Fe, which were identified as $Al_8(Mn,Fe)_5$ by further EDS analysis. This shows that Al has strong affinity with Mn and/or Fe. The addition of Al interfered with the grain refining effect of SiC in Mg-Zn system.

In order to clarify the influence of Mn and/or Fe on the grain refinement effect of Al in Mg-Zn-SiC alloy system, comparative ingot of HP Mg-3Zn-0.3SiC-0.1Al alloy was cast. Fig. 5-25 shows the corresponding optical micrographs. It clearly shows that the grain size of HP Mg-3Zn-0.3SiC-0.1Al alloy (Fig. 5-25(b)) is much smaller than that of commercial purity Mg-3Zn-0.3SiC-0.1Al alloy (Fig. 5-25(a)). In addition, the grain size of HP Mg-3Zn-0.3SiC alloy (Fig. 5-21(d)) is similar to that of HP Mg-3Zn-0.3SiC-0.1Al alloy. No poisoning grain refinement effect can be observed in HP Mg-3Zn-0.3SiC alloy with 0.1% Al addition. However, completely opposite results occurred in the commercial purity Mg-3Zn-0.3SiC alloy with small amount of Al addition.

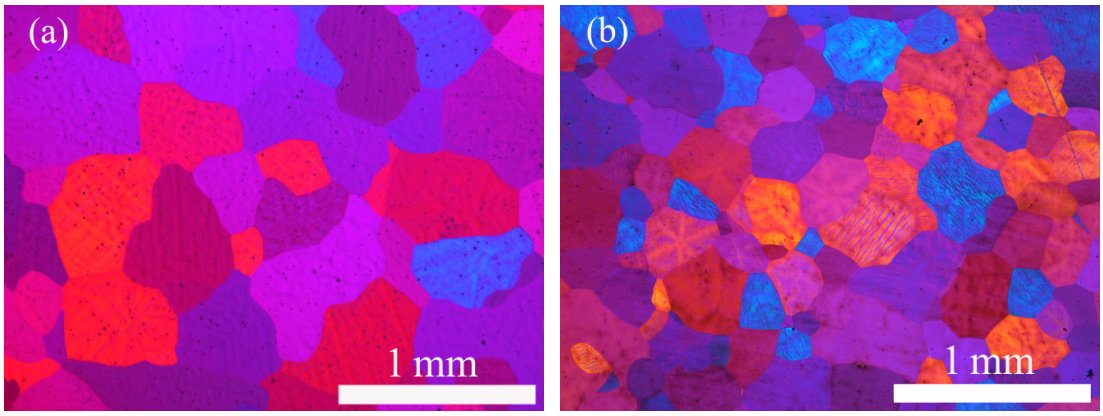

Fig. 5-25 Optical micrographs of as-cast alloy systems: (a) Mg-3Zn-0.3SiC-0.1Al; (b) HP Mg-3Zn-0.3SiC-0.1Al

5.1.6 Comparison experiments

5.1.6.1 Grain refinement of Mg-3Zn by graphite powder

SEM image of the graphite powder is shown in Fig. 5-26. Most of the graphite particles exhibit a diameter about 20 µm, but some broken particles with relatively small diameter can be also observed.

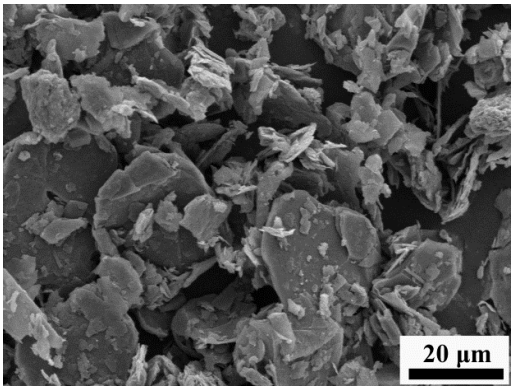

Fig. 5-26 SEM image of graphite powder with the diameter of < 20 µm

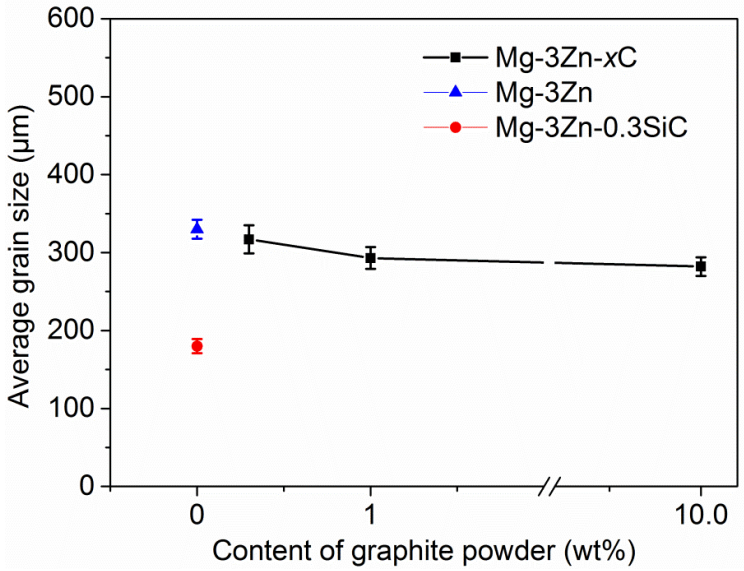

Fig. 5-27 Changes in average grain size of Mg-3Zn alloys with different contents of graphite addition. The average grain sizes of Mg-3Zn and Mg-3Zn-0.3SiC alloys are given for comparison

Fig. 5-27 shows the changes in average grain size of Mg-3Zn alloys with different contents of graphite (C) addition. It clearly shows that the average grain size decreases gradually but very slightly with the increasing amount of C addition. The average grain size changes from 317 ±

18 to 282 ± 12 μm when the addition of C increase from 0.3% to 10%. Comparing with the huge decrease tendency of average grain size from Mg-3Zn to Mg-3Zn-0.3SiC system, the average grain size decreases a bit when 0.3% C was added into Mg-3Zn system. This shows that the grain refining mechanisms for SiC and C could be totally different, and also the refining effect of SiC in Mg-Zn system is much better than that of C.

Fig. 5-28 shows the optical micrographs of as-cast Mg-3Zn, Mg-3Zn-0.3C, Mg-3Zn-1.0C and Mg-3Zn-10C alloys. The grain morphology of Mg-3Zn-0.3C alloy keeps almost the same as that of Mg-3Zn alloy. Relatively homogeneous and equiaxed grain size distribution were observed in Mg-3Zn-10C alloy. However, the grain size does not change significantly compared with that of Mg-3Zn alloy. In addition, no or very few C aggregation areas can be found in alloys inoculated with C addition.

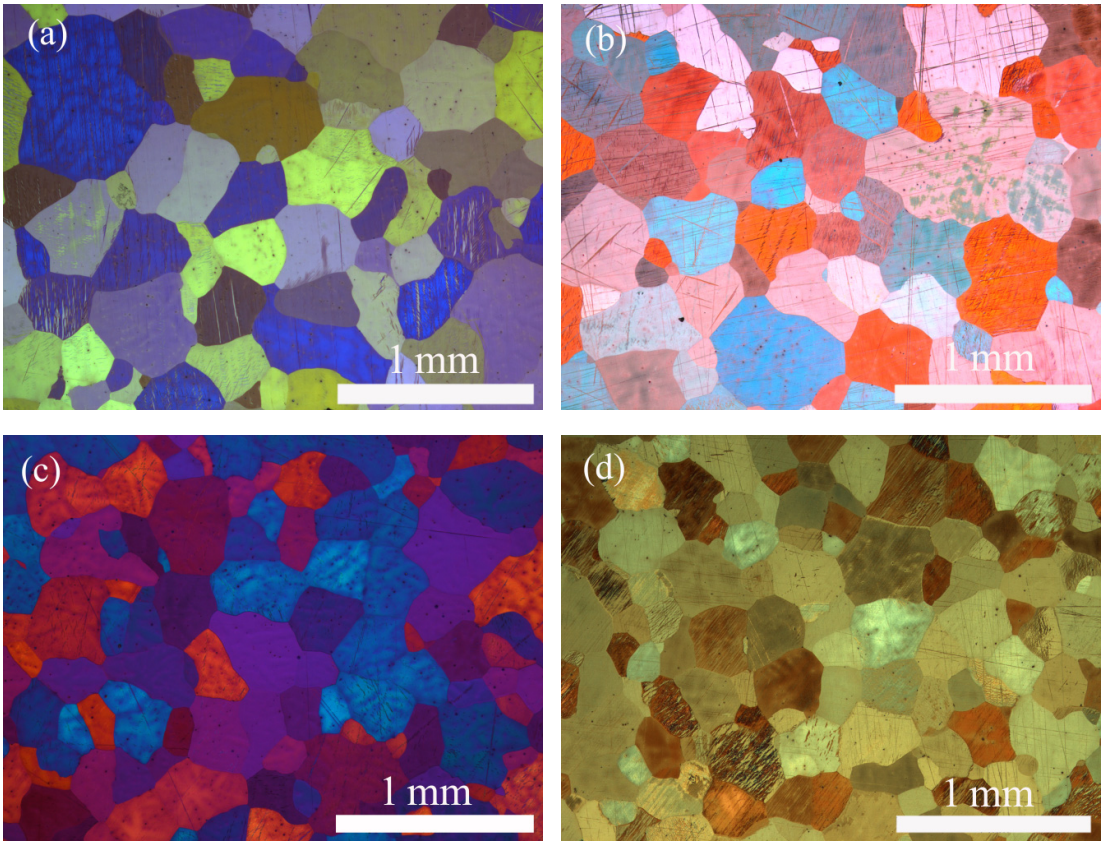

Fig. 5-28 Optical micrographs of as-cast alloys: (a) Mg-3Zn; (b) Mg-3Zn-0.3C; (c) Mg-3Zn-1.0C; (d) Mg-3Zn-10C

5.1.6.2 Grain refinement efficiency of Mg-3Zn-0.3SiC, Mg-3Al-0.3SiC and Mg-3Zn-0.3Zr alloy systems

Fig. 5-29 shows the variation of average grain size for Mg-3Zn-0.3SiC, Mg-3Al-0.3SiC and Mg-3Zn-0.3Zr alloy systems. Comparing the average grain size of Mg-3Zn-0.3SiC with that of Mg-3Al-0.3SiC, it seems that the grain refining efficiency of 3% Al is better than that of 3% Zn in Mg-0.3SiC system. The average grain sizes for Mg-3Zn-0.3SiC and Mg-3Al-0.3SiC alloy systems are 180 ± 9 and 158 ± 8 μm, respectively. When 0.3% Zr was used instead of 0.3% SiC in Mg-3Zn system, the average grain size reduces significantly from 180 ± 9 to 97 ± 2 μm.

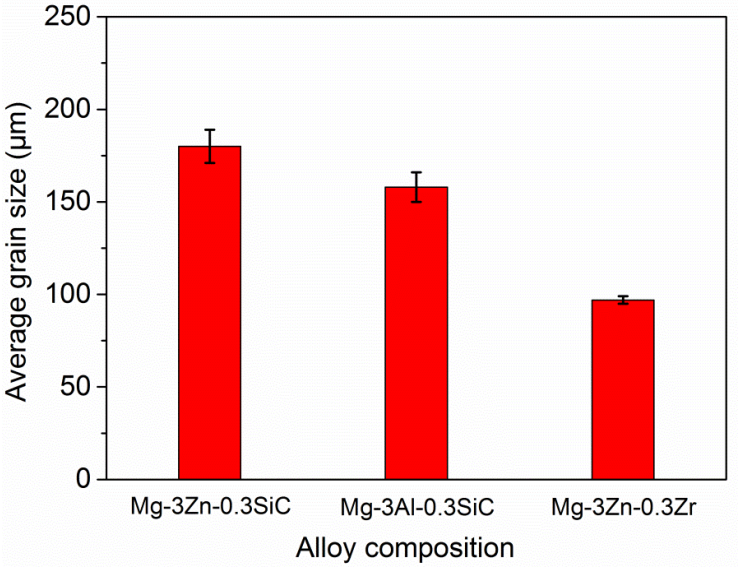

Fig. 5-29 Variation of average grain size for Mg-3Zn-0.3SiC, Mg-3Al-0.3SiC and Mg-3Zn-0.3Zr alloy systems

Fig. 5-30 shows the corresponding optical micrographs of as-cast Mg-3Zn-0.3SiC, Mg-3Al-0.3SiC and Mg-3Zn-0.3Zr alloy systems. Equiaxed grain size morphologies were observed in all the three alloy systems. The grain sizes keep in the same level for Mg-3Zn-0.3SiC and Mg-3Al-0.3SiC alloy systems. Very uniform grain sizes were observed in Mg-3Zn-0.3Zr alloy system as each grain in this alloy has almost the same size.

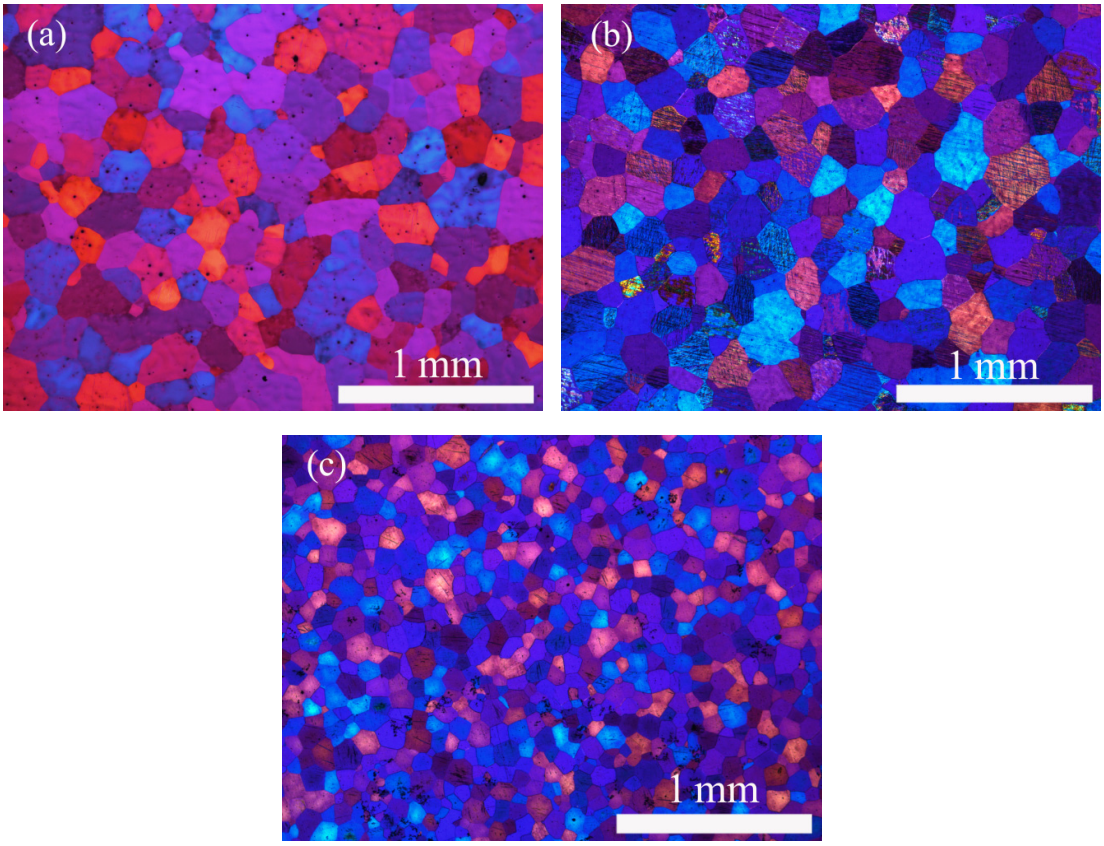

Fig. 5-30 Optical micrographs of as-cast alloys: (a) Mg-3Zn-0.3SiC; (b) Mg-3Al-0.3SiC; (c) Mg-3Zn-0.3Zr

5.2 Grain refinement of Mg-Mn-SiC alloys

5.2.1 Grain refinement of Mg-*x*Mn alloys

The criteria of selection and investigation for Mg-Mn-SiC alloy system are the same as Mg-Zn-SiC alloy system. They will not be emphasized hereafter. Fig. 5-31 shows the microstructures and variations in average grain size of as-cast pure Mg alloy with different contents of Mn, i.e. Mg-*x*Mn (x = 0.1, 0.2, 0.3, 0.5, 1) alloys. A large amount of columnar grains were observed in Fig. 5-31(a) when only 0.1% Mn was added into pure Mg. After 0.2% Mn was added into pure Mg, the grain size decreased as parts of the columnar grains were changed into equiaxed grains. The columnar grains still existed even when 1% Mn was added into pure Mg. Compared with the grain refinement effect of Zn on pure Mg, the reduction of average grain size caused by Mn addition became less. The average grain size reaches to about 638 ± 24 μm for Mg-1Mn alloys (Fig. 5-31(f)).

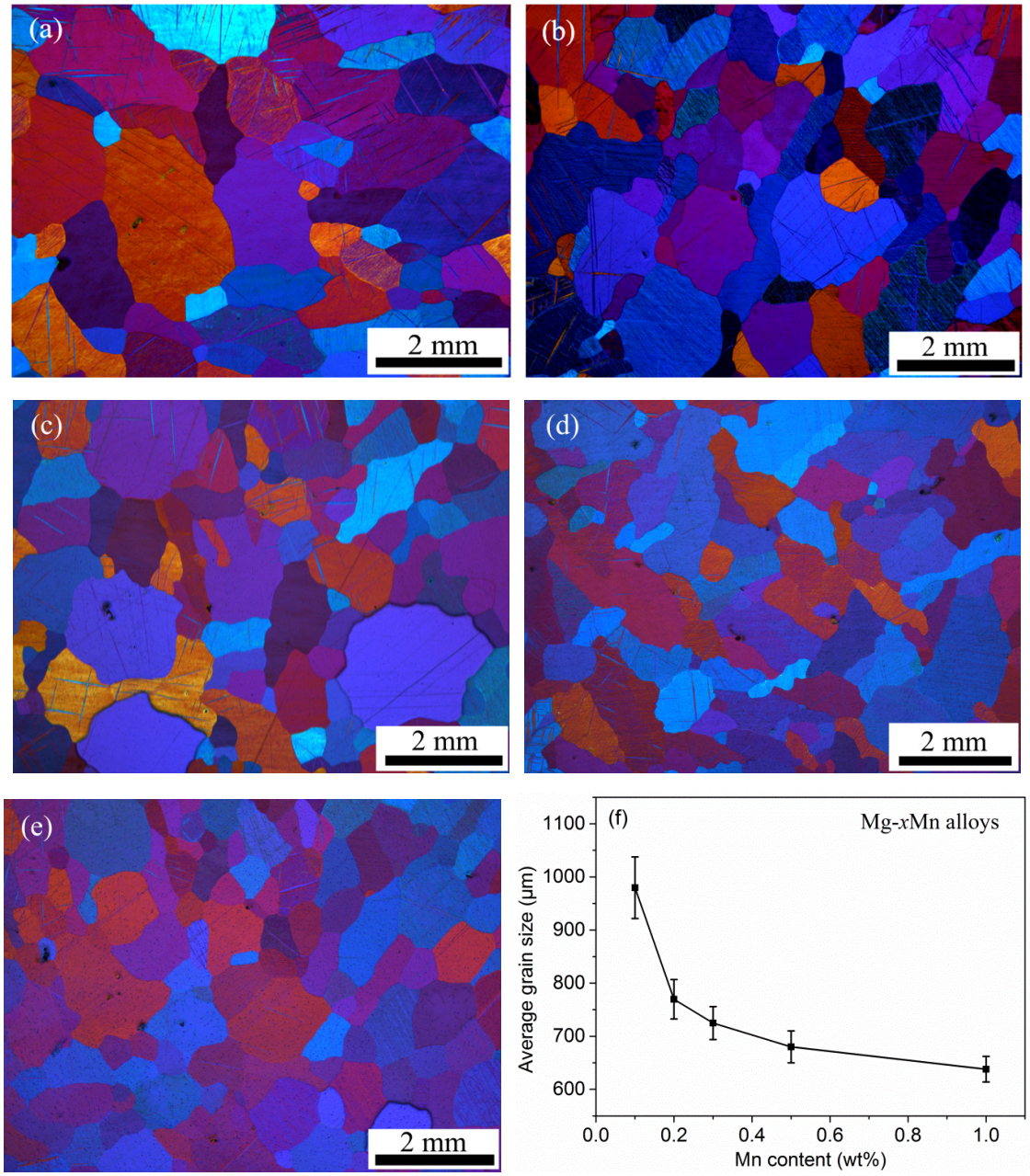

Fig. 5-31 Optical micrographs of as-cast alloys: (a) Mg-0.1Mn; (b) Mg-0.2Mn; (c) Mg-0.3Mn; (d) Mg-0.5Mn; (e) Mg-1Mn; (f) Changes in average grain size of pure Mg with different contents of Mn

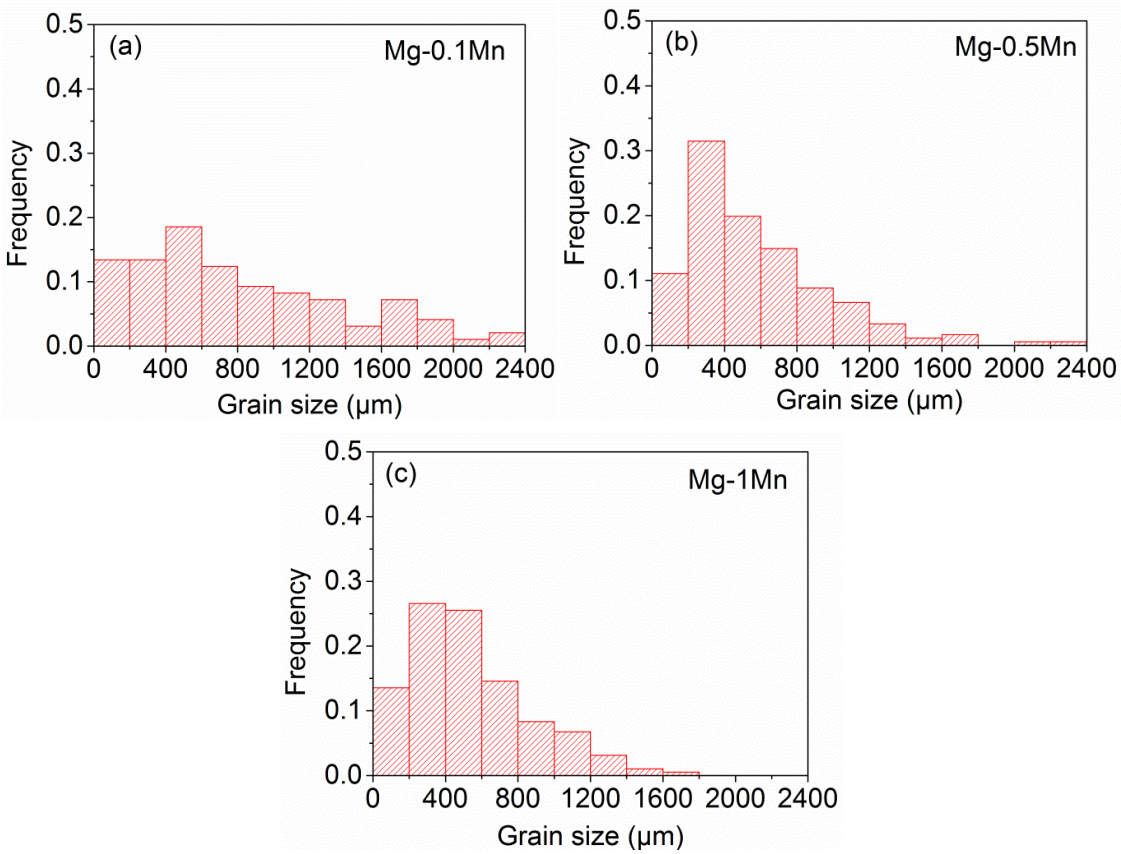

Fig. 5-32 Grain size distribution of alloys: (a) Mg-0.1Mn; (b) Mg-0.5Mn; (c) Mg-1Mn

Fig. 5-32 shows the grain size distribution of Mg-*x*Mn (*x* = 0.1, 0.5, 1) alloys. The frequencies of grain size distribution in both Mg-0.1Mn and Mg-0.5Mn were scattered in the size range from 0 to 2400 μm (the results of grain size distributions of Mg-0.2Mn and Mg-0.3Mn alloys are similar, not shown). For Mg-0.1Mn alloy, the frequency in each range section of 200 μm did not change significantly especially within the size distribution ≤ 1200 μm (Fig. 5-31(a)). In contrast, narrow distribution of grain size for Mg-1Mn alloy was obtained in Fig. 5-32(c). However, the frequency column of grain size distribution for Mg-1Mn in the size range ≥ 1000 μm still appeared. This is related to that the columnar grains were not totally suppressed by adding 1% Mn into pure Mg.

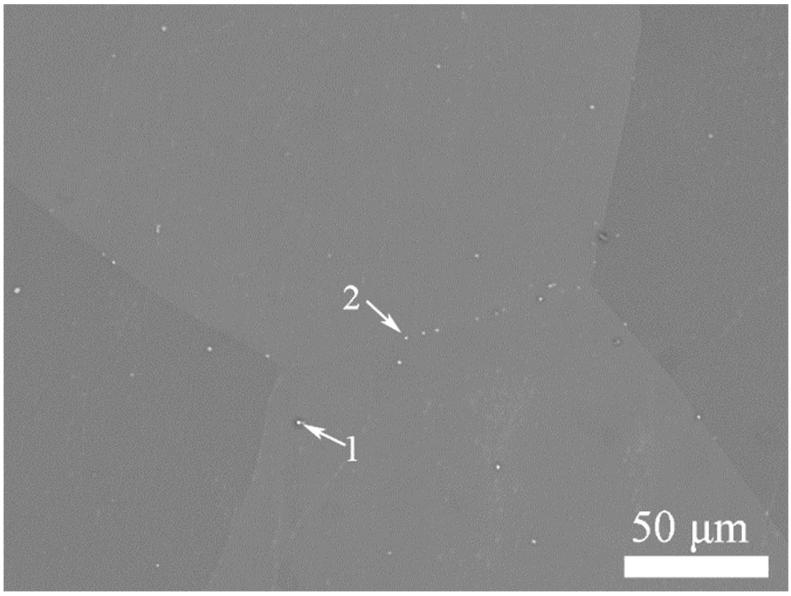

Fig. 5-33 BSE image of the as-cast Mg–0.1Mn alloy

Table 5-2 Quantitative EDS results of the areas as indicated in Fig. 5-33

Area	Composition (at%)		
	Mg	Mn	O
1	91.3	1.6	7.1
2	97.7	0.6	1.7

Fig. 5-33 shows a BSE image of the as-cast Mg-0.1Mn alloy. The corresponding quantitative EDS results are given in Table 5-2. The discontinuous α-Mn particles with white contrast were observed mostly along the grain boundaries. Very few α-Mn can be found inside α-Mg grains. Similar morphologies and EDS results were also reported by Zhong et al. [135]. Different from the distribution of Zn in binary Mg-Zn alloy, segregation of Mn was not found.

5.2.2 Grain refinement of Mg-*x*Mn-0.3SiC alloys

Fig. 5-34 shows the microstructures and variations in average grain size of as-cast Mg-*x*Mn (*x* = 0.1, 0.2, 0.3, 0.5, 1.0) alloys with the same addition of 0.3% SiC. The average grain size of the Mg-*x*Mn-0.3SiC alloys decreased gradually with the increase of Mn content. It decreased from 930 ± 38 µm for Mg-0.1Mn-0.3SiC alloy to 602 ± 21 µm for Mg-1.0Mn-0.3SiC alloy as shown in Fig. 5-34(f). Relatively uniform grain size distributions were obtained with the addition of 0.3% SiC into Mg-1Mn alloy. It should be noted that the amount of SiC clusters

indicated by white arrows increased with the increase of Mn content. In particular, the SiC clusters could be readily found in the alloy with Mn content ≥ 0.3%. In addition, parts of the SiC clusters locate inside Mg grains, while others locate between grain boundaries. Therefore, Mn addition could affect the settling behavior of SiC, and/or the affinity between Mn and SiC which has close relationship to affect the grain refining process.

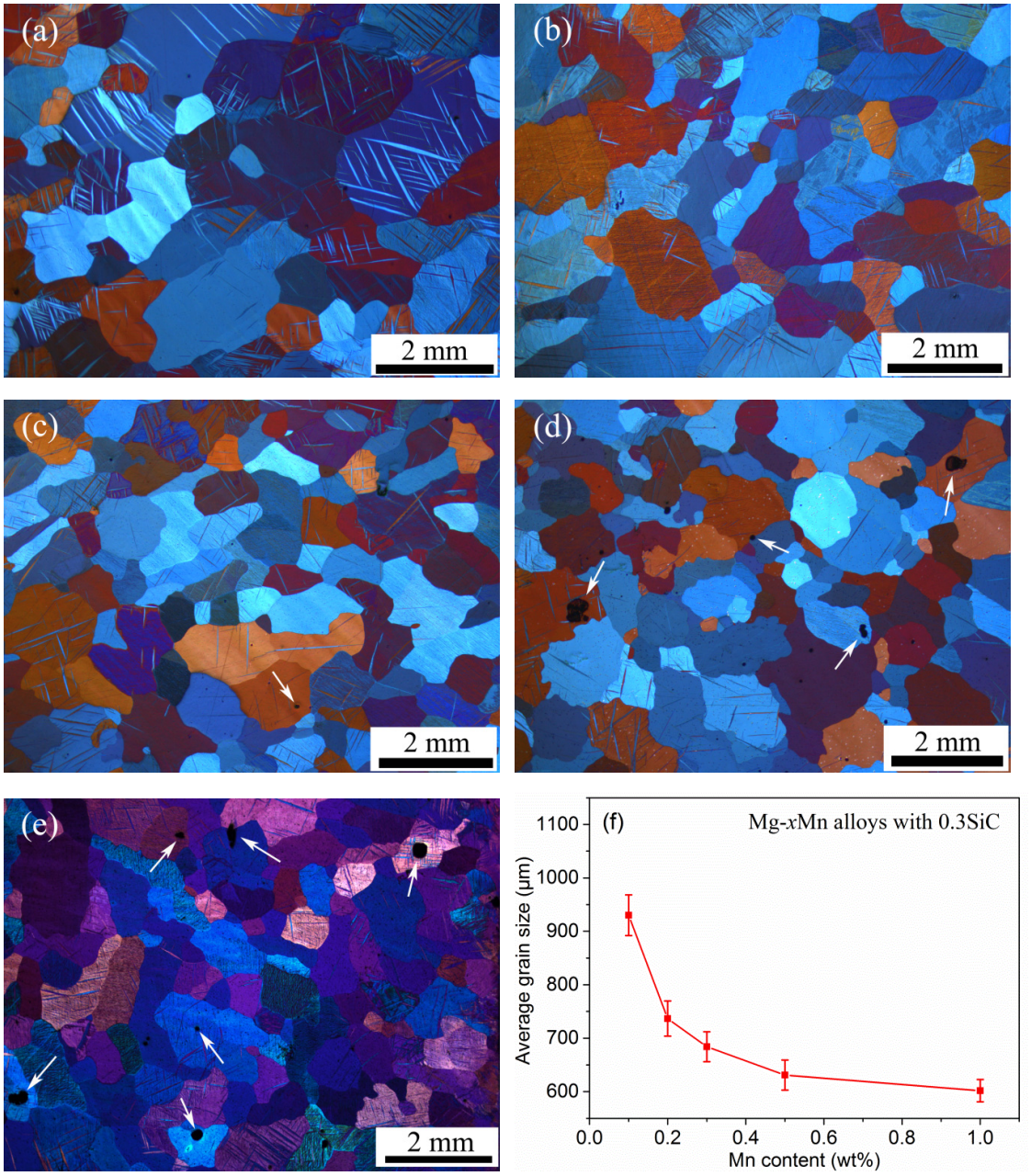

Fig. 5-34 Optical micrographs of as-cast alloys: (a) Mg-0.1Mn-0.3SiC; (b) Mg-0.2Mn-0.3SiC; (c) Mg-0.3Mn-0.3SiC; (d) Mg-0.5Mn-0.3SiC; (e) Mg-1.0Mn-0.3SiC; (f) Changes in average grain size of binary Mg-xMn alloys with 0.3% SiC. The white arrows indicate SiC clusters

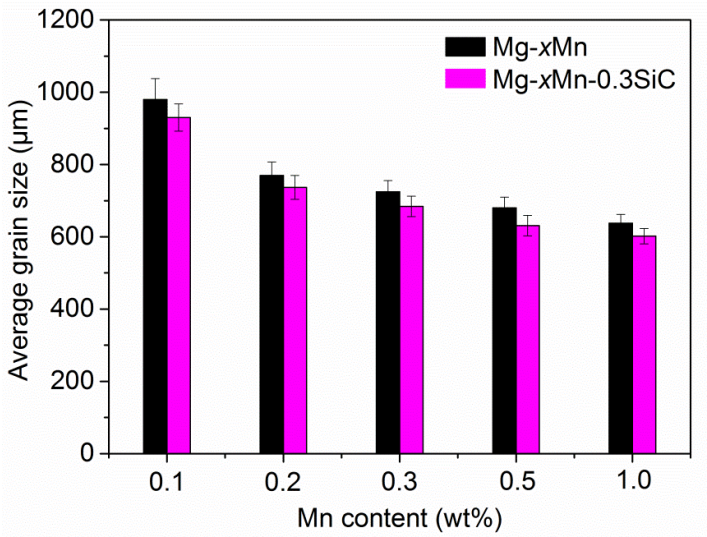

Fig. 5-35 Average grain size comparison of binary Mg-xMn alloys with and without 0.3SiC addition

Fig. 5-35 shows the average grain size comparison diagram of as-cast Mg-*x*Mn (*x* = 0.1, 0.2, 0.3, 0.5, 1.0) alloys prior to and after the addition of 0.3% SiC. It clearly shows that the average grain size of Mg-*x*Mn alloys decreased with addition of 0.3% SiC in all the range of Mn content. Compared to the results of Mg-*x*Zn alloys prior to and after the addition of 0.3% SiC in Fig. 5-6, the average grain size reduction of Mg-*x*Mn alloys prior to and after the addition of 0.3% SiC keeps in a similar level at different contents of Mn.

Fig. 5-36(a) shows an optical micrograph of as-cast Mg-0.3Mn-0.3SiC alloy at high magnification. The region marked as red rectangle in Fig. 5-36(a) was characterized by SEM and the correspondingly quantitative EDS analyses of the areas are given in Table 5-3. In Fig. 5-36(b), SiC cluster was confirmed in area 2 and 6, because both Si and C were detected but no Mn was contained. The Si/C atomic ratio in area 6 is 1.05, which is very close to that of SiC. Compared with the area 2 by collecting data from a single point, the Si/C atomic ratio in area 6 is more accurate as the detected area was collected from a rectangle. Elements of Si, Mn and C were detected in areas 1, 4 and 5, and the corresponding elements of Mg and O in those areas are coming from the matrix, which is supported by the EDS analysis in area 3. These particles with bright contrast are possibly Mn-Si-(C) containing phases from the reaction between Mn and SiC.

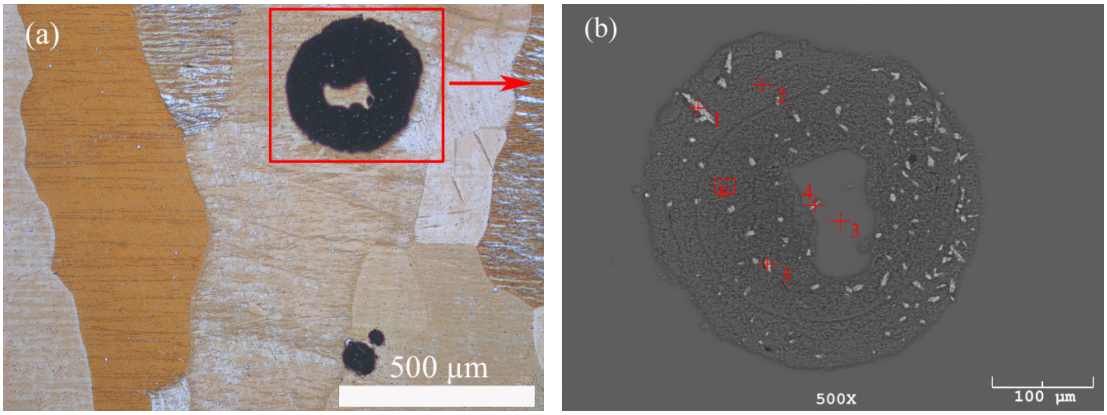

Fig. 5-36 (a) Optical micrograph of as-cast Mg-0.3Mn-0.3SiC alloy at high magnification; (b) BSE image of the area indicated by red rectangle in (a)

Table 5-3 Quantitative EDS results of the areas as indicated in Fig. 5-36(b)

Area	Composition (at%)				
	Mg	Mn	Si	C	O
1	12.0	24.2	20.5	28.2	15.1
2	25.5	–	20.3	47.4	6.9
3	98.6	–	–	–	1.4
4	37.8	25.3	2.7	10.0	24.1
5	17.3	51.4	2.8	7.5	21.0
6	25.7	–	34.6	33.0	6.6

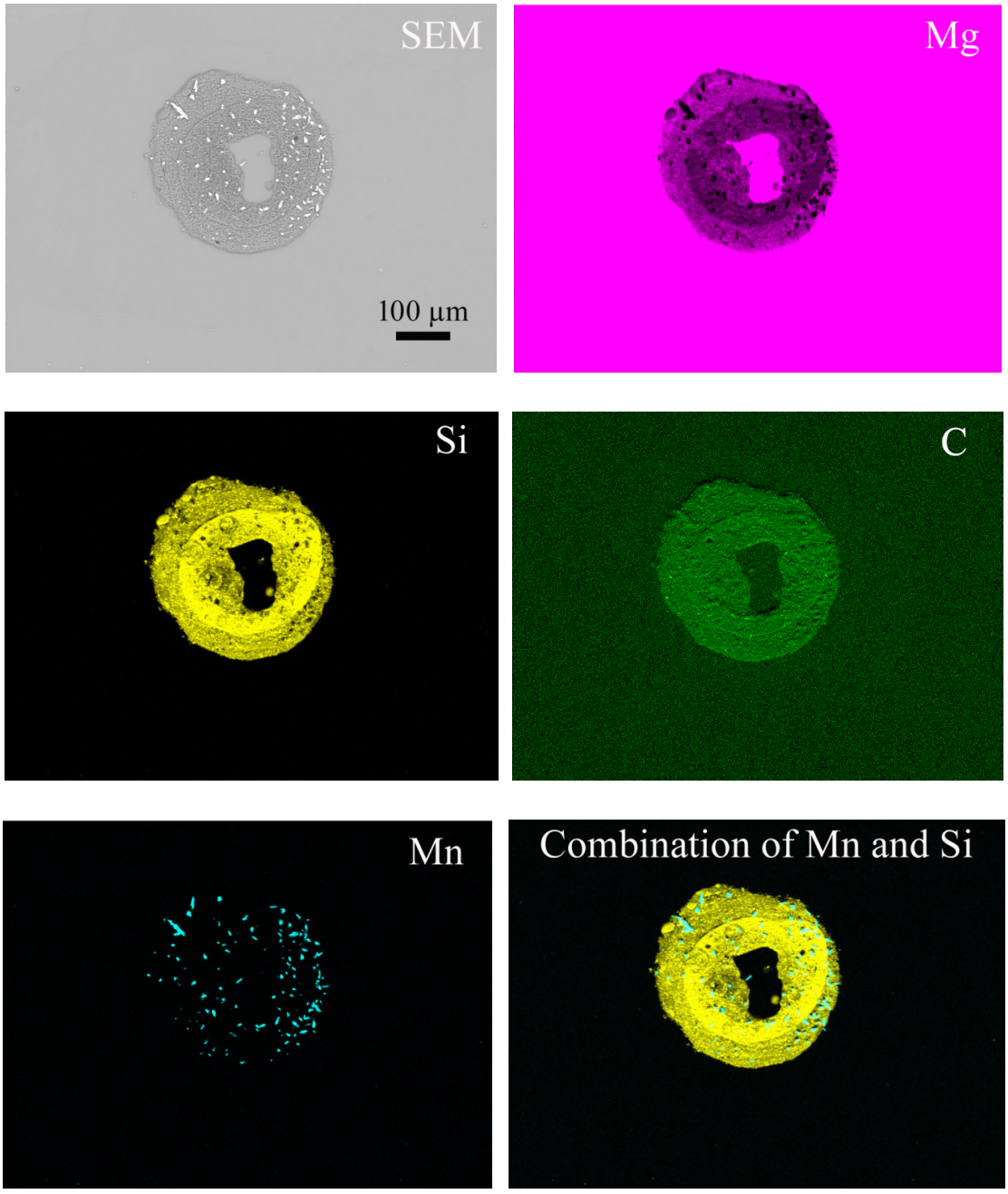

Fig. 5-37 EDS mapping analysis of a typical SiC cluster in Mg-0.3Mn-0.3SiC alloy

Fig. 5-37 shows the EDS mapping analysis of the typical SiC cluster in Mg-0.3Mn-0.3SiC alloy. The elements of Si and C have the same distribution verifying that SiC cluster was further confirmed. It clearly shows that Mn and SiC have very close contact in the picture of the combination of Mn and Si. This kind of contact relationship did not occur occasionally, because the distribution of Mn is discontinuous and most of the Mn selectively locates both the outer and inner edges of SiC particles. Therefore, SiC prefers to capture the Mn and then

partially reacts with Mn to form new Mn-Si phase, which in turn affects the inoculation process of SiC.

5.2.3 Effects of grain-refining parameters on Mg-1Mn-SiC alloys

5.2.3.1 Addition amount

Fig. 5-38 shows the changes in average grain size of Mg-1Mn alloy inoculated by different SiC contents. It shows a linear decrease of average grain size from 625 ± 22 to 560 ± 18 μm with the increase of SiC content from 0.1% to 0.5% in Mg-1Mn alloys. Then, the average grain size keeps stable for the SiC content between 0.5% and 1.0%. After that, the average grain size increases slightly with the addition of 5.0% SiC. The average grain size of Mg-1Mn-5.0SiC reaches to 572 ± 20 μm.

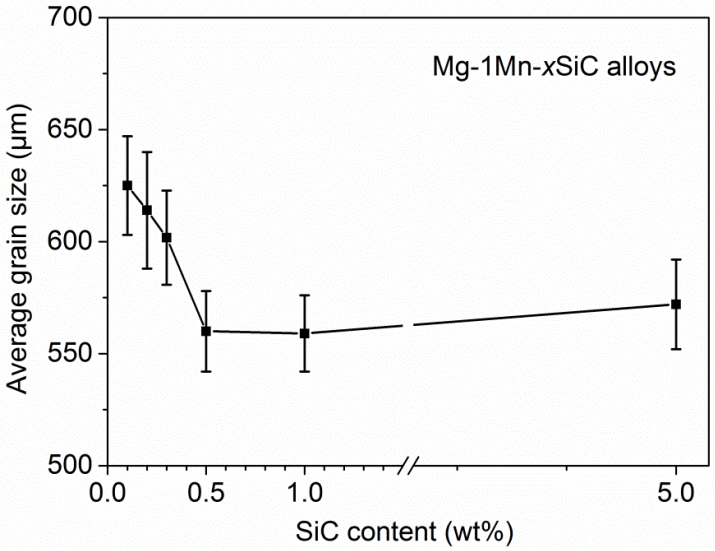

Fig. 5-38 Changes in average grain size of Mg-1Mn alloy inoculated by different SiC contents

Fig. 5-39 shows the optical micrographs of as-cast Mg-1Mn-*x*SiC (*x* = 0.1, 0.2, 0.3, 0.5, 1.0, 5.0) alloys. The volume fraction of columnar grains was suppressed gradually by adding more SiC particles, up to 1.0%. Relatively uniform grain size morphologies were obtained with the addition of 0.5% ~ 1.0% SiC into Mg-1Mn alloy. It clearly shows that SiC clusters indicated by white arrows can be detected when the contents of SiC are higher than 0.2%. Especially, large amount of SiC clusters could be found in Mg-1Mn alloy with 5.0% SiC addition. The aggregation of SiC in Mg-1Mn-5.0SiC is more severe than that in Mg-3Zn-10SiC (Fig. 5-8(c)).

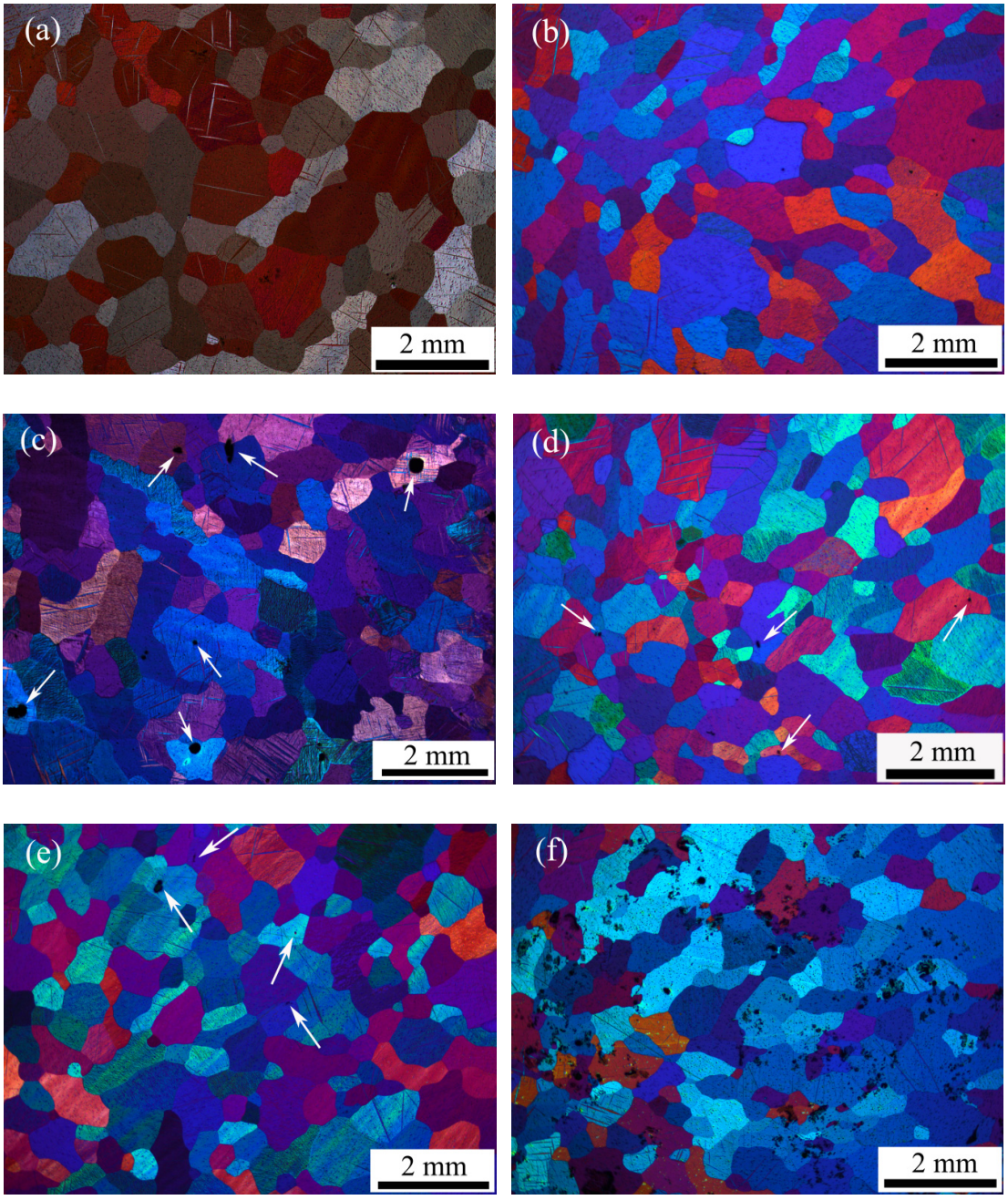

Fig. 5-39 Optical micrographs of as-cast alloys: (a) Mg-1Mn-0.1SiC; (b) Mg-1Mn-0.2SiC; (c) Mg-1Mn-0.3SiC; (d) Mg-1Mn-0.5SiC; (e) Mg-1Mn-1.0SiC; (f) Mg-1Mn-5.0SiC

Fig. 5-40 shows the XRD patterns of as-cast Mg-1Mn-1.0SiC and Mg-1Mn-5.0SiC alloys. Only Mg peaks can be detected in Mg-1Mn-1.0SiC alloys. Lack of SiC phase evidence is attributed to the less detectable volume fraction of SiC in Mg-1Mn-1.0SiC alloy. Instead, a peak at 2θ = 43.3° appears in Mg-1Mn-5.0SiC alloy, which is matching the SiC phase that appears in SiC powder pattern (PDF pattern No. 01-073-1664).

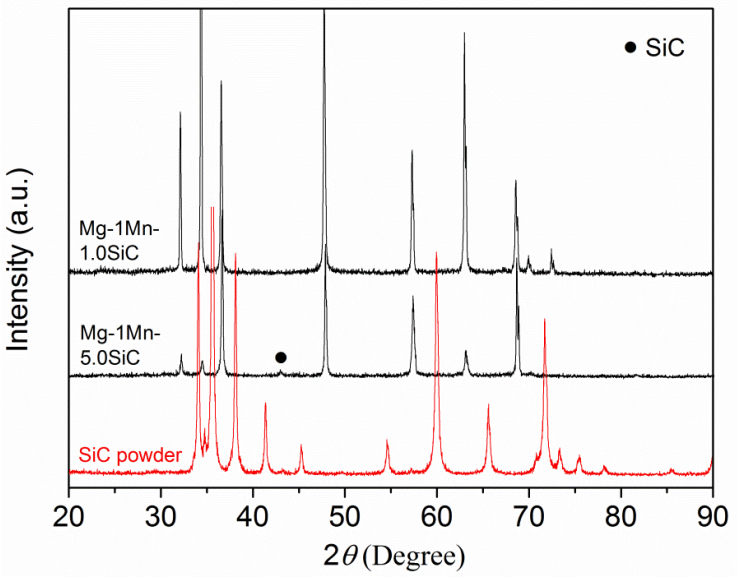

Fig. 5-40 XRD patterns of Mg-1Mn-1.0SiC and Mg-1Mn-5.0SiC alloys. Pattern of SiC powder was used in comparison. The peaks corresponding to Mg are not labeled

5.2.3.2 Effect of SiC particle size

Fig. 5-41 shows the average grain size of Mg-1Mn alloy by adding 0.5% SiC with different particle size.

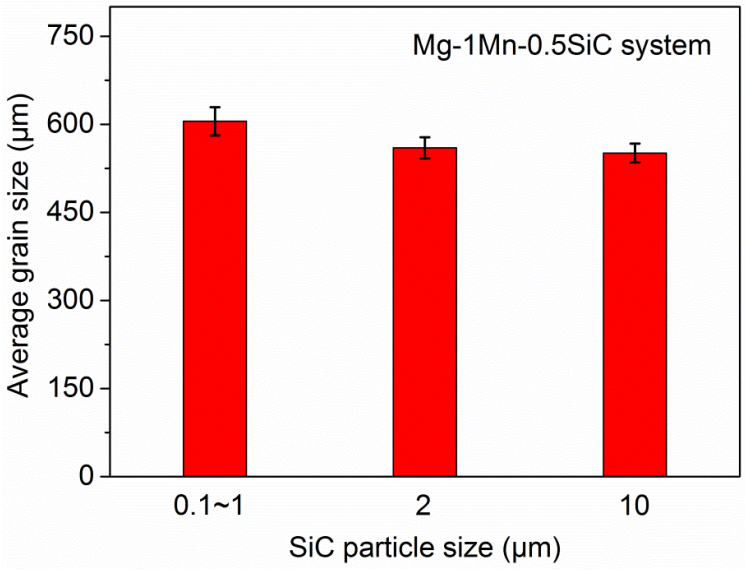

Fig. 5-41 Variation of average grain size with different SiC particle size for Mg-1Mn-0.5SiC alloy system

Compared with the alloys inoculated by SiC particles in the form of 2 μm and 10 μm, the alloy inoculated by 0.1~1 μm SiC has biggest average grain size. The average grain size of

Mg-1Mn-0.5SiC (0.1~1 µm) reaches to 605 ± 24 µm. The grain refining effects are equivalent by adding SiC particles in the form of 2 µm and 10 µm. The average grain size reaches to 560 ± 18 µm and 551 ± 16 µm for Mg-1Mn-0.5SiC (2 µm) and Mg-1Mn-0.5SiC (10 µm) alloy, respectively.

The corresponding optical micrographs of Mg-1Mn alloy by adding 0.5% SiC with different particle sizes are shown in Fig. 5-42. Large amount of SiC clusters and discontinuous SiC particles can be observed in Mg-1Mn-0.5SiC (0.1~1 µm) alloy (Fig. 5-42(a)). Some of them locate inside Mg grains but others are pushed at the grain boundaries. The grain morphologies and the grain size distributions in Mg-1Mn-0.5SiC (2 µm) and Mg-1Mn-0.5SiC (10 µm) alloys are similar. Very few SiC clusters can be detected in Mg-1Mn-0.5SiC (10 µm) alloys.

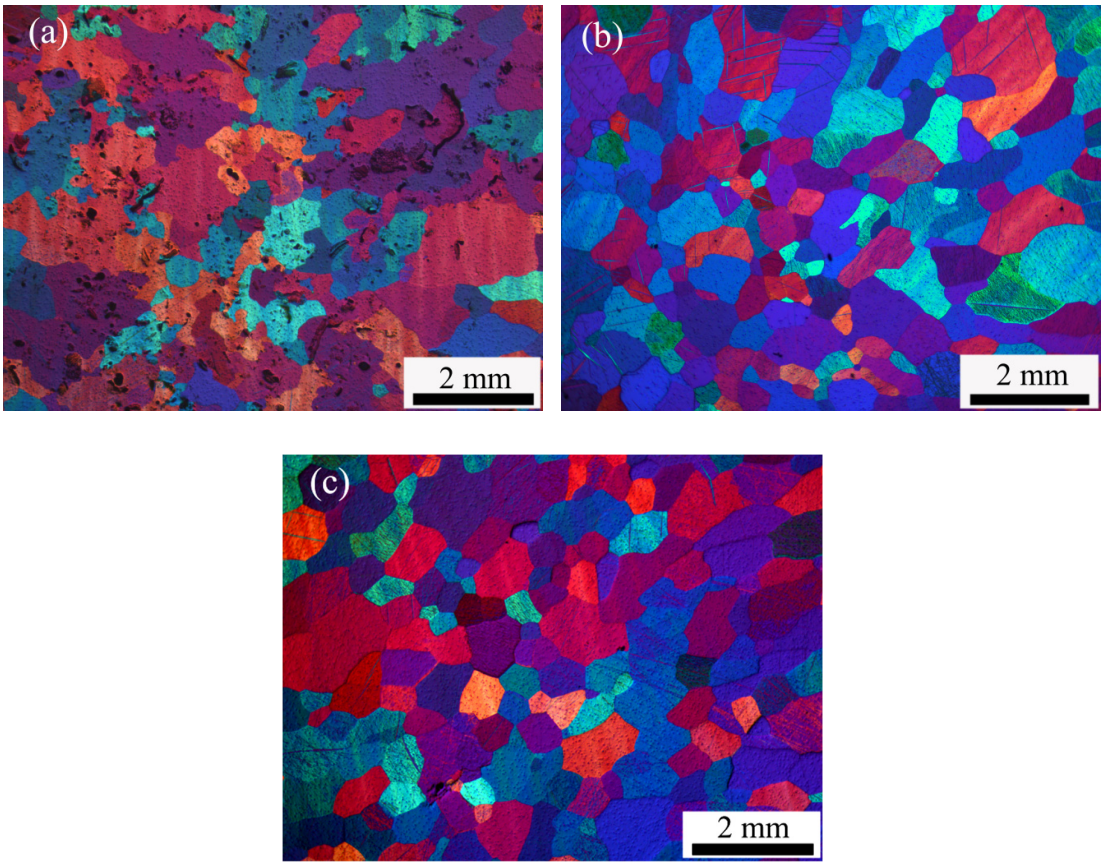

Fig. 5-42 Optical micrographs of Mg-1Mn alloy by adding 0.5% SiC with different particle sizes: (a) 0.1~1 µm; (b) 2 µm; (c) 10 µm

Fig. 5-43 shows the XRD patterns of as-cast Mg-1Mn-0.5SiC system with different SiC particle size condition. Only Mg peaks can be detected in both Mg-1Mn-0.5SiC (2 μm) and Mg-1Mn-0.5SiC (10 μm) alloys, verifying that no (or very few) SiC was left. This agrees with the results of Fig. 5-42(b) and Fig. 5-42(c). Peaks at $2\theta = 43.3^{o}$ and $2\theta = 45.2^{o}$ can be detected in Mg-1Mn-0.5SiC (0.1~1 μm) alloys, which is matching the SiC phase that appears in SiC powder pattern.

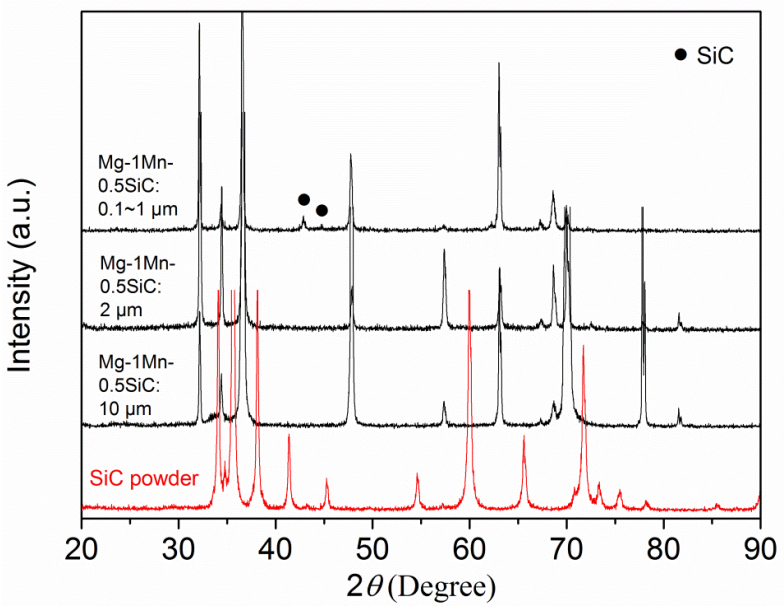

Fig. 5-43 XRD patterns of Mg-1Mn-0.5SiC system with different SiC particle size condition. Pattern of SiC powder was used in comparison. The peaks corresponding to Mg are not labeled

5.2.3.3 Addition temperature

Fig. 5-44 shows the variation of average grain size with addition temperature for Mg-1Mn-0.5SiC alloy system. The average grain size continuously decreases from 560 ± 18 to 460 ± 13 μm with the increase of addition temperature from 700 °C to 760 °C.

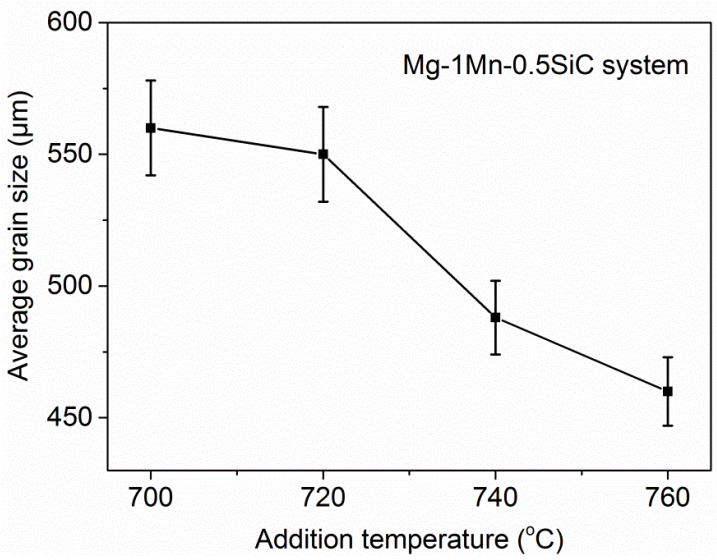

Fig. 5-44 Variation of average grain size with addition temperature for Mg-1Mn-0.5SiC alloy system

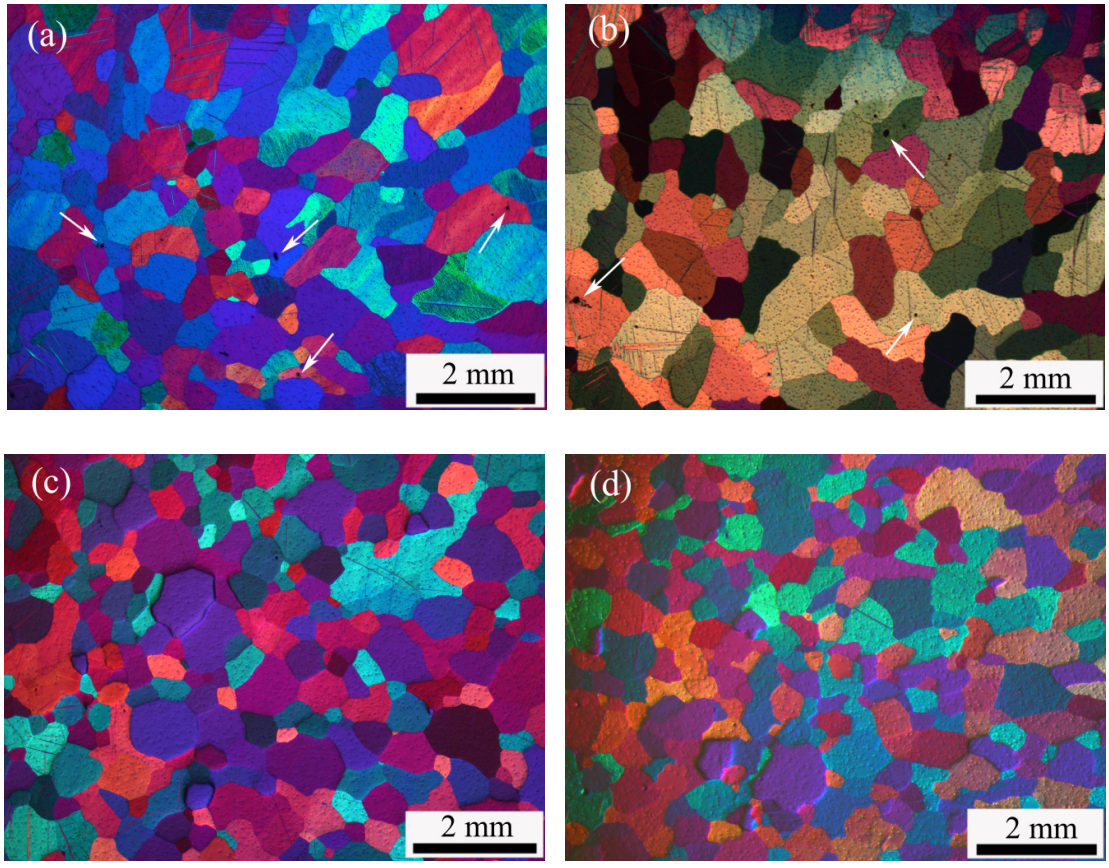

Fig. 5-45 Optical micrographs of as-cast Mg-1Mn alloys by adding 0.5% SiC particles under different addition temperatures: (a) 700 °C; (b) 720 °C; (c) 740 °C; (d) 760 °C

Fig. 5-45 shows the corresponding optical micrographs of as-cast Mg-1Mn alloys by adding

0.5% SiC particles under different addition temperatures. The columnar grains were suppressed to change into equiaxed grains as the addition temperature rises. Relatively homogeneous grain size morphologies were obtained in the alloys with the addition temperature of 740 °C and 760 °C. Some amount of SiC clusters can be found in the alloys with the addition temperature of 700 °C and 720 °C. However, no SiC clusters can be observed in the alloys with higher addition temperature, i.e. 740 °C and 760 °C.

5.2.3.4 Holding time

Fig. 5-46 shows the variation of average grain size with holding time for Mg-1Mn-0.5SiC alloy system. The average grain size continuously decreases from 572 ± 22 to 496 ± 15 μm with the increase of holding time from 0 to 60 min.

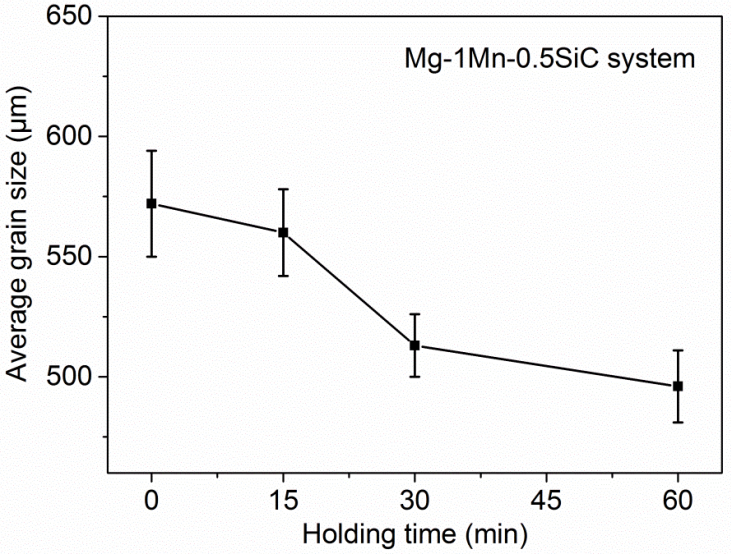

Fig. 5-46 Variation of average grain size with holding time for Mg-1Mn-0.5SiC alloy system

The corresponding optical micrographs of as-cast Mg-1Mn-0.5SiC alloys under different holding time conditions are shown in Fig. 5-47. The columnar grain morphologies were gradually suppressed with the increase of holding time from Fig. 5-47(a) to (d). A relatively homogeneous and equiaxed grain size distribution were observed when the holding time reaches to 60 min. Interestingly, the amount of SiC aggregations decreased with increasing the holding time. No or very few SiC clusters can be found in alloys under the holding time higher than 30 min.

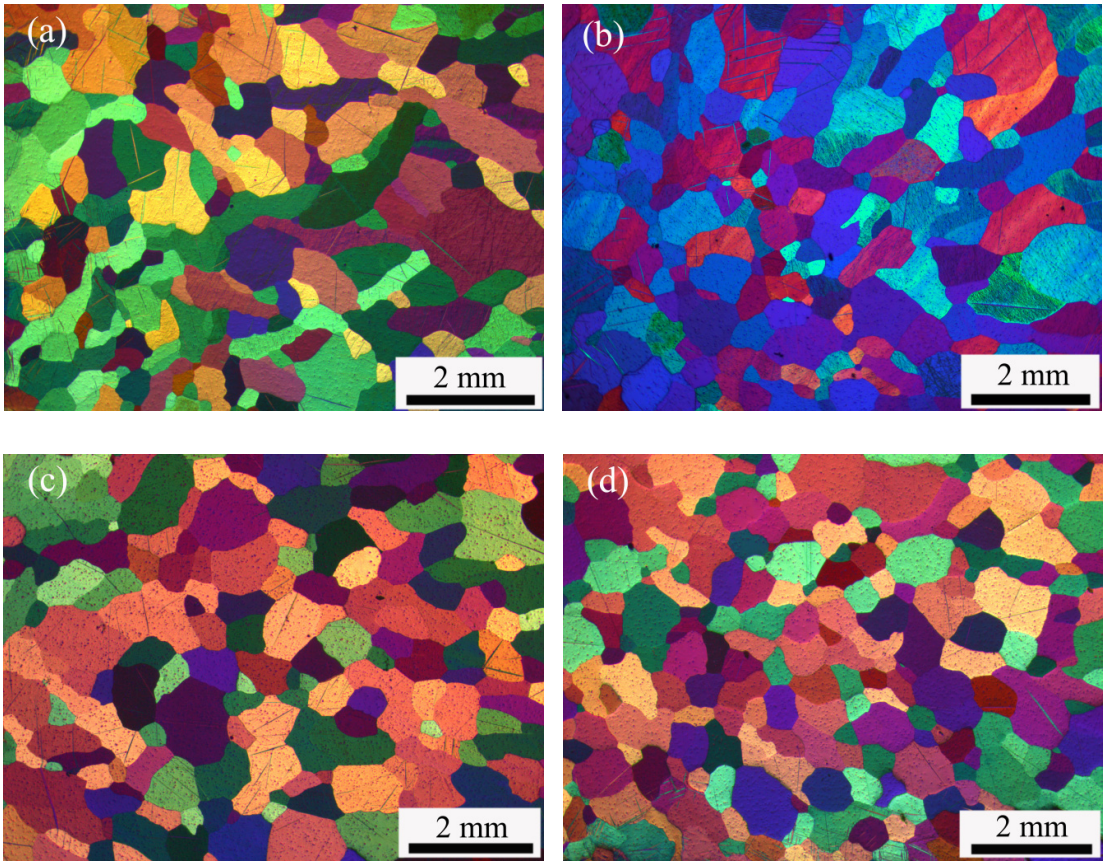

Fig. 5-47 Optical micrographs of as-cast Mg-1Mn-0.5SiC alloys under different holding time conditions: (a) 0 min; (b) 15 min; (c) 30 min; (d) 60 min

5.2.4 Characterization of nucleant particles in Mg-Mn-SiC alloy system

Fig. 5-48 (a) shows a BSE image of Mg-1Mn-0.3SiC alloy and its corresponding EDS mapping analyses are shown in Fig. 5-48(b) to (d). The discontinuous Mn enriched areas were distributed along the Mg grain boundaries. Especially, some particles with inside white and outside black contrast (indicated by white arrows in Fig. 5-48(a)) were observed in the center of Mg grains, which are possibly the nucleant particles. It clearly shows that those nucleant particles are enriched with Mn and Si elements, verifying that new Mn-Si phases were formed by the reaction between SiC and Mn in Mg-1Mn-0.3SiC alloy system.

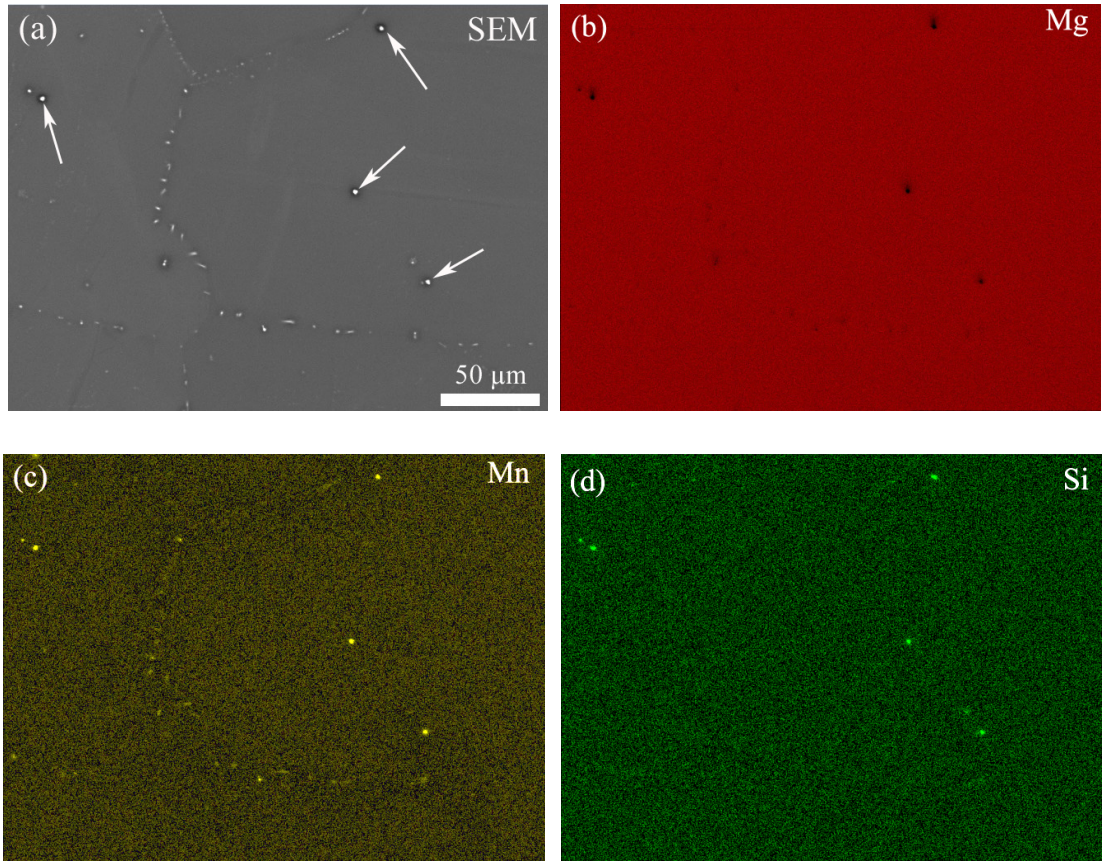

Fig. 5-48 BSE image and corresponding EDS mappings of Mg-1Mn-0.3SiC alloy. Nucleant particles are indicated by white arrows in Fig. 5-48(a)

In order to characterize and analyze the nucleant particles in detail, 30 nucleant particles were randomly probed and the six of them are shown in Fig. 5-49(a) to (f). Those nucleant particles have almost the same morphologies but with different diameters. The size distribution of the 30 probed nucleant particles is shown in Fig. 5-50. In addition, the corresponding EDS analysis results of Mn/Si ratio from the 30 probed nucleant particles are shown in Fig. 5-51.

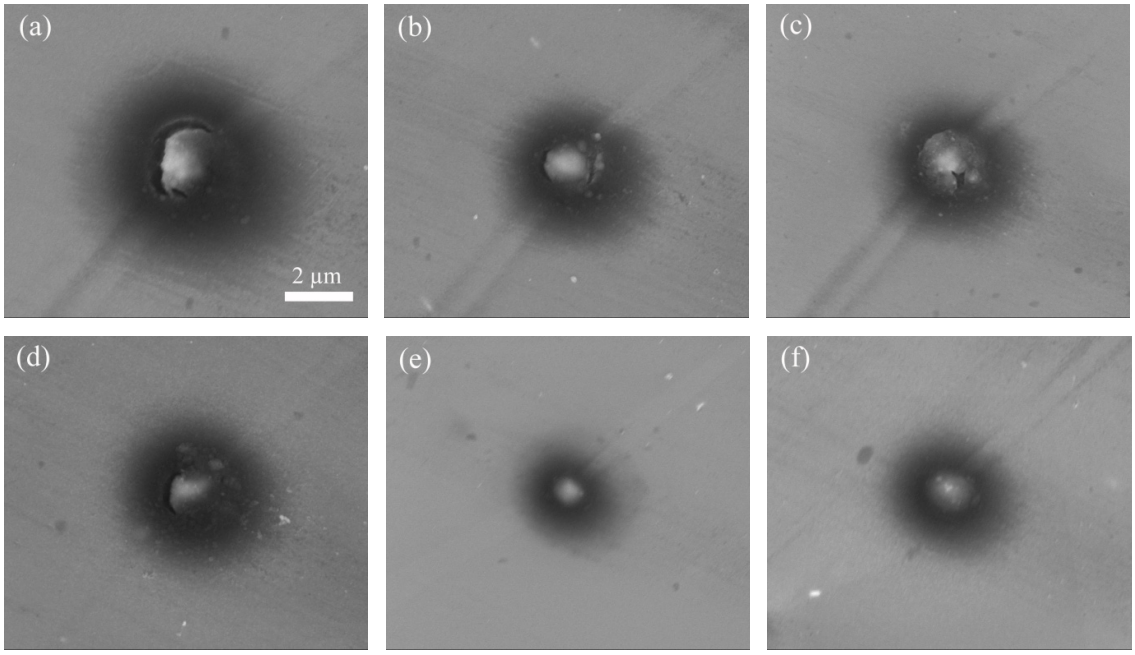

Fig. 5-49 SEM images of nucleant particles with different sizes in Mg-1Mn-0.3SiC alloy. The scale bars are not shown in (b) to (f) because all of them were taken at the same magnification as (a)

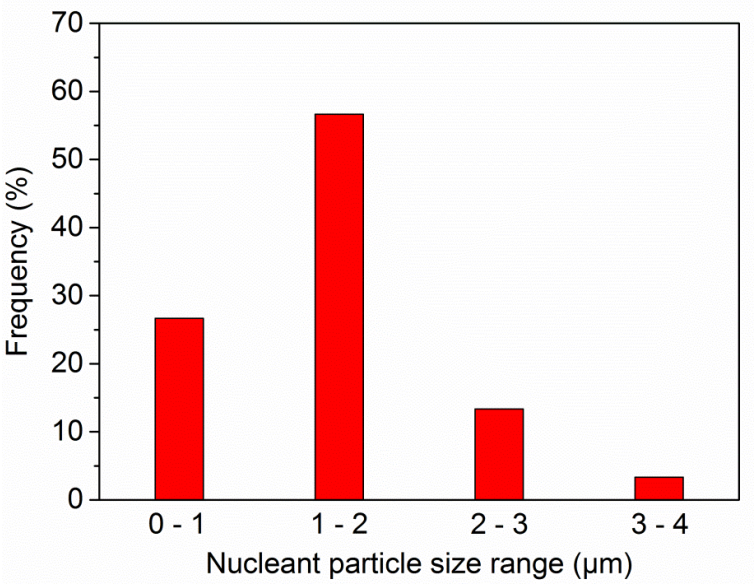

Fig. 5-50 Size distribution of the 30 probed nucleant particles

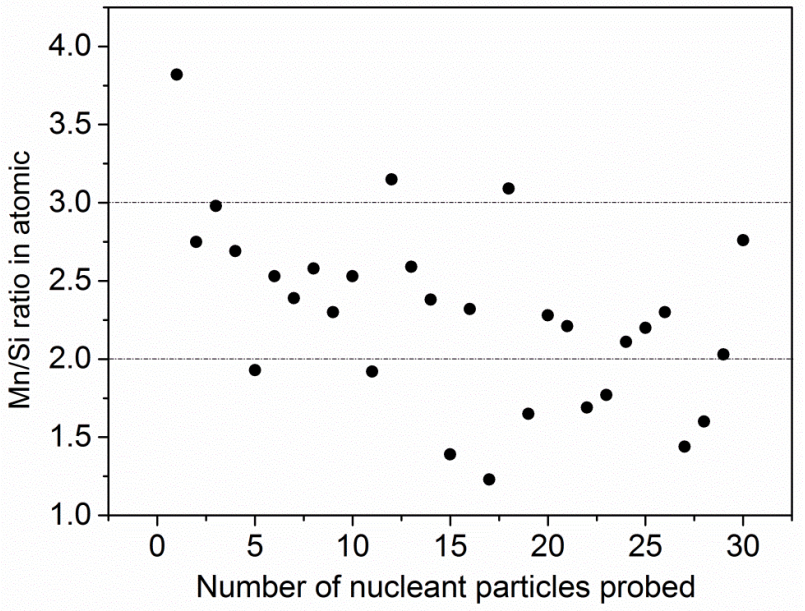

Fig. 5-51 Mn/Si ratio in atomic from the 30 probed nucleant particles by presenting in number order

It was found that the majority of the nucleant particles detected falls in the size range of 1-2 μm in Fig. 5-50, and its frequency reaches to 57%. This size range is close to that of the inoculated SiC particles with the diameter of 2 μm. Nucleant particles that are greater than 4 μm are not found. Nucleant particles with the size range of 0-1 μm are accounted for about 27%, and it should be noted that most of the particle sizes detected in this range is close to 1 μm. The frequency of the nucleant particles with the size range of 2-3 and 3-4 μm is 13% and 3%, respectively.

Fig. 5-51 shows the Mn/Si ratio in atomic from the 30 probed nucleating particles. The detected Mn/Si ratios were not uniform, which could be effected by the surrounding environment such as the Mg matrix and also the size of the probed nucleant particle. However, it clearly shows that most measurements of the Mn/Si ratios were found to fall in the range between 2 and 3. Those new formed nucleant particles could be Mn_3Si.

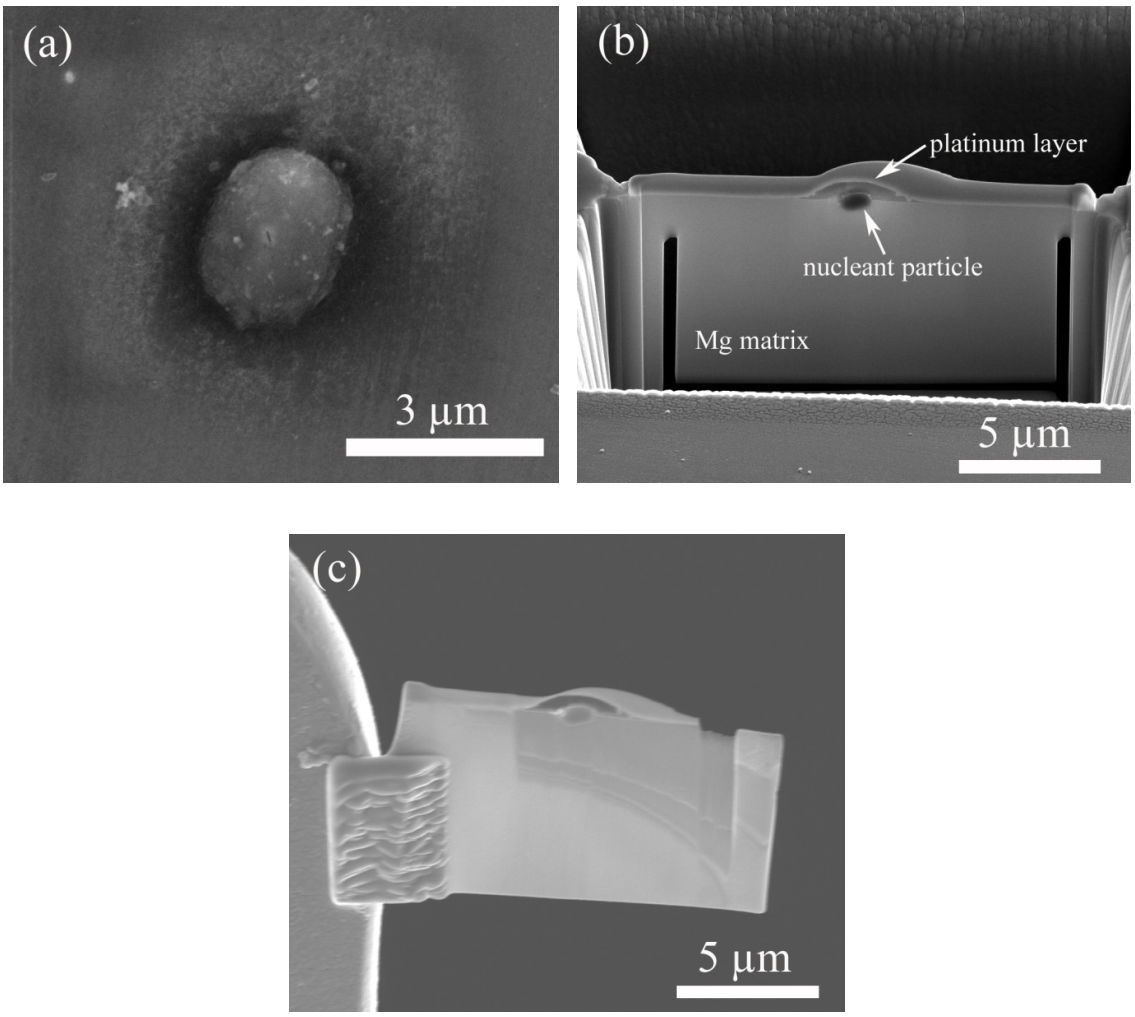

Fig. 5-52(a) SEM image of a selected nucleant particle in Mg-1Mn-0.3SiC alloy for the following FIB cutting process; (b) SEM image of the U-shape sample; (c) further thinning process by FIB for preparation of a sample fitted for TEM characterization

In order to identify the phase type of the nucleant particle, FIB cutting was used to prepare the site-specific TEM thin foil from a Mg-1Mn-0.3SiC alloy, as shown in Fig. 5-52(a) to (c). Platinum was deposited on the surface of nucleant particle before cutting in order to prevent the damage from FIB (Fig. 5-52(b)). A part of the Mg matrix belongs to the upper right corner in Fig. 5-52(c) is disappearing during the FIB cutting, indicating that the thickness of the sample has been very thin that can be characterized by TEM analysis.

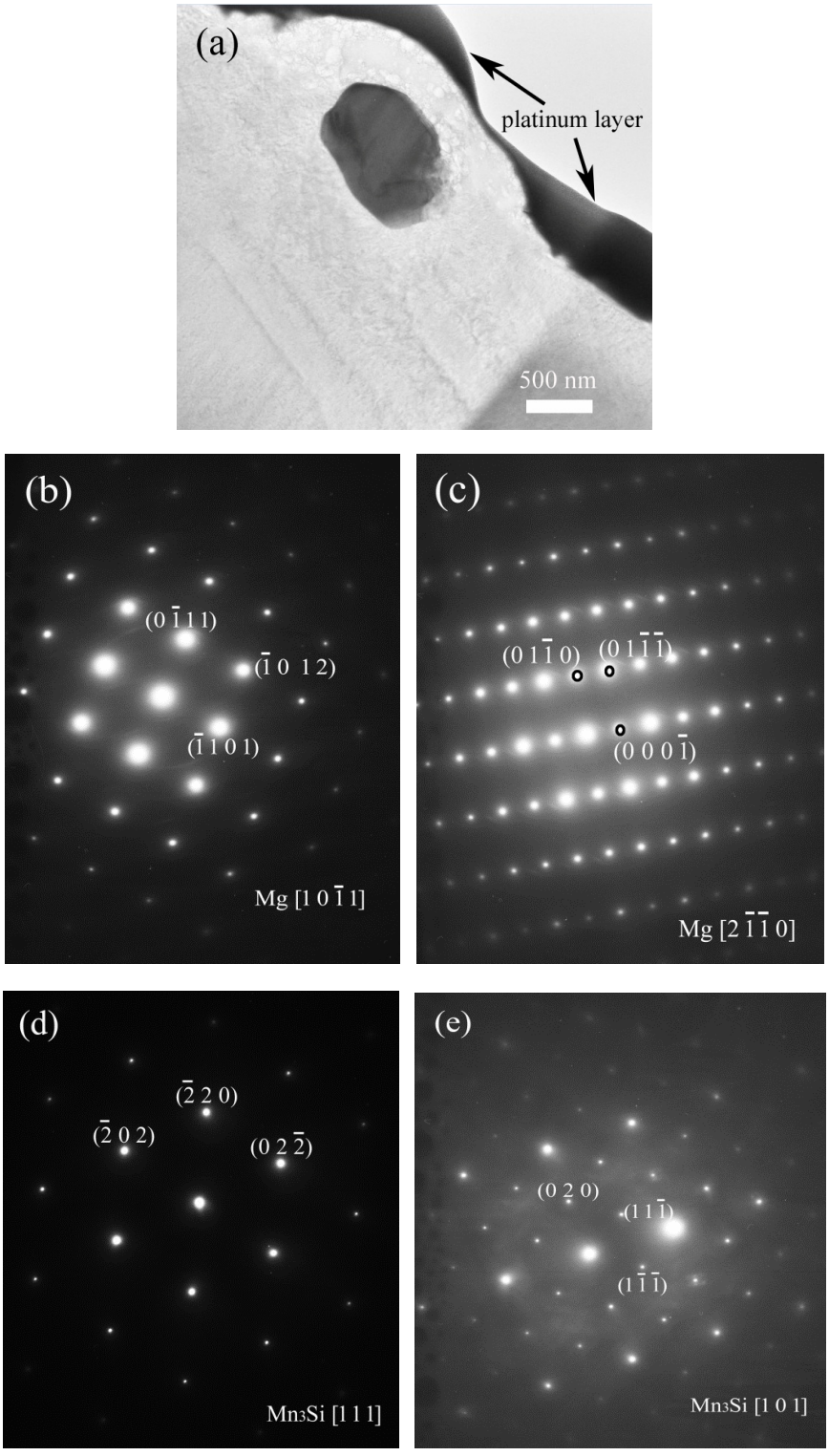

Fig. 5-53 Detailed TEM investigations of the nucleant particle prepared by FIB cutting: (a) bright-filed TEM image of the nucleant particle; (b) and (c) are the diffraction patters collected from the Mg matrix at the beam directions of $[1\ 0\ \bar{1}\ 1]_{Mg}$ *and* $[2\ \bar{1}\ \bar{1}\ 0]_{Mg}$*, respectively; (d) and (e) are the diffraction patters collected from the nucleant particle*

Fig. 5-53(a) is the morphology of the nucleant particle observed by TEM characterization. The nucleant particle with black contrast was embedded in the matrix with white contrast. Diffraction patters of Fig. 5-53(b) and Fig. 5-53(c) confirmed that the structure of the matrix is Mg, and the electron beam is parallel to $[1\ 0\ \bar{1}\ 1]_{Mg}$ and $[2\ \bar{1}\ \bar{1}\ 0]_{Mg}$, respectively. The corresponding diffraction patters taken from the nucleant particle with two different orientations confirmed that its structure is Mn_3Si. The beam direction in Fig. 5-53(d) and Fig. 5-53(e) are parallel to $[1\ 1\ 1]_{Mn3Si}$ and $[1\ 0\ 1]_{Mn3Si}$, respectively. The lattice parameters of Mn_3Si phase are $a = b = c = 0.5724$ nm with the space group $Fm\bar{3}m$. The lattice parameters of Mg are $a = 0.3209$ nm and $c = 0.5210$ nm with the space group $P63/mmc$.

Fig. 5-54(a) shows the superimposed diffraction pattern from nucleant particle and Mg matrix. The index of different facets from Mg or Mn_3Si in Fig. 5-54(a) can be identified accordingly in Fig. 5-54(b). It shows that the preferred orientation relationship (OR) between Mn_3Si and Mg follows the rule of $\Delta\mathbf{g}$ parallel to $\mathbf{g}$, i.e. Rule I classified by Zhang and Weatherly [146]. The OR obeys the following relationship: $\mathbf{g}_{(0\ 1\ \bar{1}\ 0)Mg}$ //$\Delta\mathbf{g_1}$ //$\Delta\mathbf{g_2}$, where $\Delta\mathbf{g_1} = \mathbf{g}_{(\bar{1}\ 1\ 0\ 1)Mg} - \mathbf{g}_{(\bar{2}\ 0\ 0)Mn3Si}$, $\Delta\mathbf{g_2} = \mathbf{g}_{(\bar{1}\ 0\ 1\ 1)Mg} - \mathbf{g}_{(\bar{2}\ 0\ 0)Mn3Si}$, as indicated in Fig. 5-54(b).

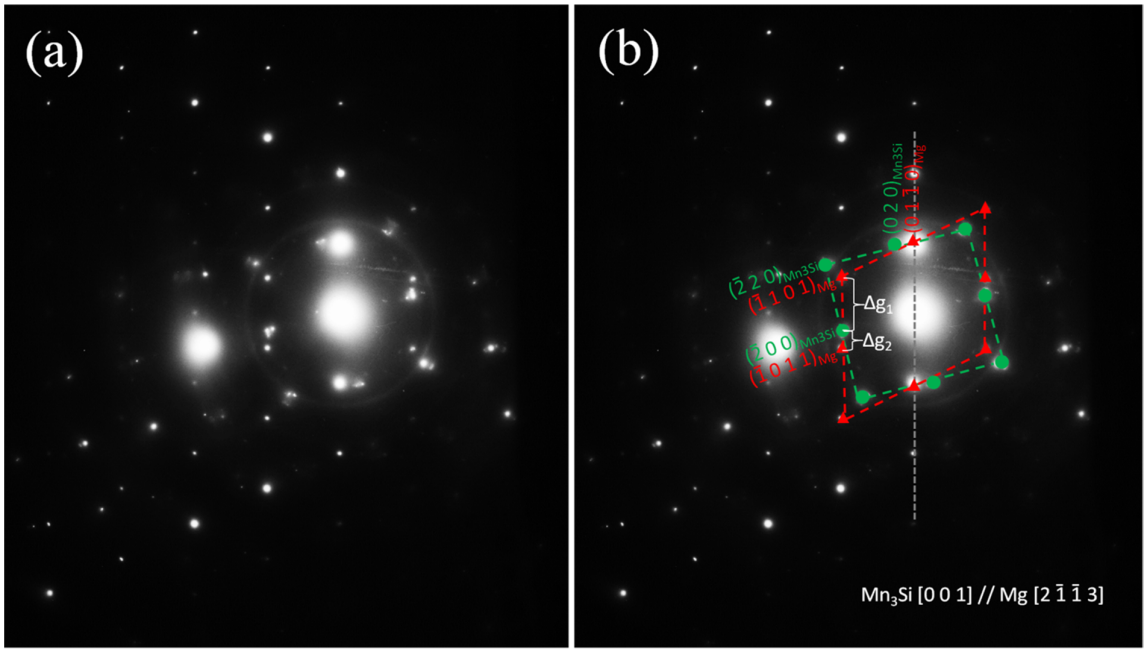

Fig. 5-54(a) Superimposed diffraction pattern of nucleant particle and Mg matrix. The electron beam is parallel to zone axis $[0\ 0\ 1]_{Mn3Si}$ // $[2\ \bar{1}\ \bar{1}\ 3]_{Mg}$ as shown in (b). The red triangles are indicated as Mg diffraction pattern, and the green circles are indicated as Mn_3Si diffraction pattern

5.2.5 Solidification simulation of Mg-Mn-SiC system

In general, a substrate (second phase) served as a nucleation site in Mg alloys should be formed prior to the formation of α-Mg phase. In order to reveal the thermodynamic driving force for nucleation process of Mg-Mn-SiC alloy system, normal solidification simulations based on Pandat software under Scheil conditions were carried out. The calculated results of phase formed sequence changed with increasing Mn addition in Mg-*x*Mn-0.3SiC alloy system were summarized in Table 5-4. The corresponding representative diagrams of phase formed sequence information vs. temperature were given in Fig. 5-55.

Table 5-4 Phase formed sequence changed with increasing Mn addition in Mg-xMn-0.3SiC alloy system, and the corresponding representative related to Fig. 5-55

Mn content	Phase formed sequence	Representative
0.00% ~ 0.55%	C_graph→hcp	–
0.55% ~ 0.62%	C_graph→hcp→SiC→Mn_5Si_3→Mg_2Si	–
0.62% ~ 0.85%	C_graph→hcp→Mn_5Si_3→SiC→Mg_2Si	Fig. 5-55(a)
0.85% ~ 1.34%	C_graph→Mn_5Si_3→hcp→SiC→Mg_2Si	Fig. 5-55(b)
1.34% ~ 1.51%	C_graph→Mn_5Si_3→Mn_3Si→hcp→SiC→Mg_2Si	Fig. 5-55(c)
1.51% ~ 1.55%	C_graph→Mn_3Si→Mn_5Si_3→hcp→SiC→Mg_2Si	Fig. 5-55(d)
1.55% ~ 1.84%	C_graph→Mn_3Si→hcp→Mn_5Si_3→SiC→Mg_2Si	Fig. 5-55(e)
1.84% ~ 2.0%	C_graph→Mn_3Si→Mn_9Si_2→hcp→Mn_5Si_3→SiC→Mg_2Si	Fig. 5-55(f)

The results show that SiC could react with the melt (at 700 °C or higher temperature) forming just graphite. The released Si is dissolved in the melt. SiC is not stable in the alloy until after α-Mg (hcp) precipitated at lower temperature. Mn contents severely affect the phase formed sequence as shown in Table 5-4. Except for the formation of C_graph phase, it was found that Mn-Si phases such as the Mn_5Si_3, Mn_3Si and Mn_9Si_2 could be served as nucleation sites as they can be formed prior to the formation of α-Mg within certain Mn contents range (see in Table 5-4). Mn_5Si_3 could be the most probable nucleation sites when the amount of Mn ranged from 0.85% ~ 1.51%. However, Mn_3Si could be the most probable nucleation sites when the amount of Mn ranged from 1.51% ~ 2.0%. In addition, Mn_3Si is more stable and favorite than that of Mn_5Si_3 when increasing the Mn content, as the precipitation of Mn_5Si_3

prior to α-Mg can be completely suppressed when the Mn content increased to 1.55%. Fig. 5-55(e) with the Mn content of 1.7% is a good example.

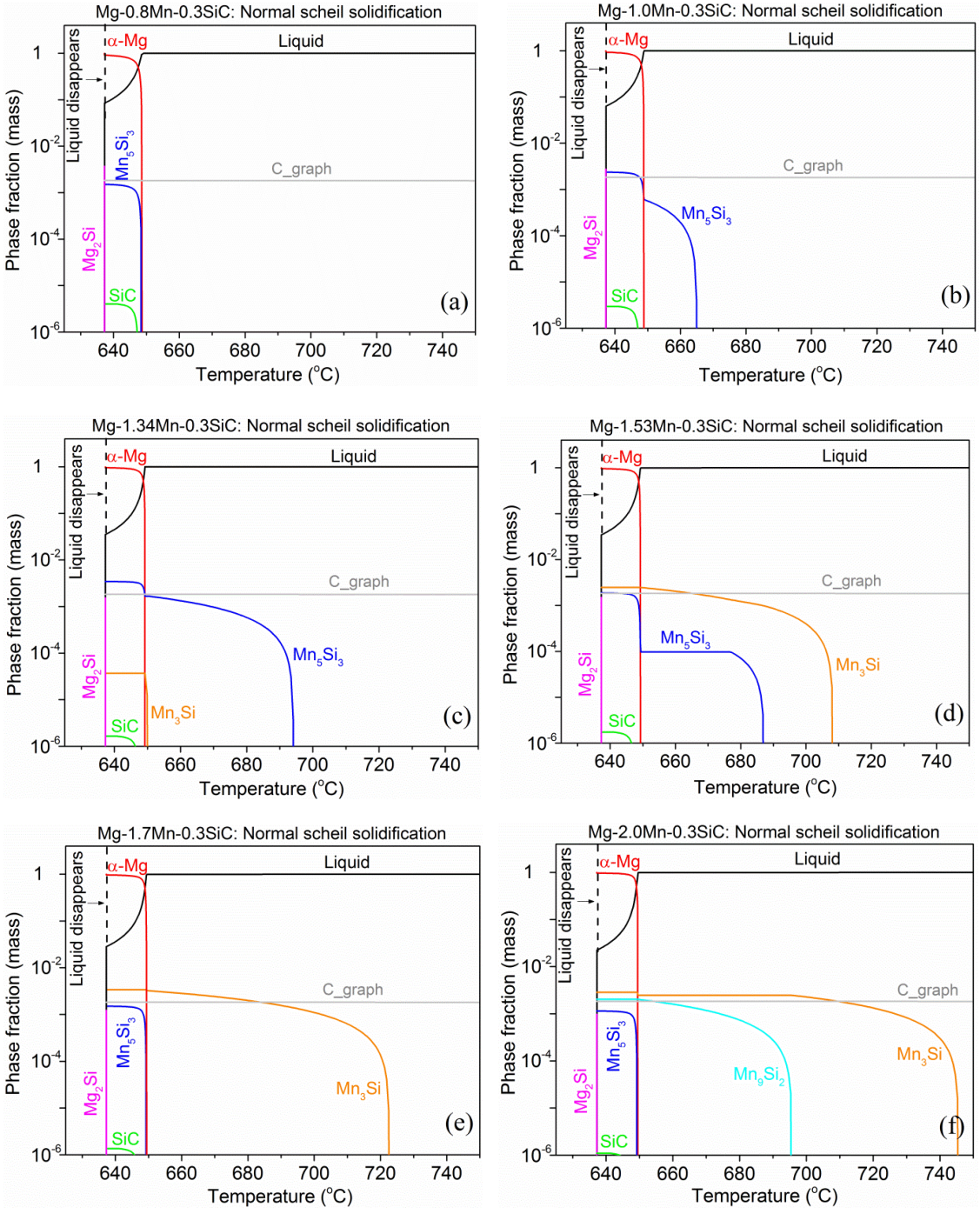

Fig. 5-55 Mass fraction of the second phases calculated for rapid solidification under normal Scheil conditions vs. temperature: (a) Mg-0.8Mn-0.3SiC; (b) Mg-1.0Mn-0.3SiC; (c) Mg-1.34Mn-0.3SiC; (d) Mg-1.53Mn-0.3SiC; (e) Mg-1.7Mn-0.3SiC; (f) Mg-2.0Mn-0.3SiC. Note that the inputted composition for calculation was given in wt%, e.g. Mg-1.0Mn-0.3SiC equals to 98.7%Mg+1.0%Mn+0.21%Si+0.09%C

6 Discussion

Based on the above results, the following part will focus on the role of solute element Zn and Mn in pure Mg. The effects of grain refining parameters on the grain sizes will be discussed in detail. The grain refining or poisoning mechanism will be proposed.

6.1 The role of solute element Zn and Mn in pure Mg

Based on the Eq. 2-5 and the corresponding parameters listed in Table 2-1, the Q value of Zn (5.31) is much larger than that of Mn (0.15), indicating more powerful segregation ability of Zn to develop CS zone in front of S-L interface, and hence higher grain refining effect. Fig. 6-1 shows the average grain sizes resulting from binary Mg-xZn and Mg-xMn alloys, i.e. data in Fig. 5-1(f) and Fig. 5-31(f) respectively, were plotted against 1/Q, which is analyzed based on the interdependence theory and fitted with Eq. 2-8. The corresponding values of the intercept a, the slope b and the correlation coefficient R^2 were summarized in Table 6-1.

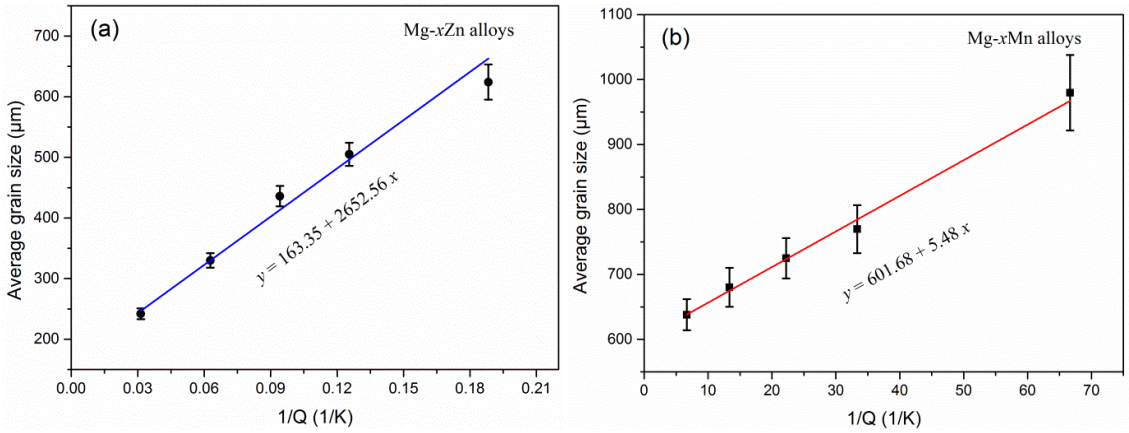

Fig. 6-1 (a) Average grain sizes were plotted against 1/Q for Mg-xZn binary alloys; (b) Average grain sizes were plotted against 1/Q for Mg-xMn binary alloys. Note that two graphs were plotted separately due to the huge difference between the 1/Q values of those two alloys

Table 6-1 Intercept a, slope b and R^2 values for linear fittings in Fig. 6-1

Alloy system	Intercept a (μm)	Slope b (μm•K)	R^2
Mg-xZn	163.35	2652.56	0.98
Mg-xMn	601.68	5.48	0.99

It is surprising that the value of *b* for Mg-Mn binary alloys is extremely low, indicating that the potency of the nucleant particles presented in this binary system (no matter whether they contained Mn or not) is much higher than those in the Mg-Zn binary system. However, despite of the very good potency of nucleant particles in Mg-Mn system, the value of the intercept *a* is comparatively higher than that of Mg-Zn system. This indicates that very few particles in Mg-Mn alloys can be effectively activated as nucleating substrates. It should be noted that the value of *b* for Mg-Zn alloys in the present study is much higher than that of StJohn's results, which is conversely close to the *b* value of Mg-Al binary system [4]. This discrepancy could be attributed to StJohn et al. [4] focused on the investigation on small Zn content range, i.e. Zn ≤ 1.06%, while in the present work it ranged from 1% to 6%. Second, to some extent the value of *b* for Mg-Zn alloys in the present work could be more reasonable as the parameters of Al and Zn in Table 2-1 are very close. In addition, as different raw materials were used by each side, a different range of *a* and *b* values could be obtained. This is due to the complicated role of impurities and/or their interaction with other alloying elements.

An interesting result is that one Fe-rich particle inside a Mg grain (marked as B in Fig. 5-3(a)) was identified by EDS mapping in Fig. 5-3(b3), which gives some direct evidence that impurities may also contribute to nucleation. As this particle shows a very small size, in this case, higher degree of constitutional undercooling is needed to trigger it to serve as a nucleus according to the free growth model [26]. In Mg-3Zn alloy, if the amount of constitutional undercooling generated by Zn segregation is enough, some *in-situ* intermetallic particles, such as Fe-containing, might be activated as powerful nucleants for the primary α-Mg.

Assuming that the actual temperature gradient in the melt is negligible or very low, Easton and StJohn [66] recently proposed a quantitative model to calculate the development of constitutional undercooling (ΔT_{cs}) with solid fraction, which is already given in Eq. 2-22. This is reasonable due to the high thermal conductivity of the melt. It is well accepted that an increase in the rate of development of the CS zone decreases the time and amount of growth required for nucleation events [66, 69]. Thus, smaller grains are finally obtained. Fig. 6-2 shows the development of the CS zone, ΔT_{cs} with solid fraction for different contents of solute element in binary Mg-Mn, Mg-Fe and Mg-Zn alloys. Considering at the same initial

composition, e.g., 1%, of Mn, Zn and Fe in Mg, the lowest increase in the ΔT_{cs} upon Mn addition indicates that Mn has little effect on grain refinement of Mg. This also means that even if some potent nucleant particles appear in Mg-Mn binary alloys, those particles cannot be effectively activated by Mn additions as the initial rate of development of the CS zone at the earliest stage is very low, i.e. the CS generated by Mn is not enough to trigger the nucleation process, which agrees with the previous discussions for Fig. 6-1(b) and Table 6-1 very well. The rate of development of the CS zone in front of S-L interface for Mg-Zn alloys increased with the increase of Zn content. The addition at higher content of Zn, such as 3% and 6%, has significant effect on grain refinement of Mg, which also supports the results of Fig. 5-1. It should be noted that in our study, the content of Fe in commercial pure Mg is around 50 ppm to 100 ppm. As shown in Fig. 6-2, the rate of development of the CS zone for such a content 0.01% Fe (equals to 100 ppm) is still quicker than that for 1% Mn, indicating that only small amount of Fe would affect the grain refinement process significantly.

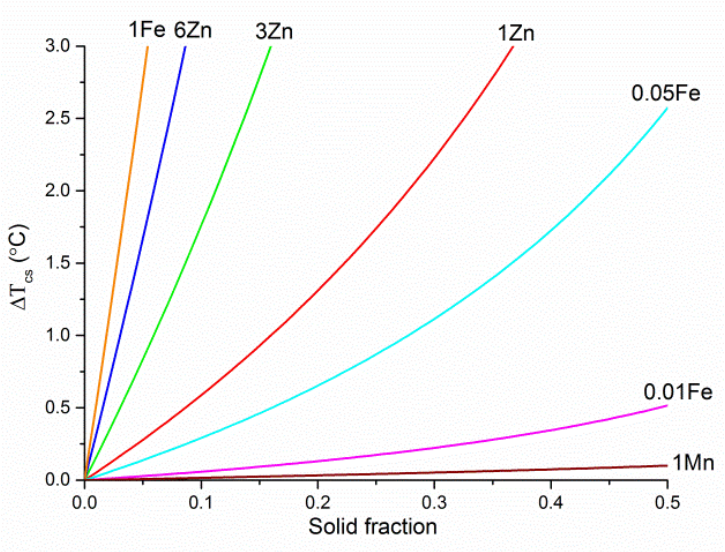

Fig. 6-2 The development of the CS zone, ΔT_{cs} with solid fraction for different contents of solute element in binary Mg-Mn, Mg-Fe and Mg-Zn alloys based on Scheilian solidification behavior. This was calculated from Eq. 2-22 using the parameters in table 2-1, and the initial alloy content at each curve was given in wt%

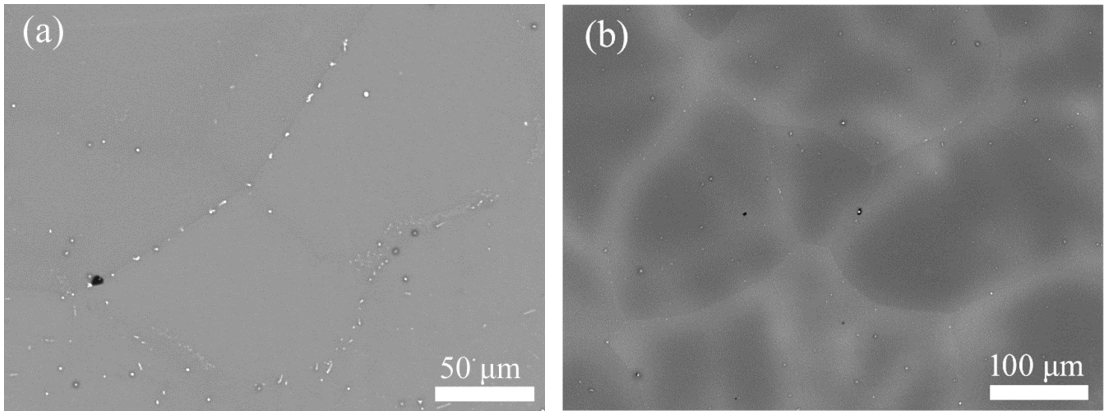

Fig. 6-3 BSE images of the as-cast alloys: (a) Mg-1.0Mn; (b) Mg-1.0Zn

Fig. 6-3 shows the BSE images of the as-cast Mg-1.0Mn and Mg-1.0Zn alloys. For binary Mg-1.0Mn alloys, fine α-Mn particles with white contrast were also observed within the grains or along the grain boundaries, which is similar to that of Mg-0.1Mn alloy as shown in Fig. 5-33. No segregations of Mn were observed even in Mg-1.0Mn alloy, supporting that the effect of Mn addition on grain refinement of Mg could be moderate. In contrast, only 1% Zn in pure Mg can already generate severe segregation (Fig. 6-3(b)).

Therefore, the addition of Zn or Mn solute element to commercial pure Mg leads to a reduction in grain size. The effect of Zn is mainly attributed to its segregation power, i.e. the CS contribution, which in turn helps to activate some native potent particles to serve as nuclei. The *in-situ* formed nucleant particles introduced by Mn additions in Mg are more potent than that in Mg-Zn binary system, but cannot be triggered effectively for the nucleation process on them due to the very low segregation ability of Mn. It is proposed that the CS driving-force arising from solute segregation in front of the S-L interface is even more important and necessary when an effective nucleant is presented in the melt than without.

6.2 Grain refinement of Mg-Zn alloys by SiC inoculation

6.2.1 Effects of Zn contents

Based on the discussion results in part 6.1, the interaction between the solute element Zn and SiC inoculant is necessary to be investigated. If the addition amount of the inoculant is given as a constant, the relative reduction percentage (RP) of average grain size changed with different amount of solute can be calculated as follows:

$$RP = (d_B - d_A) / d_B \quad 6\text{-}1$$

where d_B is the average grain size of the alloy system before inoculation, and d_A is the average grain size of the alloy system after the addition of certain amount of inoculants. Considering that the same amount of 0.3% SiC was added into Mg-*x*Zn alloy system and by using the data in Fig. 5-6, the RP of average grain size with different Zn content is shown in Fig. 6-4. It clearly shows that RP increases with increasing Zn contents up to 3% Zn. The RP of Mg-3Zn alloy with 0.3% SiC addition reaches to 45%.

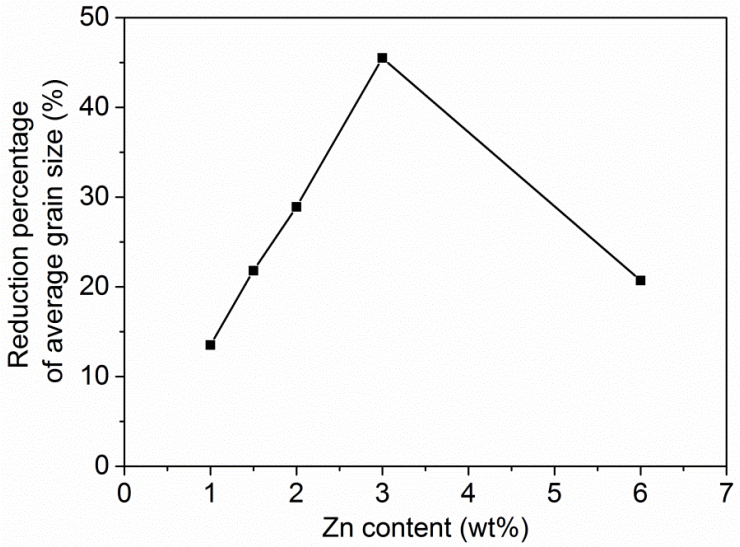

Fig. 6-4 Reduction percentage of average grain size with different Zn content in Mg-xZn-0.3SiC alloy system

Interestingly, an inferior grain refining effect was obtained at too high solute composition in Fig. 6-4, i.e. 6% Zn. In addition, the grain size of Mg-6Zn-0.3SiC alloy became slightly larger than that of Mg-3Zn-0.3SiC alloy as shown in Fig. 5-5(f). This could be due to the capillary effects [147] for too high content of solute element, as shown in Fig. 6-5. Increasing solute content from region 2 to region 3 will reduce the dendrite tip radius, which counteracts the solute effect. If the dendrite tip radius eventually decreases to a critical value, the capillary effect will dominate gradually and then the growth rate increases, leading to the increase of final grain size. When the solute content is low in region 1, the as-cast microstructure is columnar and the growth is controlled by thermal conditions. Increasing the solute content into region 2, the growth rate will decrease and lead a transition to diffusion-controlled

equiaxed growth [147]. This interpretation supports the results of Fig. 5-5, Fig. 5-6 and Fig. 6-4. Liu et al. [144] reported that a novel Al_4C_3–SiC/Al master alloy for grain refinement of Mg-Al-Zn alloys presents good grain refining efficiency in both AZ31 and AZ63 alloys, but little effect on AZ91 alloy, which also indicates that too high content of solute element has no much help or even interferes with further grain refining effect.

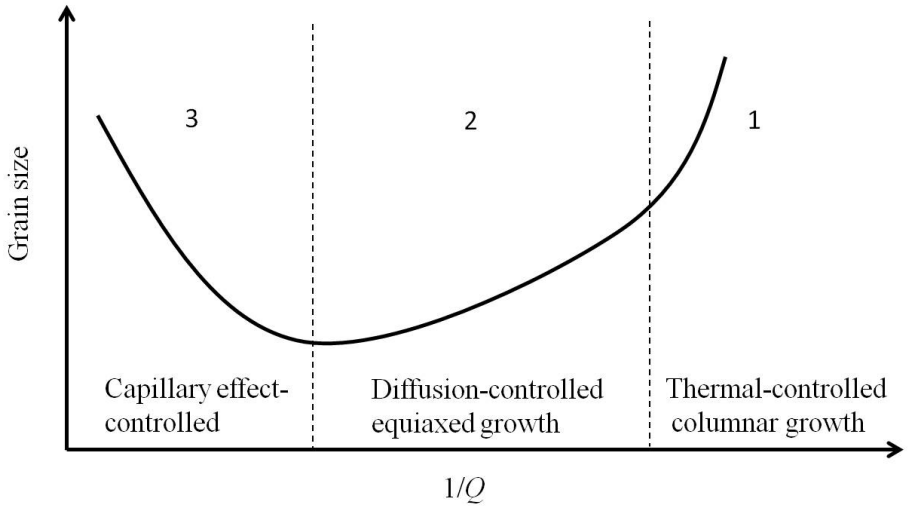

Fig. 6-5 Schematic illustration showing how the composition range of solute element related to the 1/Q value affects grain size. The solute content increases to the left in the figure

Fig. 6-6 shows the average grain size resulting from Mg-*x*Zn and Mg-*x*Zn-0.3SiC alloys plotted against 1/*Q* based on the interdependence theory and fitted with Eq. 2-8. The corresponding values of the intercept *a*, the slope *b* and the correlation coefficient R^2 were summarized in Table 6-2.

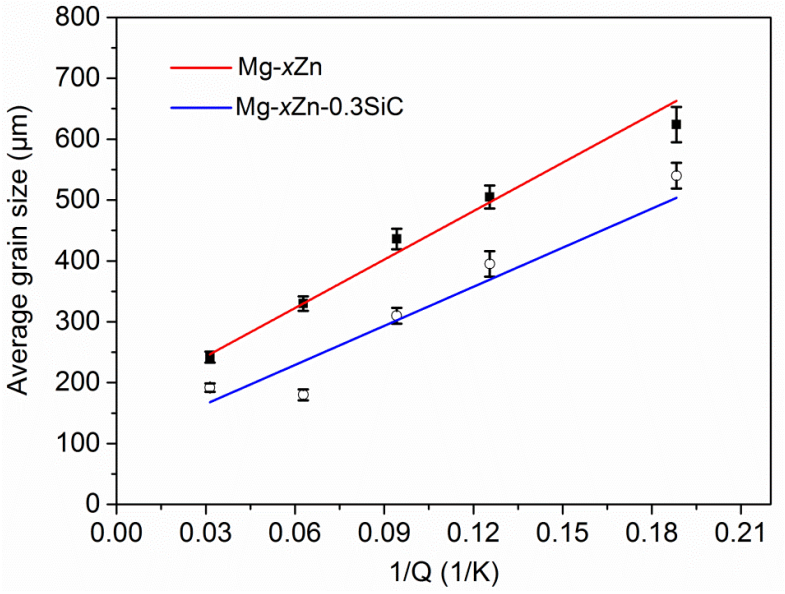

Fig. 6-6 The average grain sizes plotted against 1/Q for Mg-xZn and Mg-xZn-0.3SiC alloy system

Table 6-2 Intercept a, slope b and R^2 values for linear fittings in Fig. 6-6

Alloy system	Intercept *a* (μm)	Slope *b* (μm•*K*)	R^2
Mg-*x*Zn	163.35	2652.56	0.98
Mg-*x*Zn-0.3SiC	100.67	2139.78	0.81

The resulting average grain size shows a clear linear relationship with 1/*Q* for both alloy systems. When 0.3% SiC was added into Mg-*x*Zn alloy system, both the value of intercept *a* and the slope *b* decreased (see in Table 6-2). This indicates that the addition of SiC leads to the increase of the activated nucleation sites, and also the potency of the nucleant particles is much higher than those in the Mg-Zn binary system without inoculation process. Based on the interdependence theory, some other known or unknown native nucleant particles should exist in the melts [4]. However, the sizes of those native nucleant particles are normally very small or even at the nanometer scale [62]. In addition, both superheating [98] and native grain refinement [99] phenomena reported in binary Mg-Al alloys suggested that impurities from commercial pure Mg may play an important role to affect the grain refining process. Therefore, if SiC reacts with small Mn and Fe particles to form bigger nuclei, it will lead to the results that the number of effective nucleation sites increases and much lower degree of constitutional undercooling is needed to trigger the nucleation process according to equation

2-4, i.e. the free growth model. All of the characterization results of nucleant particles in section 5.1.4 and the HP comparative test in Fig. 5-21 fully proved the above discussions. Therefore, the combinations between Zn solute with relatively high Q value and potent nucleation sites that originated from chemical reaction by SiC inoculants and impurities contribute to the grain refining effect.

6.2.2 The role of SiC in Mg-Zn system

6.2.2.1 SiC addition amount

SiC contents varied from 0.3% to 0.5% are the optimized addition amount for the grain refinement of Mg-3Zn alloys, as shown in Fig. 5-7. Further addition of SiC leads to the aggregation of this particle in Fig. 5-8(c). When 10% SiC was added into the melt, part of the added SiC floating on the melt surface can be found before casting even after vigorously stirring. This might be due to the poor wettability between SiC and the melt or an increase in viscosity with higher SiC composition. Hence, the efficiency of grain refinement effect is reduced. Conversely, when the content of SiC was less than 1%, especially lower than 0.5%, SiC can be added into the melt well and distributed uniformly.

Until now, it is not clear that whether some SiC particles could act as heterogeneous nucleation sites themselves. Theoretically, assuming that (i) the preferred OR for Mg/SiC is randomly scattered across the SiC particles, and (ii) each SiC particle is acting individually, then the greater the number of SiC particles, the greater is the probability of the preferred SiC orientation and hence greater should be the refining capability with higher amount of SiC addition. However, the opposite results suggest that the grain refinement effect is saturated after the addition of 0.5% SiC in the present work. Considering the characterizations of the nucleation sites in Fig. 5-18, Fig. 5-19 and Fig. 5-20, SiC particle partly reacted with Mn and Fe impurities to form Fe-Mn-Si rich intermetallic phase served as a nucleation site, which is attributed to the grain refinement. As only small amount of Mn (0.030%) and Fe (0.007%) existed in the source materials (Table 5-1), the demand of SiC particles required for the reaction between SiC and those elements is also low. In fact, relative overdose of SiC addition is needed because some of the SiC particles always aggregated together to be settled down during the holding time period. In addition, Inem et al. [148, 149] investigated the nucleation

and crystallographic orientation of both the Mg matrix and the eutectic $Mg(ZnCu)_2$ phases at the SiC particle surface in ZC63 and ZC71 Mg matrix composites. They found that the eutectic nucleates at the particle surface with an identical crystallographic orientation, but no distinct crystallographic orientation between α-Mg and SiC particle was observed. This also indicates that SiC cannot serve as heterogeneous nucleation sites themselves in Mg alloy system.

6.2.2.2 The particle size of SiC

Those SiC particles reacted with Mn and/or Fe elements to form the Fe-Mn-Si rich intermetallic phases can be served as nucleation sites, which play an important role in grain refinement of Mg-Zn alloys. However, the presence of large SiC clusters or unreacted SiC particles is frequently observed in the optical micrographs. A thorough understanding of the settling behavior of unreacted SiC particles is important for optimizing the alloying process with SiC and obtaining the best grain refining effect. The particle size, the addition temperature and the holding time will affect its settling behavior. Based on previous research [11, 12] and Newton's second law of motion, the settling of SiC particles in a stationary melt can be reasonably described by:

$$S_d \approx \frac{g(\rho_P - \rho_L)d^2}{18\eta}t \qquad 6\text{-}2$$

where S_d is the settling distance, g is the gravitational acceleration, ρ_P represents the density of inoculant particle, ρ_L represents the density of molten alloy system, d is the inoculant particle size, η is the viscosity of molten alloy system, and t is the settling time. Accordingly, the liquid density of multi-component systems, i.e. ρ_L, as a function of temperature could be estimated as follows [150]:

$$\rho_L = \sum_{i=1}^{n} Y_i\rho_{L,i} - [(\sum_{i=1}^{n} Y_i \frac{K_i}{\rho_{m,i}})(\sum_{i=1}^{n} Y_i\rho_{L,i})](T - T_L) \qquad 6\text{-}3$$

where Y_i is the atomic fraction of element i in the alloy, $\rho_{L,i}$ is the liquid density of element i, K_i is a constant value of element i, $\rho_{m,i}$ is the liquid density of element i at the melting point, T represents the actual temperature of the molten alloy system, T_L is the liquidus temperature of the alloy system. The $\rho_{L,i}$ can be calculated as follows [151]:

$$\rho_{L,i} = \rho_{m,i} - K_i(T - T_L) \quad (6\text{-}4)$$

In addition, the viscosity of molten alloy system, η, as a function of composition and temperature could be estimated as follows [152]:

$$\eta = A \exp(B/RT) \quad (6\text{-}5)$$

$$A = \frac{1.7\times10^{-7}\rho_L^{2/3}T_L^{1/2}M^{-1/6}}{\exp(B/RT_L)} \quad (6\text{-}6)$$

$$B = 2.65\ T_L^{1.27} \quad (6\text{-}7)$$

where *M* is atomic weight, and *R* is the gas constant.

The data for calculation of ρ_L and η are given in Table 6-3. Also, the T_L for Mg-3Zn system is 640.7 °C, and the density of SiC is 3.30 g•cm^{-3} [13].

Table 6-3 K and ρ_m data for Mg, Zn and Mn element [151]

Element	*K* (g•cm^{-3}•°C^{-1})	ρ_m (g•cm^{-3})
Mg	1.584	2.340× 10^{-4}
Zn	6.570	1.100 × 10^{-3}
Mn	5.950	1.050 × 10^{-3}

Fig. 6-7 shows the predicted effect of SiC particle size on settling distance plotted against settling time at 700 °C. Similar to the settling behavior of any solid particle in a given media, the settling of unreacted SiC particles in Mg-3Zn melts is also significantly affected by the particle size. Large SiC particles (~10 μm) can sink about 70 mm within the holding time of 15 min, while small SiC particles (~2 μm) only settle slightly about 3 mm. From a practical point of view, these SiC particles with small sizes will be maintained in the melt in most cases unless the settling time is sufficient, which ensures the reaction process between SiC and impurity elements leading to the good grain refining effect. It should be noted that 0.5 μm SiC was used as a substitute for 0.1~1 μm SiC inoculant in this calculation. It is reasonable because the settling distance at the size range of 0.1~1 μm is always limited on the macro-scale under the certain casting condition. The highest number density of particle is existed in 0.1~1 μm SiC inoculation system with the same addition amount of 0.3% SiC. In

addition, different settling distances still exist on the micro-scale because of the 0.1~1 μm spectrum, leading to more chances for particles to interact and then form clusters. Furthermore, no high intensity physical process such as ultrasonic vibration technology was applied during casting. Therefore, the aggregation and sedimentation of sub-micrometer SiC happens frequently in this system. This is why the big SiC clusters can be found in Mg-3Zn-0.3SiC (0.1~1 μm) system as shown in Fig. 5-13(a). The grain refining effect reduces accordingly compared with that of Mg-3Zn-0.3SiC (2 μm) system.

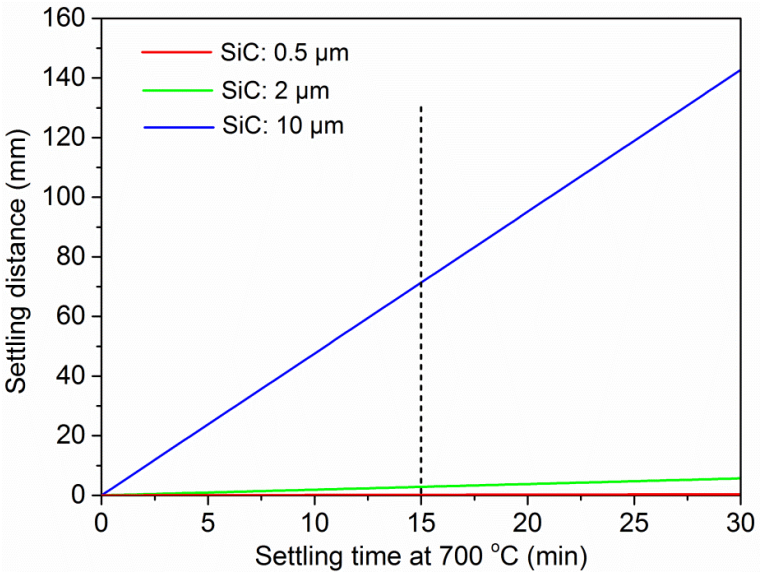

Fig. 6-7 Effect of SiC particle size on settling distance plotted against settling time at 700 °C

6.2.2.3 The addition temperature

Fig. 6-8 shows the effect of the addition temperature varied from 700 to 760 °C on settling distance plotted against settling time. The settling behavior of unreacted SiC particles in Mg-Zn system is only moderately influenced by the melt temperature. This finding agrees well with the results of Fig. 5-15 as no much difference for the overview of SiC in optical micrographs. However, the grain refining effects are strongly affected by the addition temperature in Fig. 5-14 and Fig. 5-15. If the addition temperature is higher, the longer time is needed to reduce the melt temperature back to 700 °C, i.e. the casting temperature. The inoculation fading during casting is a common phenomenon for grain refining treatment, which results from the melting, aggregation and sedimentation of the nucleation sites. Although potent nuclei can be formed by the reaction between SiC and impurities in all of

these systems, no new and fresh nuclei can be formed at later stage due to the limited amount of impurities. High addition temperature condition gives much time for nuclei impinging with each other and then settling down, leading to the decrease of grain refining effect.

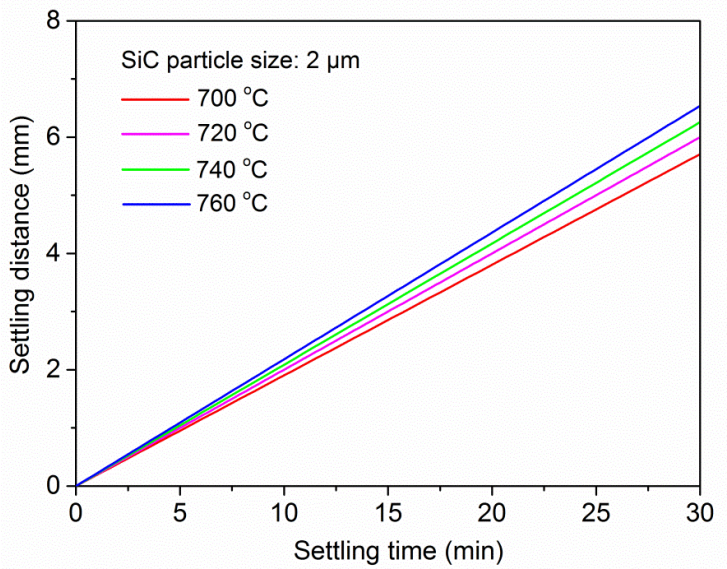

Fig. 6-8 Effect of the addition temperature varied from 700°C to 760°C on settling distance plotted against settling time

6.2.2.4 The holding time

The longer the holding time, the less the number of the effective nucleation sites due to inoculation fading. The results in Fig. 5-16 and Fig. 5-17 indicate that the sensitivity of the used SiC inoculation to fading is relatively high and the longest holding time should not exceed 30 min. The grain size of the casting sample obtained directly after the stirring, i.e. the holding time is recorded as 0 min, is slightly larger than that of the sample obtained after holding time of 15 min. This is because the reaction between SiC and impurities could be occurred during the addition and stirring process, but the reaction ratio is not sufficient for limited contacting time. Therefore, the number of the effective nuclei decreases correspondingly, leading to the reduced grain refining efficiency.

An enormous difference in the settling distance is observed when the holding time increases from 15 to 60 min in Fig. 6-9. The higher the holding time, the longer settling distance can be obtained. In addition, long holding time gives much chance for aggregation and sedimentation

of the SiC particles and nucleation sites. Therefore, the grain size is coarsened and also SiC clusters can be found in Fig. 5-17(c) and Fig. 5-17(d).

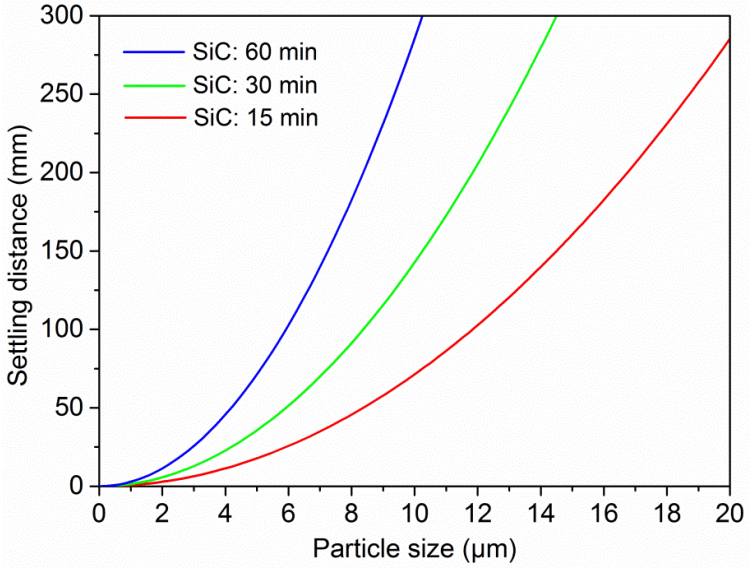

Fig. 6-9 Effect of the holding time condition on settling distance plotted against particle size

6.2.3 Poisoning mechanism of element Al in Mg-Zn-SiC system

The grain size of Mg-3Zn-0.3SiC alloy system is dramatically coarsened when the addition of Al is less than 0.1%, but decreased by adding more Al up to 1%. Based on the results of section 5.1.5, it is proposed that the poisoning effect of small amount addition of Al is due to the formation of $Al_8(Mn,Fe)_5$, which interferes with the reaction between SiC and Mn (Fe) to form potent Fe-Mn-Si nuclei. The comparative test of HP Mg-3Zn-0.3SiC-0.1Al alloy with no poisoning grain refinement effect in Fig. 5-25 directly supports this point. The grain refinement effect observed with further Al addition is caused by the solute effect of Al.

In general, there are three commonly accepted heterogeneous nucleants when Al and C-containing sources appear in Mg alloys, i.e., Al_4C_3, Al_2CO and $Al_8(Mn,Fe)_5$ [1, 4]. Zhang et al. [38] predicted that the $Al_8(Mn,Fe)_5$ intermetallic compound has the lowest efficiency as a nucleant for Mg grains based on E2EM model calculation. In addition, Wang et al. [104] investigated that Al_8Mn_5 intermetallic particles can be *in-situ* formed within the AZ91D alloys with different Mn addition. Their extensive TEM examinations on the Al_8Mn_5/α-Mg interfaces revealed that there is no crystallographic orientation relationship between the

Al_8Mn_5 and α-Mg crystals. Therefore, they concluded that Al_8Mn_5 particles are unlikely to act as effective nucleants for the α-Mg grains during solidification. In the present study, when small amount of Al addition was added into Mg-3Zn-0.3SiC alloy system, part of the Al captured the Mn (Fe) elements that originated from commercial purity Mg source to form $Al_8(Mn,Fe)_5$. This prevents the contact between Mn (Fe) elements and SiC inoculants, leading to the disappearance of the grain refining effect. Another part of the Al was served as normal solute element that segregates at the grain boundaries as shown in Fig. 5-24. Therefore, although 0.030% Mn and 0.007% Fe in commercial purity Mg source (see in Table 5-1) can consume only about 0.029% Al according to the reaction of $8Al + 5Mn(Fe) = Al_8(Mn,Fe)_5$, overdose of Al about 0.05 ~ 0.1% was needed to cause the grain coarsening effect.

It should be also noted that some previous researches also reported that Mn is a grain refiner for Mg-Al alloy system [18, 36, 101, 153], but the grain refining mechanisms are attributed to the formation of ε-AlMn or τ-AlMn phase in the Mn-Al alloys, not the Al_8Mn_5 phase. Furthermore, Cao et al. [101] verified that different Mn-containing sources would lead to different grain refining effects. However, no such phases were detected in the present study. Therefore, the grain coarsening effect is most likely attributed to a decrease in nucleation potency when effective Fe-Mn-Si intermetallic phase transformed to lower potent $Al_8(Mn,Fe)_5$ intermetallic phase.

No other new phases, such as Al_4C_3, Al_2CO and Al_2MgC_2, were observed in those alloys with further Al addition. In addition, if such potent nucleants can be formed *in-situ*, the grain refining effect would be significant. Therefore, the slightly decreasing grain refining effect with further Al addition could be only caused by the solute effect of Al, which has a similar Q value with that of Zn.

6.2.4 Different grain refinement behavior between graphite (C) and SiC

Comparing the grain refining effect of SiC inoculation in Mg-3Zn alloy with that of C inoculation, it clearly found that the grain refining effect of C is inferior to that of SiC. Previous research also concluded that the segregation of carbon has no much relationship for the grain refinement in Mg alloys by carbon inoculation, because the solubility of carbon in molten Mg alloys is only around 20 ppm [115]. The changes in average grain size of Mg-3Zn

alloy with different contents of SiC or C inoculants are shown in Fig. 6-10. The average grain size slightly decreases with the increase of C addition in Mg-3Zn alloy, even up to 10%. This indicates that the heterogeneous nucleation process with C is the main contribution to the grain refining effect. The greater the number of C particles, the greater is the probability of the preferred nucleation orientation and hence greater is the refining capability with higher amount of C addition. It should be also noted that the increasing number of nuclei or preferred nucleation orientation in Mg-3Zn-C system is limited due to the poor grain refining effect. However, the average grain size sharply decreases when the SiC addition changed from 0 to 0.3% in Mg-3Zn alloy. After that, the average grain size maintains at a stable level. This is because the reaction happens between SiC and impurities. The addition of SiC leads to not only the increase of number of nuclei, but the potency, which is discussed in Fig. 6-6. No further new nucleation sites can be formed by increasing SiC addition because the contents of impurities are limited. Therefore, the grain refining effect keeps stable.

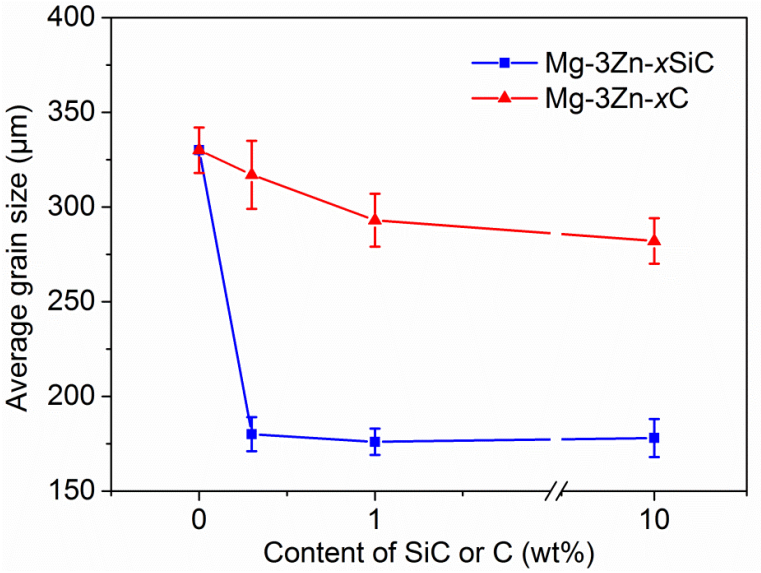

Fig. 6-10 Changes in average grain size of Mg-3Zn alloy with different contents of SiC or C inoculants

The maximum particle size of the remaining particles in Mg-3Zn melt can be predicted based on Eq. 6-2 with respect to different determined settling lengths. Note that the density of C is about 2.20 g•cm^{-3} [154], which is higher than that of Mg-3Zn melt (1.61 g•cm^{-3}, calculated based on Eq. 6-3) at 700 °C. Therefore, the settling behavior of C will happen in the melt. Fig. 6-11 shows an overview of a casting sample with the length of 120 mm. In general, the average length of a casting sample is around 100 ~ 140 mm based on our casting procedures.

As metallographic specimens were transversally sectioned from the position of 20 mm away from the bottom of each ingot, the determined settling lengths for calculation analysis can be set as 80 ~ 120 mm.

Fig. 6-11 Overview of a casting sample

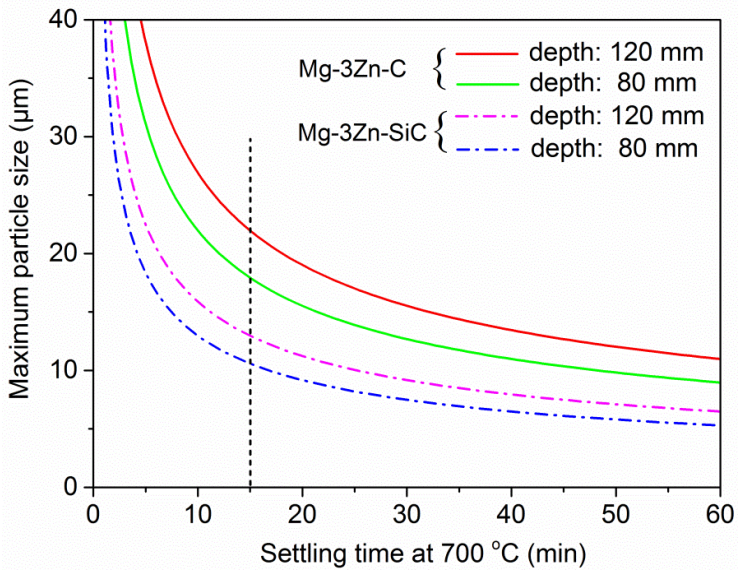

Fig. 6-12 Predicted maximum particle size against settling time at 700 °C for different depths of Mg-3Zn-C or Mg-3Zn-SiC system

Fig. 6-12 shows the predicted maximum particle size against settling time at 700 °C for different inoculation system with the settling depths varied from 80 to 120 mm. Regardless of the determined melt depth and also the inoculation system, the settling of undissolved SiC or C particles mainly occurs within the first 10 ~ 20 min. After that, the settling gradually

continues with increasing time until it reaches a relatively stabilized stage. Note that the bigger the particle size, the shorter is its finished settling time with a certain melt depth. Considering the settling time of 15 min, i.e. it equals to the holding time during casting, the particle size of C higher than ~18 μm under the melt depth of 80 mm (green line) will be totally settled down. For the melt depth of 120 mm (red line), the maximum particle size of the remaining C particles should be smaller than ~22 μm at 15 min. As the average particle size of C inoculation is around 20 μm, most of the C particles will be settled down during the casting process. Therefore, no C can be detected in Fig. 5-28(b) and Fig. 5-28(c) and Fig. 5-28(d), and the possible heterogeneous nuclei of C are rare, leading to the lower efficiency of grain refinement.

6.2.5 Comparisons of Mg-3Zn-0.3SiC, Mg-3Al-0.3SiC and Mg-3Zn-0.3Zr

Fig. 6-13 shows the comparisons of average grain size and the corresponding reduction percentage of average grain size for different alloy systems.

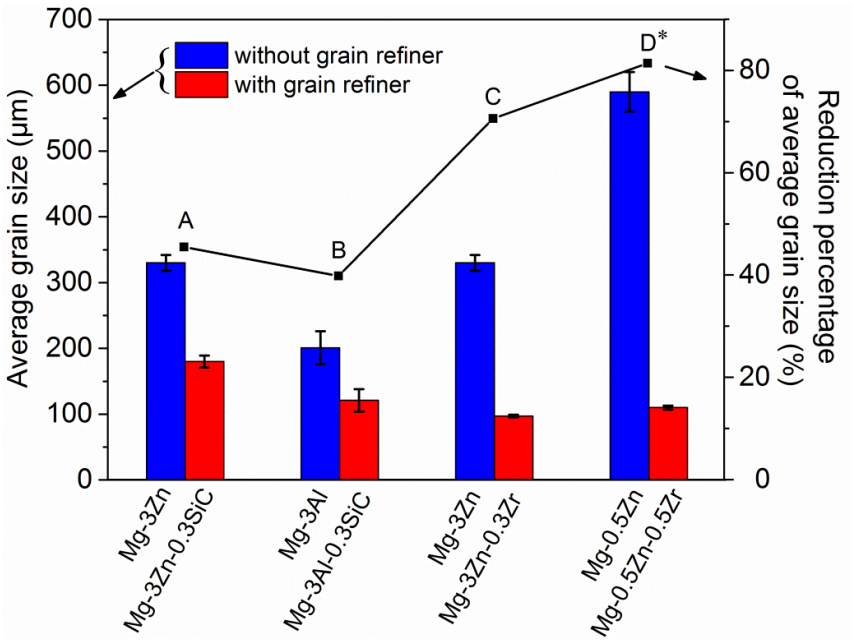

Fig. 6-13 Comparisons of average grain size and the corresponding reduction percentage of average grain size for different alloy systems. Data marked by group D were extracted from [4]*

Considering the same contents of solutes, i.e. 3%, in Mg-Zn and Mg-Al system with or without 0.3% SiC grain refiner, the average grain sizes of Mg-Al system with or without grain

refiner are much smaller than that of Mg-Zn system. However, the RP of average grain size for Mg-Zn system (point A) is 45%, which is higher than that of Mg-Al system (40%, point B). This means that the grain refining efficiency of 0.3% SiC is more effective in Mg-Zn system. The RP of grain size for Mg-Zn system with Zr inoculation is the most obvious one in both lower (0.5%) and higher (3%) contents of Zn. However, it should be noted that Zr is only effective for grain refinement in alloy systems without the alloying elements of Al, Mn, Si, and Fe, because Zr forms stable intermetallic compounds with these elements [81]. This indicates that Zr will totally lose the grain refining efficiency when it meets those alloying elements, which inhibits the usage range of Zr especially in very common Al-bearing Mg alloy systems. Instead, there is no limitation of grain refining effect of SiC for encountering the alloying elements of Al, Mn, Si, and Fe. In addition, the price of SiC particle is much cheaper than that of Zr. Furthermore, Zr is hard to be dissolved into Mg alloys and also it is easy to be settled down due to its high density [4, 11, 12]. Therefore, the SiC particle can be selected as a good grain refiner in both Al-bearing and Al-free Mg alloys with reasonable grain refining effect.

6.3 Grain refinement of Mg-Mn alloys by SiC inoculation

6.3.1 Effects of Mn contents

Based on Eq. 6-1, the RP of average grain size of Mg-*x*Mn alloys prior to and after the addition of 0.3% SiC particle inoculants is shown in Fig. 6-14. It clearly shows that the value of RP of grain size varies within a narrow range between 4.3% and 7.2%. No inferior grain refining effect obtains at high Mn solute compositions with 0.3% SiC addition, which can be also seen directly in Fig. 5-34, indicating that no capillary effect was occurred in Mg-*x*Mn-0.3SiC alloy system. This could be attributed to the very low Q value of Mn solute (Table 2-1) compared to that of Zn, leading to the grain growth mechanisms keep staying in the region 1 and 2 (Fig. 6-5). The grain morphologies in Fig. 5-31 and Fig. 5-34 match the predictive results in Fig. 6-5 very well.

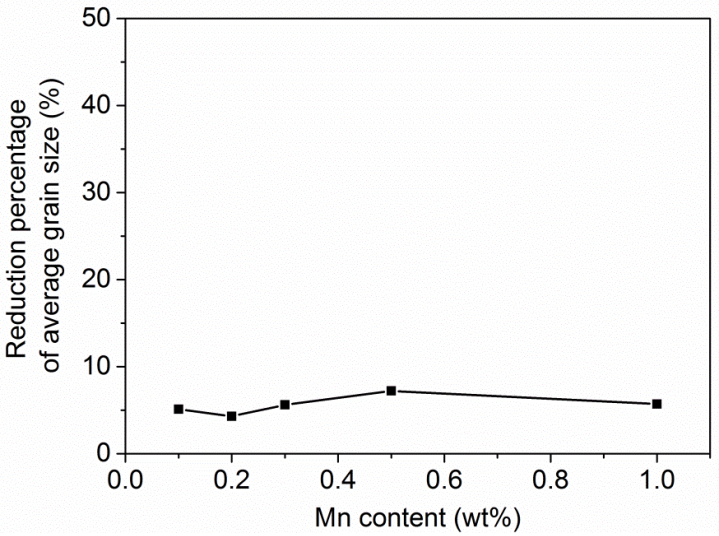

Fig. 6-14 Reduction percentage of grain size with different Mn content in Mg-xMn-0.3SiC alloy system

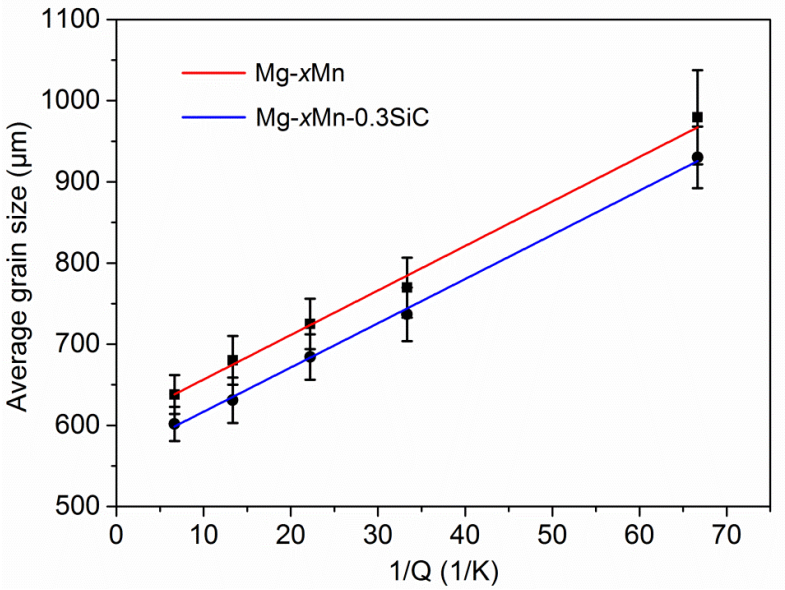

Fig. 6-15 The average grain sizes plotted against 1/Q for Mg-xMn and Mg-xMn-0.3SiC alloy system

Table 6-4 Intercept a, slope b and R^2 values for linear fittings in Fig. 6-15

Alloy system	Intercept *a* (μm)	Slope *b* (μm•*K*)	R^2
Mg-*x*Mn	601.68	5.48	0.99
Mg-*x*Mn-0.3SiC	562.27	5.44	0.99

Fig. 6-15 shows the average grain size resulting from Mg-*x*Mn and Mg-*x*Mn-0.3SiC alloys plotted against 1/*Q* based on the interdependence theory and fitted with Eq. 2-8. The

corresponding values of the intercept a, the slope b and the correlation coefficient R^2 were summarized in Table 6-4. The resulting average grain size shows a clear linear relationship with $1/Q$ for both alloy system. When 0.3% SiC was added into Mg-xMn alloy system, the value of intercept a decreases but the slope b keeps stable. The increasing value of a indicates that the addition of SiC leads to the increase of the activated nucleation sites. The almost same value of b reflects directly in the two parallel fitted lines, which suggests the iso-potency for nucleant sites in those two systems. As discussed in section 6.1, the potency of the nucleant particles presented in Mg-Mn binary system is much higher than those in Mg-Zn binary system. Therefore, although the potent nuclei can be formed by the following reaction:

$$3Mn + SiC = Mn_3Si + C \qquad 6\text{-}8$$

the potency level does not change too much due to the originally high potency level in Mg-Mn system. Another possible reason is that although the potency of Mn_3Si is higher than that of *in-situ* formed nuclei in binary Mg-Mn alloys, lots of those nuclei cannot be triggered effectively due to the very low segregation ability of Mn. This also means that the CS driving-force arising from solute segregation of Mn in front of the S-L interface is not enough to stimulate the nucleation process. Therefore, the grain refining effect in Mg-xMn-0.3SiC alloy system is moderate.

6.3.2 The role of SiC in Mg-Mn system

6.3.2.1 SiC addition amount

Considering the reaction Eq. 6-8 in section 6.3.1, 1% Mn can consume about 0.24% SiC. That is why some SiC clusters can be detected when the contents of SiC are ≥ 0.3% in Fig. 5-39. If the SiC contents are ≤ 0.2%, they could totally react with Mn solute and therefore no SiC clusters were observed. When increasing the SiC content up to 5%, the aggregation of SiC particle is severe and it can be even detected by XRD in Fig. 5-40. SiC contents varied from 0.5% to 1.0% are the optimized addition amount for the grain refinement of Mg-1Mn alloys, as shown in Fig. 5-38. In general, a reasonable overdose of SiC addition amount ensures the adequate reaction process between SiC and Mn solute.

6.3.2.2 The particle size of SiC

Generally, the dissolution rate of smaller SiC particles in the melt should be higher compared to bigger SiC particles. However, stirring conditions counteract that effect by easier cluster formation for the smaller particles. The SiC clusters that found in Mg-1Mn-0.5SiC (0.1~1 μm) system are similar to the situation in Mg-3Zn alloy inoculated with 0.1~1 μm SiC. Both of them suggest that sub-micrometer SiC particles are easy to aggregate together, which will interfere with the grain refining process. In contrast, the number density of SiC particle is the lowest for 10 μm SiC inoculants. Those SiC particles can be easily separated and then uniformly distributes in the melt. In addition, the content level of Mn in Mg-1Mn system is much higher than that in Mg-3Zn system. Therefore, these SiC particles can be captured by Mn and then react with Mn in the melt to form nucleation sites that uniformly suspend in the melt. Consequently, the grain refining effect of Mg-1Mn-0.5SiC (10 μm) system is better than that of Mg-1Mn-0.5SiC (0.1~1 μm) system, as shown in Fig. 5-42.

6.3.2.3 The addition temperature

Interestingly, different addition temperature leads to totally different grain refining effect in Mg-1Mn and Mg-3Zn systems with SiC inoculation. For Mg-1Mn-0.5SiC system, it favors high addition temperature of SiC. However, Mg-3Zn-0.3SiC system favors low addition temperature. First, it could be due to the different inherent physical properties between Mn element and Zn element. Especially, the melt point of Mn is about 1246 ºC, but the melt point of Zn is only about 419.5 ºC. In addition, the effective nucleation sites resulted from the reaction between the SiC and Mn in the melt is based on Eq. 6-8. This is an endothermic reaction and its operation will become more active as the temperature increases, resulting in the formation of more Mn_3Si nucleation sites. Abundant amount of Mn and SiC in Mg-1Mn-0.5SiC system can support this process well. Those new and fresh formed nuclei may compensate the inoculation fading phenomenon, leading to the better grain refining effect in Mg-1Mn-0.5SiC system at higher addition temperature.

6.3.2.4 The holding time

Unlike the results in Mg-3Zn-0.3SiC system with different holding time, the long holding

time improves the grain refining efficiency during the inoculation process of 0.5% SiC in Mg-1Mn alloys, which means that the common inoculation fading phenomenon do not happen. The possible reason could be related to the above discussion in 6.3.2.3. As the amount of Mn and SiC is abundant, long holding time leads to enough time for the reaction between SiC and Mn, and also the possibility for new reaction increases. In addition, no SiC clusters can be detected in Mg-1Mn-0.5SiC system even after 60 min settling, suggesting that the reaction between Mn and the suspended SiC is completed. Therefore, the current result implies that the sensitivity of the used grain refiner (SiC) to inoculation fading is relatively high and the longest holding time can exceed around 60 min.

6.3.3 The formation of Mn_3Si nuclei

Although the normal Scheil solidification simulation in section 5.2.5 indicates that Mn_3Si can be formed only when the content of Mn is higher than 1.34%, Mn_3Si nuclei were observed and verified in Mg-1Mn-0.3SiC alloy system in section 5.2.4. This deviation could be originated from a local imbalance of Mn composition in the melt. Laser et al. [102] also proposed that the SEM observation of β-Mn phase in AZ31 alloy system with 0.28% Mn addition cannot be explained by both the phase diagram and the solidification simulation result, which is attributed to the local imbalance of Mn composition in the melt. Similar result of Liu et al. [155] verified that $MgZn_2$ phase formed prior to the nucleation of Zn grains due to the inhomogeneity of Mg concentration even though $MgZn_2$ would not form in the binary Zn-Mg alloys containing less than 6.3% Mg. In addition, the nucleation barriers for precipitation during solidification are not considered within the Scheil model. Indeed, nucleation barriers related to the interfacial energies between two different phases can be huge. This would result in a shift of the formation temperature of the second phase, or even a change of the formation sequence.

In fact, the calculated equilibria among the remaining set of phases by suspending the Mn_5Si_3 phase result in the constrained Scheil solidification simulations (Fig. 6-16). This simulates some undercooling to the “next stable” Mn_3Si phase. The corresponding formation temperature of Mn_5Si_3, Mn_3Si and α-Mg phases in both normal Scheil and constrained Scheil conditions were summarized in Table 6-5.

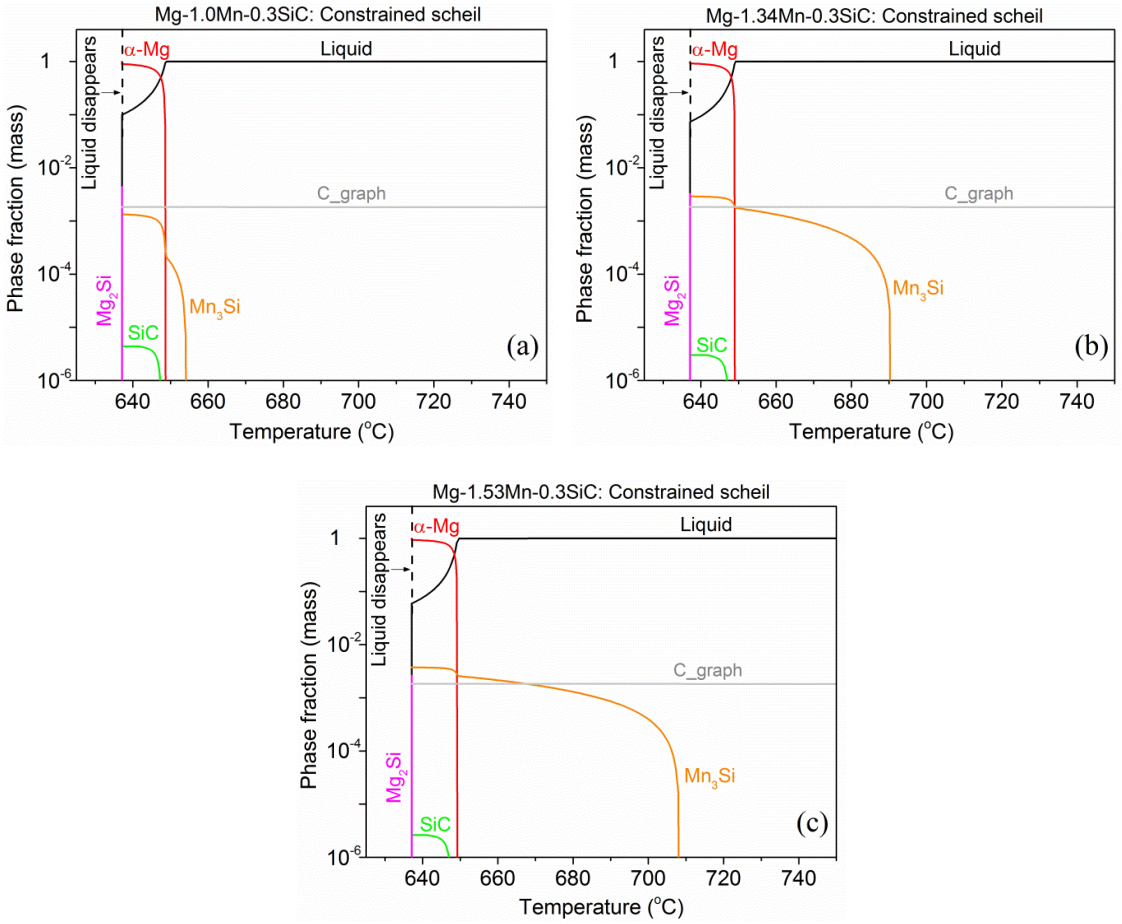

Fig. 6-16 Mass fraction of the second phases calculated for rapid solidification under constrained Scheil conditions (Mn_5Si_3 phase suspended) vs. temperature for Mg-xMn-0.3SiC alloy system: (a) Mg-1.0Mn-0.3SiC; (b) Mg-1.34Mn-0.3SiC; (c) Mg-1.53Mn-0.3SiC

Table 6-5 Formation temperature of Mn_5Si_3, Mn_3Si and α-Mg phases by using normal Scheil and constrained Scheil solidification simulations

Alloy system	Mn_5Si_3 formed temperature (°C)	Mn_3Si formed temperature (°C)	α-Mg formed temperature (°C)
Mg-1.0Mn-0.3SiC-normal	664.93	–	648.77
Mg-1.0Mn-0.3SiC-constrained	–	654.05	648.61
Mg-1.34Mn-0.3SiC-normal	694.05	649.25	649.17
Mg-1.34Mn-0.3SiC-constrained	–	690.21	648.93
Mg-1.53Mn-0.3SiC-normal	686.83	707.95	649.23
Mg-1.53Mn-0.3SiC-constrained	–	707.95	649.07

For the three constrained Scheil solidification simulations, the Mn_3Si is the only preferred Mn-Si phase type formed prior to the formation of α-Mg phase. Although Mn_3Si was not found in Mg-1.0Mn-0.3SiC alloy system by using normal Scheil condition (Fig. 5-55(b)), Mn_3Si could thoroughly substitute the Mn_5Si_3 phase formed prior to α-Mg served as the nucleus by using constrained Scheil condition (Fig. 6-16(a)). This supports the results of FIB and TEM analyses in section 5.2.4 very well. In addition, based on the Table 6-5, the predicted undercoolings of Mn_3Si to that of Mn_5Si_3 in the same alloy system by using both normal Scheil and constrained Scheil conditions are 10.88 °C (Mg-1.0Mn-0.3SiC system), 3.84 °C (Mg-1.34Mn-0.3SiC system), 0 °C (Mg-1.53Mn-0.3SiC system), respectively. The degree of the predicted undercooling decreased with increasing Mn content. It decreased to 0 as Mn_3Si phase is already formed prior to the formation of Mn_5Si_3 phase in Mg-1.53Mn-0.3SiC system, even by using the normal Scheil condition (Fig. 5-55(d)). Note that C_graph originated from SiC particle always precipitated as the first solid phase prior to the formation of α-Mg phase in both normal Scheil and constrained Scheil solidification simulations. However, the results in section 5.1.6 and section 6.2.4 show that the contribution of graphite to grain refinement effect is very limited. Based on the above discussions, it can be confirmed that Mn_3Si is the actual nucleation site for Mg-Mn-SiC alloy system in the present work, leading to the grain refinement effect. Till now, the Fe-Mn-Si rich intermetallic phase detected in Mg-Zn-SiC system can be also revised in the form of $(Mn,Fe)_3Si$ phase.

6.3.4 The influence of impurity element Fe

As Fe always appears together with Mn or substitutes the Mn to react with SiC to form the nucleants in Mg-Zn-SiC alloy system, the function of Fe in Mg-Mn-SiC alloy system should also be considered. However, it should be noted that the Mn addition is deliberately added into Mg-Mn-SiC alloy system, the Mn content is much higher than that of Fe (impurity level). Therefore, the formation of Mn_3Si nuclei is the common phenomenon. Fig. 6-17 shows a detailed BSE characterization of a nucleus with the appearance of Fe.

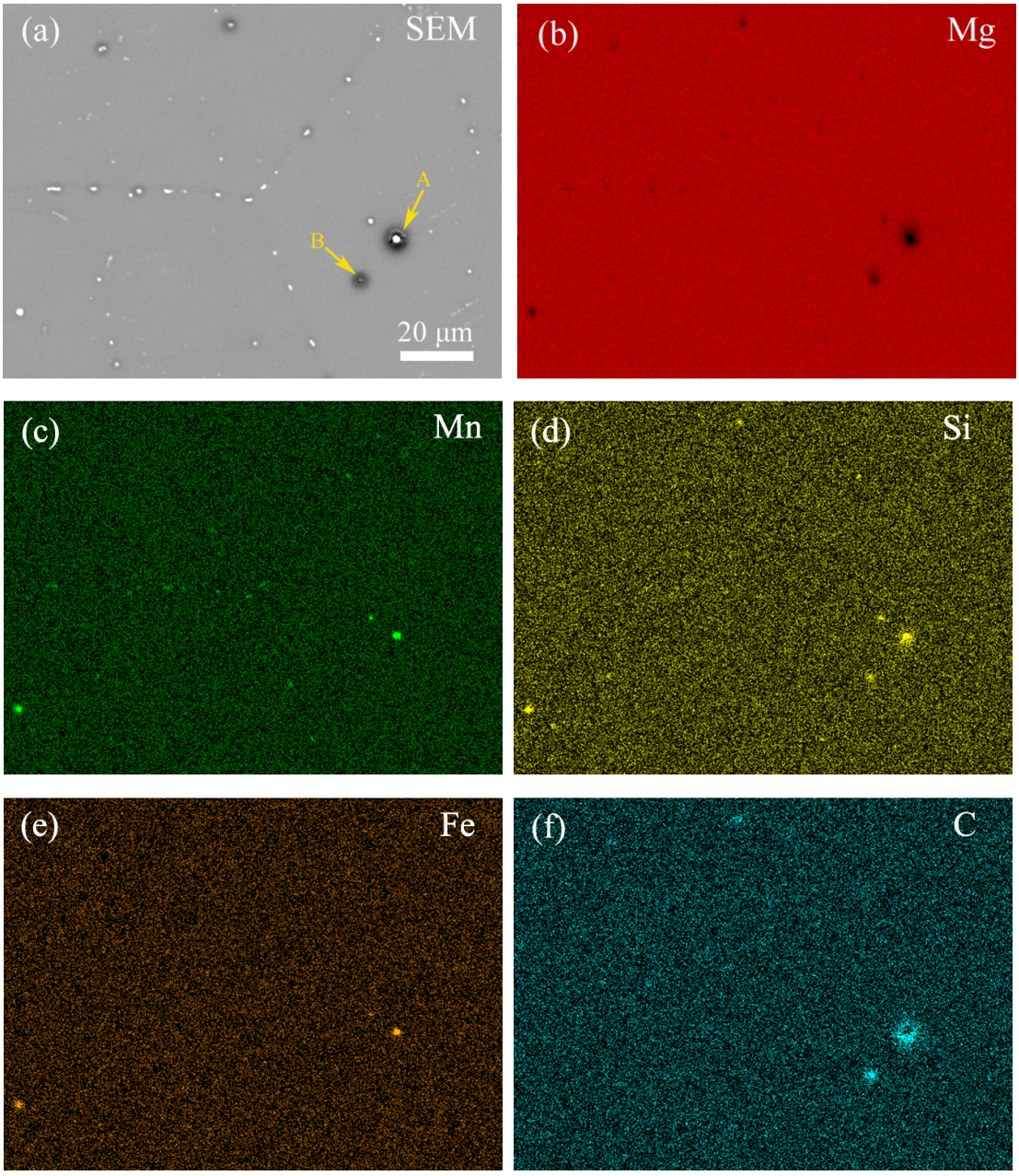

Fig. 6-17 BSE image and corresponding EDS mappings of Mg-1Mn-0.3SiC alloy

The region A marked with yellow arrow in Fig. 6-17(a) indicates a nucleus enriched with Mn, Fe, Si and C elements, which means that Fe is possible to substitute the element Mn in some extend, to react with SiC to form the potent nucleus. In this case, the Mn_3Si phase can be rewritten as $(Mn,Fe)_3Si$ phase. The region B marked with yellow arrow was verified as an unreacted SiC particle, because only Si and C elements were detected. This situation could occur when some of the SiC particle cannot capture the Mn or Fe element. It also supports the similar result obtained in Mg-3Zn-10SiC alloy system, see in Fig. 5-20(b) and (d).

In summary, the effect of SiC inoculation on grain refinement of the as-cast Mg-Mn binary alloys can be well understood according to the interdependency theory [3]. After inoculation, part of SiC particles can react with Mn and/or Fe atoms to form *in-situ* potent Mn_3Si or $(Mn,Fe)_3Si$ nuclei, which not only promotes heterogeneous nucleation at beginning of the solidification, but also restricts the grain growth through continuing nucleation within the CS zone at front of the S-L interface. However, as the formation of CS zone depending on the solute segregation at the front of the S-L interface, the solute element Mn with relatively low Q value has little contribution to the formation of the CS zone. Thus, the grain refining efficiency is moderate in Mg-Mn-SiC alloy system compared with that of Mg-Zn-SiC alloy system, because Zn with high Q value can provide additional undercooling to activate and accelerate the heterogeneous nucleation process. The present work indicates that chemical reactions in the melt should be considered and paid attention to during inoculation process. The co-existence of potent nucleants and solutes with high Q values is necessary to obtain the highest grain refining efficiency.

7 Summary

The grain refinement efficiencies of as-cast binary Mg-Zn and Mg-Mn alloys with SiC inoculation were systematically investigated. The interaction between SiC and solute/impurity elements on grain refinement was clarified. The grain refinement mechanisms are also discussed. The conclusions are summarized as follows:

1. SiC particle can be selected as a good grain refiner in both Al-free and Al-bearing Mg alloys with reasonable grain refining effect. It has a wider range of applications in practice even encountering Al, Mn, Si and Fe compared to that of Zr. The grain refining efficiency of graphite (C) is inferior to that of SiC, because most of the C particles of 20 μm are settled down during the casting process, and also no chemical reaction occurs between C and solute/impurity elements.

2. Comparing with the SiC particles with the size of 0.1~1 μm or 10 μm, SiC particles with the size of 2 μm are the most effective grain refining agents in both as-cast binary Mg-Zn and Mg-Mn alloys. For the grain refinement of Mg-Zn alloy system, SiC contents varied from 0.3% to 0.5% are the optimized addition amount, and the addition temperature controlled at 700 ~ 720 ^{o}C and the holding time maintained at 0 ~ 15 min are preferred. For the grain refinement of Mg-Mn alloy system, SiC contents varied from 0.5% to 1.0% are the optimized parameters, and the preferred addition temperature and holding time are 740 ~ 760 ^{o}C and 30 ~ 60 min, respectively.

3. The grain size of Mg-3Zn-0.3SiC alloy system is dramatically coarsened when the addition of Al is less than 0.1%, but decreased gradually by adding more Al up to 1%. The poisoning effect of small amount addition of Al is due to the formation of low potent $Al_8(Mn,Fe)_5$ phase, which interferes with the reaction between SiC and Mn (or Fe) to form potent nuclei. The comparative test of high purity (HP) Mg-3Zn-0.3SiC-0.1Al alloy with no poisoning grain refinement effect supports this result well. The grain refinement effect observed with further Al addition is caused by the solute effect of Al.

4. The solidification process of Mg-Mn-SiC alloy system by Pandat software simulation

supports that Mn_3Si phase can be formed prior to the nucleation of α-Mg grains. The contents of Mn affect the phase precipitating sequence in Mg-Mn-SiC alloy system based on the simulation results. Due to the imbalance of Mn composition in the melt, it was experimentally evidenced that Mn_3Si particles formed and served as the nucleation sites even though such phase would not appear when Mn content is less than 1.34%.

5. The added SiC particles cannot directly act as nucleation sites of α-Mg grains. The Mn_3Si or $(Mn,Fe)_3Si$ nuclei *in-situ* formed by the reaction between the SiC particles and Mn (or Fe), which depends on whether Fe atoms can substitute some of the Mn atoms during reaction. The preferred orientation relationship (OR) between the nuclei and Mg matrix follows the rule of $\Delta\mathbf{g}$ parallel to $\mathbf{g}$, and the measured OR obeys the following relationship: $\mathbf{g}_{(0\ 1\ \bar{1}\ 0)Mg} // \Delta\mathbf{g_1} // \Delta\mathbf{g_2}$, where $\Delta\mathbf{g_1} = \mathbf{g}_{(\bar{1}\ 1\ 0\ 1)Mg} - \mathbf{g}_{(\bar{2}\ 0\ 0)Mn3Si}$, $\Delta\mathbf{g_2} = \mathbf{g}_{(\bar{1}\ 0\ 1\ 1)Mg} - \mathbf{g}_{(\bar{2}\ 0\ 0)Mn3Si}$.

6. The grain refining efficiency of SiC inoculation is not only dominated by the presence of *in-situ* formed heterogeneous nucleation sites, but also by the solute element of Mn or Zn. The co-existence of potent nucleants and solutes with high Q values is necessary to obtain the highest grain refining efficiency. This is also correct in binary Mg-Zn and Mg-Mn alloy systems. The constitutional supercooling (CS) driving-force arising from solute segregation in front of the S-L interface is even more important and necessary when an effective nucleant is presented in the melt than without.

Outlook:

- This thesis found that the co-existence of potent nucleants and solutes with high segregation ability is necessary to obtain good grain refining efficiency. The complex interaction between them needs to be checked in-depth.
- A standard quantitative evaluation system of grain refinement efficiency needs to be established and developed, which can be applicable to all casting alloys and types.
- Future work should improve the understanding of grain refinement mechanisms. It is an interesting topic to investigate the heterogeneous nucleation at atomic level.
- New techniques (i.e. *in-situ* synchrotron diffraction) should be introduced in the investigation of microstructure evolution during solidification.

8 Acknowledgements

I sincerely acknowledge the financial support from the China Scholarship Council (CSC).

Many thanks to my supervisor Prof. Dr.-Ing. (a.D.) Rainer Schmid-Fetzer for all of his help and guidance. I also gratefully thank Prof. Dr.-Ing. Karl Ulrich Kainer for his agreement to be the chief reviewer of this work and his valuable suggestions to complete this study.

I sincerely thank Dr. Norbert Hort and Dr. Yuanding Huang for their scientific and fruitful discussions during this work. I learned a lot from the discussions on grain refinement of magnesium alloys.

Many thanks also to Dr. Li Wang and Dr. Henry Ovri for their helps in experiments, results analysis, and valuable discussions. Moreover, preparation of raw materials with the help from Dr. Hajo Dieringa is also greatly acknowledged.

Many thanks to Mr. Günter Meister, Mr. Gert Wiese, Ms. Petra Fischer and Ms. Sabine Schubert for their excellent technical help. I also thank all the staffs in WZP group for their help and support.

Finally, I would like to thank my family for their encouragement and support, especially my wife, Sasa Gu.

9 References

[1] D.H. StJohn, M.A. Easton, M. Qian, J.A. Taylor, Grain Refinement of Magnesium Alloys: A Review of Recent Research, Theoretical Developments, and Their Application, Metallurgical and Materials Transactions A, 44 (2012) 2935-2949.

[2] M.A. Easton, M. Qian, A. Prasad, D.H. StJohn, Recent advances in grain refinement of light metals and alloys, Current Opinion in Solid State and Materials Science, 20 (2016) 13-24.

[3] D.H. StJohn, M. Qian, M.A. Easton, P. Cao, The Interdependence Theory: The relationship between grain formation and nucleant selection, Acta Materialia, 59 (2011) 4907-4921.

[4] D.H. StJohn, M. Qian, M.A. Easton, P. Cao, Z. Hildebrand, Grain refinement of magnesium alloys, Metallurgical and Materials Transactions A, 36 (2005) 1669-1679.

[5] H.W. Chang, D. Qiu, J.A. Taylor, M.A. Easton, M.X. Zhang, The role of Al_2Y in grain refinement in Mg–Al–Y alloy system, Journal of Magnesium and Alloys, 1 (2013) 115-121.

[6] D. Qiu, M.X. Zhang, P.M. Kelly, Crystallography of heterogeneous nucleation of Mg grains on Al_2Y nucleation particles in an Mg–10wt.% Y alloy, Scripta Materialia, 61 (2009) 312-315.

[7] H.M. Fu, M.X. Zhang, D. Qiu, P.M. Kelly, J.A. Taylor, Grain refinement by AlN particles in Mg–Al based alloys, Journal of Alloys and Compounds, 478 (2009) 809-812.

[8] B. Jiang, W. Liu, D. Qiu, M.X. Zhang, F. Pan, Grain refinement of Ca addition in a twin-roll-cast Mg–3Al–1Zn alloy, Materials Chemistry and Physics, 133 (2012) 611-616.

[9] Y. Ali, D. Qiu, B. Jiang, F. Pan, M.X. Zhang, The influence of CaO addition on grain refinement of cast magnesium alloys, Scripta Materialia, 114 (2016) 103-107.

[10] J. Jeong, J. Im, K. Song, M. Kwon, S.K. Kim, Y. Kang, S.H. Oh, Transmission electron microscopy and thermodynamic studies of CaO-added AZ31 Mg alloys, Acta Materialia, 61 (2013) 3267-3277.

[11] M. Qian, L. Zheng, D. Graham, M.T. Frost, D.H. StJohn, Settling of undissolved zirconium particles in pure magnesium melts, Journal of Light Metals, 1 (2001) 157-165.

[12] M. Qian, A. Das, Grain refinement of magnesium alloys by zirconium: Formation of

equiaxed grains, Scripta materialia, 54 (2006) 881-886.

[13] M.A. Easton, A. Schiffl, J.Y. Yao, H. Kaufmann, Grain refinement of Mg–Al(–Mn) alloys by SiC additions, Scripta Materialia, 55 (2006) 379-382.

[14] Y. Huang, K.U. Kainer, N. Hort, Mechanism of grain refinement of Mg–Al alloys by SiC inoculation, Scripta Materialia, 64 (2011) 793-796.

[15] A. Schiffl, M. Easton, Influence of SiC particles on the grain refinement of an Mg-Al alloy, Materials Science Forum, 618 (2009) 445-448.

[16] G. Cao, H. Choi, H. Konishi, S. Kou, R. Lakes, X. Li, Mg–6Zn/1.5%SiC nanocomposites fabricated by ultrasonic cavitation-based solidification processing, Journal of Materials Science, 43 (2008) 5521-5526.

[17] G. Cao, J. Kobliska, H. Konishi, X. Li, Tensile properties and microstructure of SiC nanoparticle-reinforced Mg-4Zn alloy fabricated by ultrasonic cavitation-based solidification processing, Metallurgical and Materials Transactions A, 39 (2008) 880-886.

[18] J. Du, J. Yang, M. Kuwabara, W. Li, J. Peng, Effects of manganese and/or carbon on the grain refinement of Mg-3Al alloy, Materials transactions, 49 (2008) 139-143.

[19] A. Zhang, H. Hao, X. Zhang, Grain refinement mechanism of Al-5C master alloy in AZ31 magnesium alloy, Transactions of Nonferrous Metals Society of China, 23 (2013) 3167-3172.

[20] S. Liu, Y. Zhang, H. Han, Role of manganese on the grain refining efficiency of AZ91D magnesium alloy refined by Al_4C_3, Journal of Alloys and Compounds, 491 (2010) 325-329.

[21] E.F. Horst, B. Mordike, Magnesium technology. Metallurgy, design data, application, Springer-Verlag, Berlin Heidelberg, Germany, 2006.

[22] D. Turnbull, B. Vonnegut, Nucleation catalysis, Industrial & Engineering Chemistry, 44 (1952) 1292-1298.

[23] B.L. Bramfitt, The effect of carbide and nitride additions on the heterogeneous nucleation behavior of liquid iron, Metallurgical Transactions, 1 (1970) 1987-1995.

[24] P.M. Kelly, M.X. Zhang, Edge-to-edge matching - a new approach to the morphology and crystallography of precipitates, Materials Forum, 23 (1999) 41-62.

[25] Z. Fan, An epitaxial model for heterogeneous nucleation on potent substrates, Metallurgical and Materials Transactions A, 44 (2012) 1409-1418.

[26] A. Greer, A. Bunn, A. Tronche, P. Evans, D. Bristow, Modelling of inoculation of metallic melts: application to grain refinement of aluminium by Al–Ti–B, Acta Materialia, 48 (2000) 2823-2835.

[27] Y. Ali, D. Qiu, B. Jiang, F. Pan, M.X. Zhang, Current research progress in grain refinement of cast magnesium alloys: A review article, Journal of Alloys and Compounds, 619 (2015) 639-651.

[28] L. Lu, A.K. Dahle, D.H. StJohn, Grain refinement efficiency and mechanism of aluminium carbide in Mg–Al alloys, Scripta Materialia, 53 (2005) 517-522.

[29] Y. Wang, X. Zeng, W. Ding, Effect of Al–4Ti–5B master alloy on the grain refinement of AZ31 magnesium alloy, Scripta Materialia, 54 (2006) 269-273.

[30] S. Liu, Y. Zhang, H. Han, B. Li, Effect of Mg–TiB_2 master alloy on the grain refinement of AZ91D magnesium alloy, Journal of alloys and compounds, 487 (2009) 202-205.

[31] Y. Wang, Z. Fan, X. Zhou, G. Thompson, Characterisation of magnesium oxide and its interface with α-Mg in Mg–Al-based alloys, Philosophical Magazine Letters, 91 (2011) 516-529.

[32] M.X. Zhang, P.M. Kelly, Edge-to-edge matching and its applications: Part I. application to the simple hcp/bcc system, Acta Materialia, 53 (2005) 1073-1084.

[33] M.X. Zhang, P.M. Kelly, Edge-to-edge matching and its applications: part II. Application to Mg–Al, Mg–Y and Mg–Mn alloys, Acta materialia, 53 (2005) 1085-1096.

[34] P.M. Kelly, M.X. Zhang, Edge-to-edge matching-The fundamentals, Metallurgical and Materials Transactions A, 37 (2006) 833-839.

[35] D. Qiu, J.A. Taylor, M.X. Zhang, P.M. Kelly, A mechanism for the poisoning effect of silicon on the grain refinement of Al–Si alloys, Acta Materialia, 55 (2007) 1447-1456.

[36] D. Qiu, M.X. Zhang, J.A. Taylor, H.M. Fu, P.M. Kelly, A novel approach to the mechanism for the grain refining effect of melt superheating of Mg–Al alloys, Acta Materialia, 55 (2007) 1863-1871.

[37] D. Qiu, M.X. Zhang, H.M. Fu, P.M. Kelly, J.A. Taylor, Crystallography of recently developed grain refiners for Mg–Al alloys, Philosophical Magazine Letters, 87 (2007) 505-514.

[38] M.X. Zhang, P.M. Kelly, M. Qian, J.A. Taylor, Crystallography of grain refinement in

Mg–Al based alloys, Acta Materialia, 53 (2005) 3261-3270.

[39] M.X. Zhang, P.M. Kelly, M.A. Easton, J.A. Taylor, Crystallographic study of grain refinement in aluminum alloys using the edge-to-edge matching model, Acta Materialia, 53 (2005) 1427-1438.

[40] D. Qiu, M.X. Zhang, J.A. Taylor, P.M. Kelly, A new approach to designing a grain refiner for Mg casting alloys and its use in Mg–Y-based alloys, Acta Materialia, 57 (2009) 3052-3059.

[41] H.M. Fu, D. Qiu, M.X. Zhang, H. Wang, P.M. Kelly, J.A. Taylor, The development of a new grain refiner for magnesium alloys using the edge-to-edge model, Journal of Alloys and Compounds, 456 (2008) 390-394.

[42] D. Qiu, M.X. Zhang, P.M. Kelly, Crystallography of self-assembled $DySi_2$ nanowires on a Si substrate, Applied Physics Letters, 94 (2009) 0831051-0831053.

[43] W. Kim, B. Cantor, An adsorption model of the heterogeneous nucleation of solidification, Acta metallurgica et materialia, 42 (1994) 3115-3127.

[44] G.P. Jones, Grain refinement of castings using inoculants for nucleation above liquidus, Solidification Processing 1987, (1987) 496-499.

[45] G.P. Jones, J. Pearson, Factors affecting the grain-refinement of aluminum using titanium and boron additives, Metallurgical Transactions B, 7 (1976) 223-234.

[46] H. Men, Z. Fan, Atomic ordering in liquid aluminium induced by substrates with misfits, Computational Materials Science, 85 (2014) 1-7.

[47] P. Schumacher, A. Greer, Heterogeneously nucleated α-Al in amorphous aluminium alloys, Materials Science and Engineering: A, 178 (1994) 309-313.

[48] P. Schumacher, A. Greer, J. Worth, P. Evans, M. Kearns, P. Fisher, A. Green, New studies of nucleation mechanisms in aluminium alloys: implications for grain refinement practice, Materials science and technology, 14 (1998) 394-404.

[49] A.L. Greer, P.S. Cooper, M.W. Meredith, W. Schneider, P. Schumacher, J.A. Spittle, A. Tronche, Grain refinement of aluminium alloys by inoculation, Advanced Engineering Materials, 5 (2003) 81-91.

[50] N. Iqbal, N. Van Dijk, T. Hansen, L. Katgerman, G. Kearley, The role of solute titanium and TiB_2 particles in the liquid–solid phase transformation of aluminum alloys, Materials

Science and Engineering: A, 386 (2004) 20-26.

[51] J. Wang, A. Horsfield, U. Schwingenschlögl, P.D. Lee, Heterogeneous nucleation of solid Al from the melt by TiB_2 and Al_3Ti: An *ab initio* molecular dynamics study, Physical Review B, 82 (2010) 1-10.

[52] H. Zhang, Y. Han, W. Zhou, Y. Dai, J. Wang, B. Sun, Atomic study on the ordered structure in Al melts induced by liquid/substrate interface with Ti solute, Applied Physics Letters, 106 (2015) 1-5.

[53] Z. Fan, Y. Wang, Y. Zhang, T. Qin, X.R. Zhou, G.E. Thompson, T. Pennycook, T. Hashimoto, Grain refining mechanism in the Al/Al–Ti–B system, Acta Materialia, 84 (2015) 292-304.

[54] I. Maxwell, A. Hellawell, A simple model for grain refinement during solidification, Acta Metallurgica, 23 (1975) 229-237.

[55] A. Greer, Grain refinement of alloys by inoculation of melts, Philosophical Transactions of the Royal Society of London A: Mathematical, Physical and Engineering Sciences, 361 (2003) 479-495.

[56] N.H. Fletcher, Size effect in heterogeneous nucleation, The Journal of Chemical Physics, 29 (1958) 572-576.

[57] M. Qian, J. Ma, Heterogeneous nucleation on convex spherical substrate surfaces: A rigorous thermodynamic formulation of Fletcher's classical model and the new perspectives derived, The Journal of Chemical Physics, 130 (2009) 214709.

[58] M. Vandyoussefi, A. Greer, Application of cellular automaton–finite element model to the grain refinement of directionally solidified Al–4.15 wt% Mg alloys, Acta Materialia, 50 (2002) 1693-1705.

[59] M. Qian, Heterogeneous nuclei size in magnesium–zirconium alloys, Scripta Materialia, 50 (2004) 1115-1119.

[60] R. Günther, C. Hartig, R. Bormann, Grain refinement of AZ31 by $(SiC)_P$: Theoretical calculation and experiment, Acta Materialia, 54 (2006) 5591-5597.

[61] D. Qiu, M.X. Zhang, Effect of active heterogeneous nucleation particles on the grain refining efficiency in an Mg–10wt.% Y cast alloy, Journal of Alloys and Compounds, 488 (2009) 260-264.

[62] Y. Zhang, H. Zheng, Y. Liu, L. Shi, R. Xu, X. Tian, Cluster-assisted nucleation of silicon phase in hypoeutectic Al–Si alloy with further inoculation, Acta Materialia, 70 (2014) 162-173.

[63] M.A. Easton, D.H. StJohn, Grain refinement of aluminum alloys: Part I. The nucleant and solute paradigms - a review of the literature, Metallurgical and Materials Transactions A, 30 (1999) 1613-1623.

[64] M.A. Easton, D.H. StJohn, Grain refinement of aluminum alloys: Part II. Confirmation of, and a mechanism for, the solute paradigm, Metallurgical and Materials Transactions A, 30 (1999) 1625-1633.

[65] Y. Lee, A. Dahle, D.H. StJohn, The role of solute in grain refinement of magnesium, Metallurgical and Materials Transactions A, 31 (2000) 2895-2906.

[66] M.A. Easton, D.H. StJohn, A model of grain refinement incorporating alloy constitution and potency of heterogeneous nucleant particles, Acta Materialia, 49 (2001) 1867-1878.

[67] D.H. StJohn, A. Prasad, M.A. Easton, M. Qian, The contribution of constitutional supercooling to nucleation and grain formation, Metallurgical and Materials Transactions A, 46 (2015) 4868-4885.

[68] M. Johnsson, L. Backerud, G.K. Sigworth, Study of the mechanism of grain refinement of aluminum after additions of Ti-and B-containing master alloys, Metallurgical Transactions A, 24 (1993) 481-491.

[69] T. Quested, A. Dinsdale, A. Greer, Thermodynamic modelling of growth-restriction effects in aluminium alloys, Acta materialia, 53 (2005) 1323-1334.

[70] R. Schmid-Fetzer, A. Kozlov, Thermodynamic aspects of grain growth restriction in multicomponent alloy solidification, Acta Materialia, 59 (2011) 6133-6144.

[71] M. Sun, M.A. Easton, D.H. StJohn, G. Wu, T.B. Abbott, W. Ding, Grain refinement of magnesium alloys by Mg–Zr master alloys: the role of alloy chemistry and Zr particle number density, Advanced Engineering Materials, 15 (2013) 373-378.

[72] M.J. Bermingham, S.D. McDonald, M.S. Dargusch, D.H. StJohn, The mechanism of grain refinement of titanium by silicon, Scripta Materialia, 58 (2008) 1050-1053.

[73] M.J. Bermingham, S.D. McDonald, D.H. StJohn, M.S. Dargusch, Beryllium as a grain refiner in titanium alloys, Journal of Alloys and Compounds, 481 (2009) L20-L23.

[74] M.A. Easton, D.H. StJohn, An analysis of the relationship between grain size, solute content, and the potency and number density of nucleant particles, Metallurgical and materials transactions A, 36 (2005) 1911-1920.

[75] D.H. StJohn, P. Cao, M. Qian, M.A. Easton, A New Analytical Approach to Reveal the Mechanisms of Grain Refinement, Advanced Engineering Materials, 9 (2007) 739-746.

[76] M.A. Easton, D.H. StJohn, Improved prediction of the grain size of aluminum alloys that includes the effect of cooling rate, Materials Science and Engineering: A, 486 (2008) 8-13.

[77] J. Dai, M.A. Easton, M.X. Zhang, D. Qiu, X. Xiong, W. Liu, G. Wu, Effects of cooling rate and solute content on the grain refinement of Mg-Gd-Y alloys by aluminum, Metallurgical and Materials Transactions A, 45 (2014) 4665-4678.

[78] A. Banerji, Q. Feng, W. Reif, On identification of the nucleant in commercially pure aluminum castings inoculated with < 0.15 pct titanium, Metallurgical Transactions A, 20 (1989) 564-566.

[79] K. Honda, K. Ushioda, W. Yamada, K. Tanaka, H. Hatanaka, Nucleation of the primary Al phase on $TiAl_3$ during solidification in hot-dip Zn-11%Al-3%Mg-0.2%Si-Coated Steel Sheet, Materials Transactions, 49 (2008) 1401-1409.

[80] F. Sauerwald, Das Zustandsdiagramm Magnesium-Zirkonium, Zeitschrift für anorganische Chemie, 255 (1947) 212-220.

[81] E.F. Emley, Principles of magnesium technology, Pergamon Press, London, UK, 1966.

[82] F. Wang, Z. Liu, D. Qiu, J.A. Taylor, M.A. Easton, M.-X. Zhang, Revisiting the role of peritectics in grain refinement of Al alloys, Acta Materialia, 61 (2013) 360-370.

[83] M. Qian, D. StJohn, M. Frost, M. Barnett, Grain refinement of pure magnesium using rolled zirmax master alloy (Mg-33.3Zr), Magnesium Technology, 2003 (2003) 215-220.

[84] M. Qian, D.H. StJohn, M. Frost, Zirconium alloying and grain refinement of magnesium alloys, Magnesium Technology 2003, (2003) 209-214.

[85] M. Qian, D.H. StJohn, M.T. Frost, Effect of soluble and insoluble zirconium on the grain refinement of magnesium alloys, Materials Science Forum, 419-422 (2003) 593-598.

[86] Y. Wang, X. Zeng, W. Ding, A.A. Luo, A.K. Sachdev, Grain Refinement of AZ31 Magnesium Alloy by Titanium and Low-Frequency Electromagnetic Casting, Metallurgical and Materials Transactions A, 38 (2007) 1358-1366.

[87] W. Kurz, D.J. Fisher, Fundamentals of solidification (3rd edition), Trans Tech Publications, Switzerland, 1989.

[88] P.G. de Gennes, Wetting: statics and dynamics, Reviews of modern physics, 57 (1985) 827-863.

[89] H.B. Aaron, D. Fainstein, G.R. Kotler, Diffusion-Limited Phase Transformations: A Comparison and Critical Evaluation of the Mathematical Approximations, Journal of applied physics, 41 (1970) 4404-4410.

[90] M. Qian, P. Cao, M.A. Easton, S.D. McDonald, D.H. StJohn, An analytical model for constitutional supercooling-driven grain formation and grain size prediction, Acta Materialia, 58 (2010) 3262-3270.

[91] J. Du, W. Han, Y. Peng, Life cycle greenhouse gases, energy and cost assessment of automobiles using magnesium from Chinese Pidgeon process, Journal of Cleaner Production, 18 (2010) 112-119.

[92] A.A. Nayeb-Hashemi, J.B. Clark, Phase diagrams of binary magnesium alloys, ASM International, Metals Park, Ohio, USA, 1988.

[93] V. Petrovich, Grain refining process, US Patent (US3290742), 1966.

[94] J. Du, J. Yang, M. Kuwabara, W. Li, J. Peng, Effect of iron and/or carbon on the grain refinement of Mg-3Al alloy, Materials transactions, 48 (2007) 2903-2908.

[95] P. Cao, M. Qian, D.H. StJohn, Effect of iron on grain refinement of high-purity Mg–Al alloys, Scripta Materialia, 51 (2004) 125-129.

[96] Y. Tamura, T. Haitani, E. Yano, T. Motegi, N. Kono, E. Sato, Grain refinement of high-purity Mg-Al alloy ingots and influences of minor amounts of iron and manganese on cast grain size, Materials Transactions, 43 (2002) 2784-2788.

[97] J. Du, M. Wang, W. Li, Effects of Fe addition and addition sequence on carbon inoculation of Mg–3%Al alloy, Journal of Alloys and Compounds, 502 (2010) 74-79.

[98] P. Cao, M. Qian, D.H. StJohn, Mechanism for grain refinement of magnesium alloys by superheating, Scripta Materialia, 56 (2007) 633-636.

[99] P. Cao, M. Qian, D.H. StJohn, Native grain refinement of magnesium alloys, Scripta Materialia, 53 (2005) 841-844.

[100] M. Ohno, D. Mirkovic, R. Schmid-Fetzer, Liquidus and solidus temperatures of

Mg-rich Mg–Al–Mn–Zn alloys, Acta Materialia, 54 (2006) 3883-3891.

[101] P. Cao, M. Qian, D.H. StJohn, Effect of manganese on grain refinement of Mg–Al based alloys, Scripta Materialia, 54 (2006) 1853-1858.

[102] T. Laser, M. Nürnberg, A. Janz, C. Hartig, D. Letzig, R. Schmid-Fetzer, R. Bormann, The influence of manganese on the microstructure and mechanical properties of AZ31 gravity die cast alloys, Acta Materialia, 54 (2006) 3033-3041.

[103] Y.M. Kim, L. Wang, B.S. You, Grain refinement of Mg–Al cast alloy by the addition of manganese carbonate, Journal of Alloys and Compounds, 490 (2010) 695-699.

[104] Y. Wang, M. Xia, Z. Fan, X. Zhou, G.E. Thompson, The effect of Al_8Mn_5 intermetallic particles on grain size of as-cast Mg–Al–Zn AZ91D alloy, Intermetallics, 18 (2010) 1683-1689.

[105] M. Mabuchi, K. Kubota, K. Higashi, Tensile strength, ductility and fracture of magnesium-silicon alloys, Journal of Materials Science, 31 (1996) 1529-1535.

[106] A. Srinivasan, U. Pillai, B. Pai, Microstructure and mechanical properties of Si and Sb added AZ91 magnesium alloy, Metallurgical and Materials Transactions A, 36 (2005) 2235-2243.

[107] J.J. Kim, D.H. Kim, K. Shin, N.J. Kim, Modification of Mg_2Si morphology in squeeze cast Mg-Al-Zn-Si alloys by Ca or P addition, Scripta Materialia, 41 (1999) 333-340.

[108] Y. Guangyin, L. Manping, D. Wenjiang, A. Inoue, Microstructure and mechanical properties of Mg–Zn–Si-based alloys, Materials Science and Engineering: A, 357 (2003) 314-320.

[109] Y.B. Zuo, X. Fu, D. Mou, Q.F. Zhu, L. Li, J.Z. Cui, Study on the role of Ca in the grain refinement of Mg–Ca binary alloys, Mater Res Innov, 19 (2015) 94-97.

[110] J. Du, J. Yang, M. Kuwabara, W. Li, J. Peng, Improvement of grain refining efficiency for Mg–Al alloy modified by the combination of carbon and calcium, Journal of Alloys and Compounds, 470 (2009) 134-140.

[111] S.E. Harandi, M. Mirshahi, S. Koleini, M.H. Idris, H. Jafari, M.R.A. Kadir, Effect of calcium content on the microstructure, hardness and in-vitro corrosion behavior of biodegradable Mg-Ca binary alloy, Materials Research, 16 (2013) 11-18.

[112] Z. Li, X. Gu, S. Lou, Y. Zheng, The development of binary Mg–Ca alloys for use as

biodegradable materials within bone, Biomaterials, 29 (2008) 1329-1344.

[113] A. Suzuki, N. Saddock, J. Jones, T. Pollock, Solidification paths and eutectic intermetallic phases in Mg–Al–Ca ternary alloys, Acta Materialia, 53 (2005) 2823-2834.

[114] E. Yano, Y. Tamura, T. Motegi, E. Sato, Effect of carbon powder on grain refinement of an AZ91E magnesium alloy, Materials Transactions, 44 (2003) 107-110.

[115] M. Qian, P. Cao, Discussions on grain refinement of magnesium alloys by carbon inoculation, Scripta Materialia, 52 (2005) 415-419.

[116] H.L. Chen, N. Li, A. Klostermeier, R. Schmid-Fetzer, Measurement of carbon solubility in magnesium alloys using GD-OES, Journal of Analytical Atomic Spectrometry, 26 (2011) 2189-2196.

[117] H.L. Chen, R. Schmid-Fetzer, The Mg–C phase equilibria and their thermodynamic basis, International Journal of Materials Research, 103 (2012) 1294-1301.

[118] A. Luo, Heterogeneous nucleation and grain refinement in cast Mg(AZ91)/SiCp metal matrix composites, Canadian Metallurgical Quarterly, 35 (1996) 375-383.

[119] Q. Jin, J.P. Eom, S.G. Lim, W.W. Park, B.S. You, Grain refining mechanism of a carbon addition method in a Mg–Al magnesium alloy, Scripta Materialia, 49 (2003) 1129-1132.

[120] L. Lu, A.K. Dahle, J.A. Taylor, D.H. StJohn, Theoretical and practical considerations of grain refinement of Mg-Al alloys, in: Materials Science Forum, Trans Tech Publ, 2005, pp. 299-302.

[121] G. Han, X. Liu, H. Ding, Grain refinement of Mg–Al based alloys by a new Al–C master alloy, Journal of Alloys and Compounds, 467 (2009) 202-207.

[122] T.J. Chen, X.D. Jiang, Y. Ma, Y.D. Li, Y. Hao, Grain refinement of AZ91D magnesium alloy by SiC, Journal of Alloys and Compounds, 496 (2010) 218-225.

[123] Y. Tamura, N. Kono, T. Motegi, E. Sato, Grain refinement of cast Mg-Al alloys, Journal of Japan Institute of Light Metals (Japan), 48 (1998) 395-399.

[124] E. Yano, Y. Tamura, T. Motegi, E. Sato, Grain refining mechanism of cast magnesium alloy AZ91 by superheat treatment, Journal of Japan Institute of Light Metals (Japan), 51 (2001) 594-598.

[125] D.R. Gaskell, Introduction to the thermodynamics of materials, Taylor & Francis, New York, USA, 1995.

[126] M. Suresh, A. Srinivasan, U.T.S. Pillai, B.C. Pai, Mechanism for Grain Refinement and Mechanical Properties of AZ91 Mg Alloy by Carbon Inoculation, Procedia Engineering, 55 (2013) 93-97.

[127] Y.D. Huang, X.H. Zheng, A. Okechukwu, G.S. Kim, K.U. Kainer, N. Hort, Aluminium-Rich Coring Structures in Mg-Al Alloys with Carbon Inoculation, Materials Science Forum, 654-656 (2010) 675-678.

[128] H. Haferkamp, F. Bach, V. Kaese, K. Möhwald, M. Niemeyer, H. Schreckenberger, P.T. Tai, Magnesium Corrosion–Processes, Protection of Anode and Cathode, Magnesium-Alloys and Technology, (2003) 226-241.

[129] J.B. Clark, Transmission electron microscopy study of age hardening in a Mg-5 wt.% Zn alloy, Acta Metallurgica, 13 (1965) 1281-1289.

[130] X. Gao, J.F. Nie, Characterization of strengthening precipitate phases in a Mg–Zn alloy, Scripta Materialia, 56 (2007) 645-648.

[131] H. Tapiero, K.D. Tew, Trace elements in human physiology and pathology: zinc and metallothioneins, Biomedicine & Pharmacotherapy, 57 (2003) 399-411.

[132] S. Zhang, X. Zhang, C. Zhao, J. Li, Y. Song, C. Xie, H. Tao, Y. Zhang, Y. He, Y. Jiang, Research on an Mg–Zn alloy as a degradable biomaterial, Acta Biomaterialia, 6 (2010) 626-640.

[133] X.Y. Fang, D.Q. Yi, J.F. Nie, X.J. Zhang, B. Wang, L.R. Xiao, Effect of Zr, Mn and Sc additions on the grain size of Mg–Gd alloy, Journal of Alloys and Compounds, 470 (2009) 311-316.

[134] J. Wang, R. Lu, D. Qin, X. Huang, F. Pan, A study of the ultrahigh damping capacities in Mg–Mn alloys, Materials Science and Engineering: A, 560 (2013) 667-671.

[135] L. Zhong, J. Peng, Y. Sun, Y. Wang, Y. Lu, F. Pan, Microstructure and thermal conductivity of as-cast and as-extruded binary Mg–Mn alloys, Materials Science and Technology, 33 (2016) 1-6.

[136] L. Xu, G. Yu, E. Zhang, F. Pan, K. Yang, In vivo corrosion behavior of Mg-Mn-Zn alloy for bone implant application, Journal of Biomedical Materials Research, 83 (2007) 703-711.

[137] E. Zhang, D. Yin, L. Xu, L. Yang, K. Yang, Microstructure, mechanical and corrosion properties and biocompatibility of Mg–Zn–Mn alloys for biomedical application, Materials

Science and Engineering: C, 29 (2009) 987-993.

[138] Y.L. Zhou, Y. Li, D.M. Luo, Y. Ding, P. Hodgson, Microstructures, mechanical and corrosion properties and biocompatibility of as extruded Mg–Mn–Zn–Nd alloys for biomedical applications, Materials Science and Engineering: C, 49 (2015) 93-100.

[139] X. Liu, J. Sun, F. Zhou, Y. Yang, R. Chang, K. Qiu, Z. Pu, L. Li, Y. Zheng, Micro-alloying with Mn in Zn–Mg alloy for future biodegradable metals application, Materials & Design, 94 (2016) 95-104.

[140] ASTM E112-10, Standard test methods for determining average grain size, ASTM International, West Conshohocken, PA, 2010, DOI: 10.1520/E0112-10.

[141] E. Scheil, Bemerkungen zur schichtkristallbildung, Zeitschrift für Metallkunde, 34 (1942) 70-72.

[142] R. Schmid-Fetzer, J. Gröbner, S. Zhu, J.F. Nie, M.A. Gibson, Phase Stability and Formation in Mg–Gd–Zn Alloys—Key Data for ICME of Mg Alloys, Magnesium Technology 2017, (2017) 365-371.

[143] S.M. Liang, R. Schmid-Fetzer, Phosphorus in Al–Si cast alloys: Thermodynamic prediction of the AlP and eutectic (Si) solidification sequence validated by microstructure and nucleation undercooling data, Acta Materialia, 72 (2014) 41-56.

[144] Y. Liu, X. Liu, X. Bian, Grain refinement of Mg–Al alloys with Al_4C_3–SiC/Al master alloy, Materials Letters, 58 (2004) 1282-1287.

[145] M. De Cicco, H. Konishi, G. Cao, H.S. Choi, L.S. Turng, J.H. Perepezko, S. Kou, R. Lakes, X. Li, Strong, ductile magnesium-zinc nanocomposites, Metallurgical and Materials Transactions A, 40 (2009) 3038-3045.

[146] W.Z. Zhang, G.C. Weatherly, On the crystallography of precipitation, Progress in Materials Science, 50 (2005) 181-292.

[147] M. Johnsson, Grain refinement of aluminium studied by use of a thermal analytical technique, Thermochimica Acta, 256 (1995) 107-121.

[148] B. Inem, G. Pollard, Interface structure and fractography of a magnesium-alloy, metal-matrix composite reinforced with SiC particles, Journal of Materials Science, 28 (1993) 4427-4434.

[149] B. Inem, Crystallography of the second phase/SiC particles interface, nucleation of the

second phase at β-SiC and its effect on interfacial bonding, elastic properties and ductility of magnesium matrix composites, Journal of Materials Science, 30 (1995) 5763-5769.

[150] K.O. Yu, Modeling for casting and solidification processing, CRC Press, Ohio, USA, 2001.

[151] J. Kerr, D. Lide, CRC handbook of chemistry and physics, CRC press, Florida, USA, 1999-2000.

[152] M. Hirai, Estimation of Viscosities of Liquid Alloys, ISIJ international, 33 (1993) 251-258.

[153] G.W. Qin, Y. Ren, W. Huang, S. Li, W. Pei, Grain refining mechanism of Al-containing Mg alloys with the addition of Mn–Al alloys, Journal of Alloys and Compounds, 507 (2010) 410-413.

[154] S. Stankovich, D.A. Dikin, R.D. Piner, K.A. Kohlhaas, A. Kleinhammes, Y. Jia, Y. Wu, S.T. Nguyen, R.S. Ruoff, Synthesis of graphene-based nanosheets via chemical reduction of exfoliated graphite oxide, Carbon, 45 (2007) 1558-1565.

[155] Z. Liu, D. Qiu, F. Wang, J.A. Taylor, M.X. Zhang, Grain refinement of cast zinc through magnesium inoculation: Characterisation and mechanism, Materials Characterization, 106 (2015) 1-10.